2017

Investigation of Residual Stresses in Melt Infiltrated SiC/SiC Ceramic Matrix Composites using Raman Spectroscopy

Kaitlin Noelle Kollins
Wright State University

INVESTIGATION OF RESIDUAL STRESSES IN MELT INFILTRATED SiC/SiC CERAMIC MATRIX COMPOSITES USING RAMAN SPECTROSCOPY

A thesis submitted in partial fulfillment of the
requirements for the degree of
Master of Science in Materials Science and Engineering

By

KAITLIN NOELLE KOLLINS
B.S.M.E., Wright State University, 2017

2017
Wright State University

WRIGHT STATE UNIVERSITY

GRADUATE SCHOOL

September 19, 2017

I HEREBY RECOMMEND THAT THE THESIS PREPARED UNDER MY SUPERVISION BY Kaitlin Noelle Kollins ENTITLED Investigation of Residual Stresses in Melt Infiltrated SiC/SiC Ceramic Matrix Composites Using Raman Spectroscopy BE ACCEPTED IN PARTIAL FULFILLMENT OF THE REQUIREMENTS FOR THE DEGREE OF Master of Science in Materials Science and Engineering

Maher S. Amer, Ph.D.
Thesis Director

Joseph C. Slater, Ph.D., P.E.
Chair, Department of Mechanical and Materials Engineering

Committee on
Final Examination

Maher S. Amer, Ph.D.

Craig P. Przybyla, Ph.D.

Henry D. Young, Ph.D.

Barry Milligan, Ph.D.
Interim Dean of the Graduate School

ABSTRACT

Kollins, Kaitlin Noelle. M.S.M.S.E. Department of Mechanical and Materials Engineering, Wright State University, 2017. Investigation of Residual Stresses in Melt Infiltrated SiC/SiC Ceramic Matrix Composites Using Raman Spectroscopy.

Ceramic matric composites (CMCs) are being developed for use in extreme operating conditions. Specifically, there is interest to replace superalloys with Silicon Carbide/Silicon Carbide (SiC/SiC) CMCs in the hot section of gas turbine engines because of their lower densities, high temperature performance, and oxidation resistance. Residual stresses in SiC/SiC CMCs are a direct result of the high temperature processing conditions, a mismatch in the coefficients of thermal expansion between composite constituents, and silicon crystallization expansion upon cooldown. Understanding the residual stress state and magnitudes of these stresses will enable better prediction of behavior and life performance in application environments. This study focused on using micro-Raman spectroscopy, indentation cracking, and mechanical testing on as-received and annealed SiC/SiC CMCs to measure and investigate the residual stresses within the composite. Following the silicon Raman active mode at 520 cm^{-1} and the SiC Raman active mode at 796 cm^{-1}, residual stresses within the matrix and reinforcing fibers were investigated with a spatial resolution of 1 micron. Indentation cracking allowed for an estimate of the residual stresses solely in the matrix material. Mechanical testing, paired with acoustic emission, enabled an understanding of the macro-mechanical behavior of the composite. Results from this study will aid in behavior and damage modeling of SiC/SiC CMCs.

TABLE OF CONTENTS

LIST OF FIGURES

LIST OF TABLES

ACKNOWLEDGMENTS

I would like to thank my mentor Dr. Craig Przybyla of the Air Force Research Laboratory for the help and support he has provided me while working at AFRL. I would not be where I am today if it were not for his guidance and support.

I would also like to thank my advisor, Dr. Maher Amer of Wright State University. Dr. Amer has helped immensely with his knowledge and expertise of Raman spectroscopy and ceramics.

Jennifer Pierce of UDRI and Larry Zawada of UTC, Inc. have also been a great source of support and knowledge of CMCs. Dale Osborne and Phil Blosser of UDRI were extremely helpful with mechanical testing. Many thanks go to Dr. Travis Whitlow of UDRI, Stephen Hawkins of SOCHE, and Samuel Sherman of UTC for their assistance with AE data processing. I would like to thank Dr. Pasha Nikolaev of UES for providing training with Raman spectroscopy. Also, I appreciate the aid Randy Corns and Tommy Cissel of UES provided with sample preparation.

Lastly, I would like to thank my friends and family for their constant support. Andrew Detwiler and Nathan Levkulich have been a great source of encouragement. Dr. Michael Knauf has been a helpful friend and colleague throughout this process. Most importantly, I would like to thank my parents and sisters for always being there and providing me with the resources to be successful.

I. INTRODUCTION

1.1 Objective

Use of ceramic matrix composites (CMCs) is becoming increasingly desirable in high temperature applications, such as turbine jet engines and hypersonic vehicles. CMCs have higher temperature capabilities and higher oxidation resistance, with a lower density than the metal alloy parts that are currently used. Because of these desirable properties, it is important to understand the behavior of CMCs through their life cycle. One property that affects the mechanical behavior of a CMC is the residual stresses that are inherent to the material. Various methods can be used to study residual stresses, including, but not limited to, Raman spectroscopy, crack indentation, and mechanical testing. The objective of this study is to understand the effect that residual stresses have on a SiC/SiC CMC through its life cycle by using annealing techniques residual stress measurement methods.

1.2 Thesis Overview

The ensuing chapters will detail the work completed to characterize residual stresses within SiC/SiC composites. The next chapter will give a detailed background on ceramic matrix composites and their sources of residual stresses. Also, backgrounds will be provided for residual stress measurement techniques, as well as experiments using these techniques that have been performed using silicon, SiC, or SiC/SiC CMCs. A review of annealing techniques for both silicon and SiC are provided as well. Chapter 3

will discuss the specific material used in this study, as well as giving mechanical testing results previously found in the material. Also, Chapter 3 lists the testing procedures for processes used in this study, including volume fraction, annealing, mechanical testing, crack indentation and Raman testing procedures. Chapter 4 will state the results obtained from the processes completed. Last, Chapter 5 will supply a discussion of the results and Chapter 6 will state conclusions and suggestions for future work.

II. BACKGROUND

This chapter provides a background on Ceramic Matrix Composites (CMCs), SiC/SiC CMCs, residual stresses, residual stress measurement techniques, and annealing. The first section will describe basic CMCs, their properties, and their reinforcement types. The next section contains information about the applications of SiC/SiC CMCs and how they are manufactured. The third section discusses residual stresses and their effects in CMCs. A review on residual stress measurement techniques will be provided in the fourth section. The last section gives a description of various annealing techniques for silicon and SiC.

2.1 Ceramic Matrix Composites

2.1.1 Basic Properties of CMCs

A basic CMC consists of ceramic reinforcements (in the form of fibers or particulates) surrounded by a ceramic matrix [1]. Typical ceramics are known to be brittle and experience torturous fracture, but by adding a second phase material in the form of particles, fibers, or whiskers, crack growth is interrupted [2]. Continuous fibers within the matrix provide the highest increase in toughness and strength for CMCs when compared to other forms of reinforcement [2]. CMCs are being developed to replace high temperature metal alloys in high-temperature applications, such as jet engines or hypersonic vehicles, or enable system concepts previously inaccessible due to the temperature limitations of current commercially available structural materials.

Specifically, CMCs offer densities that are significantly less than current high temperature alloys, and CMCs can exhibit mechanical properties sufficient for a wide range of applications, dependent upon the type of ceramic used [1, 3].

2.1.2 Reinforcement Types

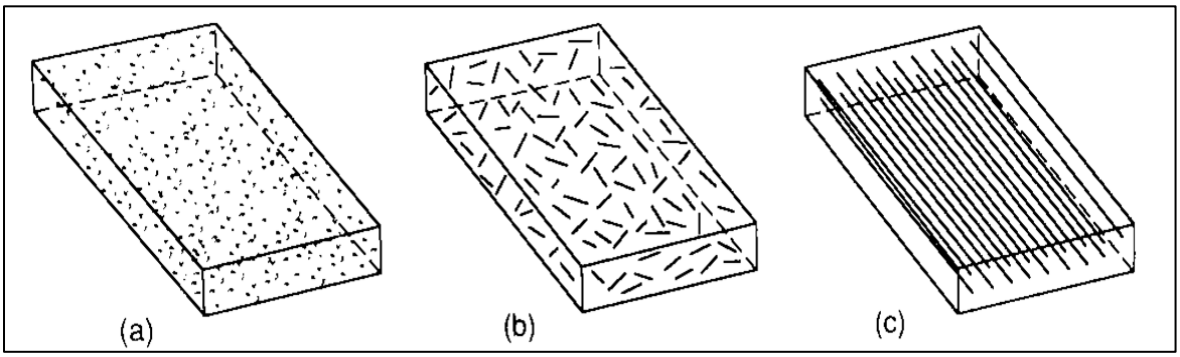

Figure 1: Reinforcement types for composites include (a) particulate reinforcements, (b) discontinuous whisker reinforcements, and (c) continuous fiber composites [4]

There are multiple types of reinforcements for composites, including particulate reinforcements, discontinuous fiber whisker reinforcements, and continuous fiber composites, including laminate or woven composites [5]. Figure 1 shows a particulate reinforced composite, a discontinuous whisker reinforced composite, and a laminate composite [4]. By adding ductile particles to a brittle ceramic matrix, the toughness of the material is increased because cracks cannot propagate as easily through the particulates as it could through the monolith [4]. Particulate reinforced ceramic composites are used in applications such as cutting tools, bridges, and buildings [4]. Discontinuous ceramic whisker reinforcements can either be used to strengthen

materials, or act as a “filler” material to help reduce costs of the final material [5]. Continuous fiber reinforcements, when oriented in a unidirectional manner, provide the maximum strength and stiffness in the fiber direction [4]. Materials strengthened by continuous fibers are typically employed for structural components. In order to make the composite strong in both the longitudinal and transverse direction of the fibers, a laminate can be made [4]. For laminates, several layers of a continuous fiber composite are stacked upon one another with alternating orientations [5]. Figure 2 shows an example laminate composite with varying orientations for each layer [4]. In woven materials, the fibers are interlocked with one another by weaving, braiding, or knitting the fiber tows [5]. This architecture will also strengthen the material in both the longitudinal and transverse directions. This orientation also creates an out-of-plane orientation, allowing for the additional ability to have structural, thermal, or electrical properties in the out-of-plane direction [5]. The ability to change reinforcement type or orientation enables optimization of a material for a multitude of applications.

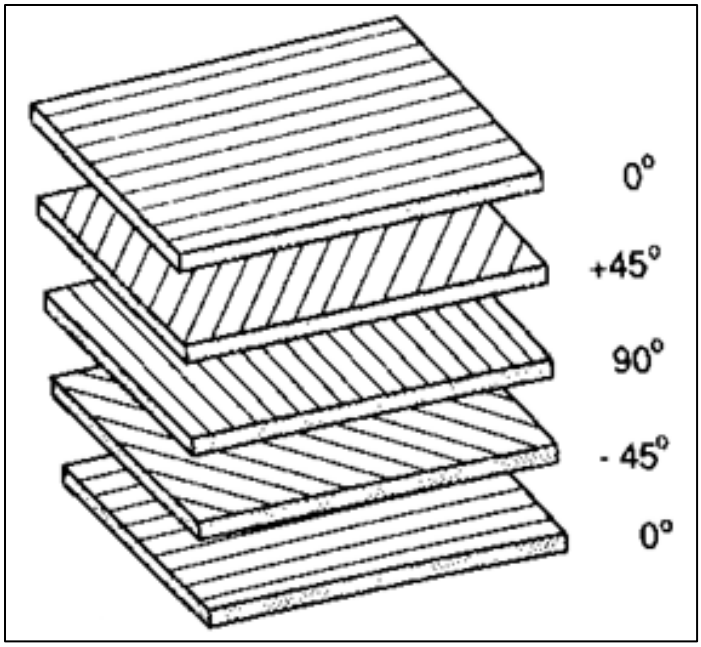

Figure 2: An example laminate composite is shown with various fiber orientations [5]

2.2 Silicon Carbide/Silicon Carbide Ceramic Matrix Composites

Silicon-Carbide continuous fiber reinforced Silicon-Carbide matrix composites (SiC/SiC CMCs) cannot only withstand high temperature environments, but also have oxidation resistance and mechanical properties that make them suitable for use in advanced engine applications [2]. Ni-base superalloys are currently the primary material used for hot section components of gas turbine engines, but SiC/SiC CMCs have a combination of properties that make them more promising for future innovation than their metal counterparts. SiC/SiC CMCs exhibit oxidation resistance at temperatures much higher than superalloys, making them suitable for use in an oxidizing environment [2]. SiC/SiC CMCs enable many possible improvements to current gas turbine engines, including reduced cooling requirements, simpler component design, reduced structural

weight, and improved fuel efficiency [3]. Components that may be replaced by CMCs include hot gas path components, as imaged in Figure 3 [6].

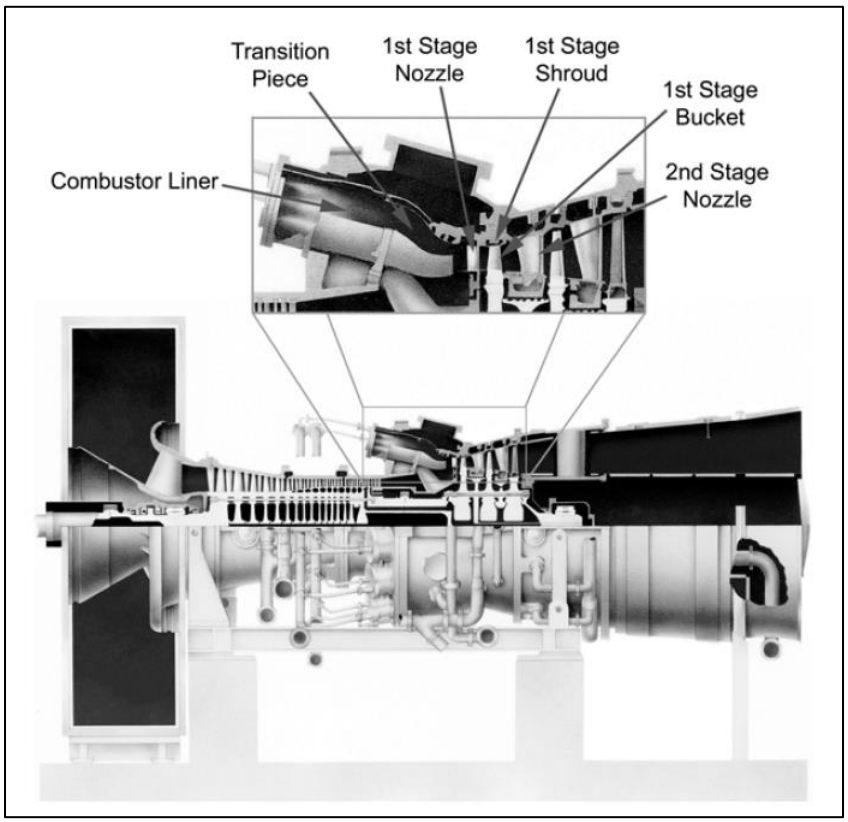

Figure 3: The parts highlighted in this image are currently metallic parts that are candidates to be replaced by CMCs [6]

2.2.1 Processing Techniques for SiC/SiC CMCs

CMCs are produced through various processing techniques, including, but not limited to, chemical vapor infiltration (CVI) and slurry melt infiltration (SMI) [1, 2]. CVI and SMI are the two techniques used to manufacture the material used in this study. Because of the high melting temperatures of the ceramic materials used to make CMCs, processing temperatures over 1400° C are not uncommon [2, 3]. It is important

to note that finding compatible fiber and matrix materials is vital. Due to chemical and mechanical interactions at the bonding surface, degradation of the fiber reinforcement during processing can occur [2]. Also, to ensure toughness as well and strength in CMCs, sufficient conditions for debonding and stress transfer must be met at the bonding interface between the fiber and the matrix [2]. In some cases, a fiber coating may be applied to ensure a proper interface between the fiber and matrix [2].

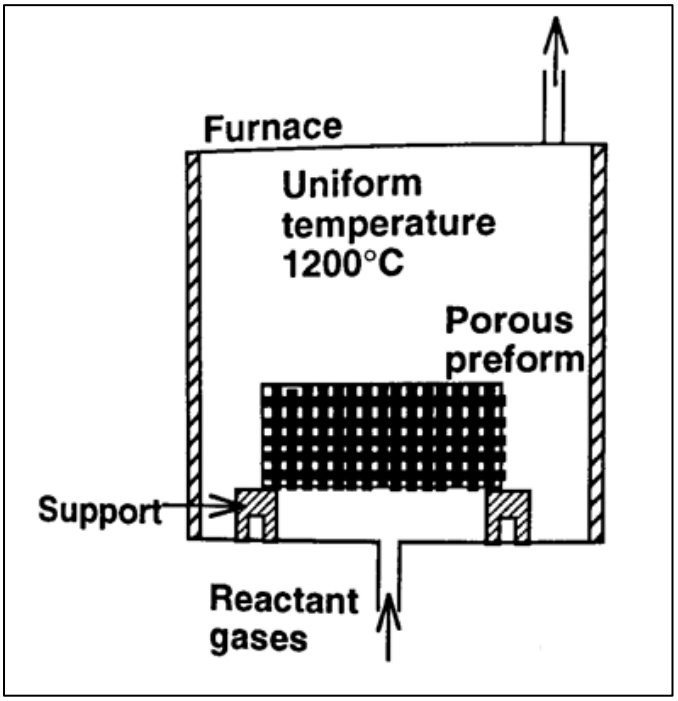

Figure 4: The CVI process in which reactant gases are exposed to a porous preform, depositing a solid matrix on top of the fibers [2]

In CVI, a porous preform of fibers is exposed to reactant gases which penetrate the pores of the preform [2]. The gases react to form a solid matrix on top of the fibers [2]. Using the CVI process, complex shaped objects can be formed, creating components

such as turbine nozzle flaps, rotors, and combustors [2]. A diagram is shown of the CVI process in Figure 4 [2].

The SMI process involves infiltration of a prepreg fiber preform with a matrix material that is heated to become viscous. When the matrix molten matrix material comes into contact with the fiber preform, the wetting properties of the fiber preform are such that it wicks the molten matrix material into and around the fibers [7]. In some cases, the fiber preform is first infiltrated with a resin [7]. After consolidation, pyrolysis leaves reactant components from the resin in the porosity which react with the molten material being infiltrated, forming a secondary matrix [7]. In SiC/SiC SMI materials, a Si metal is typically infiltrated into a preform with significant excess carbon. The molten Si metal reacts with the excess carbon to form a predominantly SiC matrix [3]. This process results in high densification and only leaves a small percent of porosity, but also leaves pools of residual, unreacted silicon [2]. The matrix processing technique can be seen in Figure 5 [7]. An image labeling the various constituents of the CMC can be seen in Figure 6.

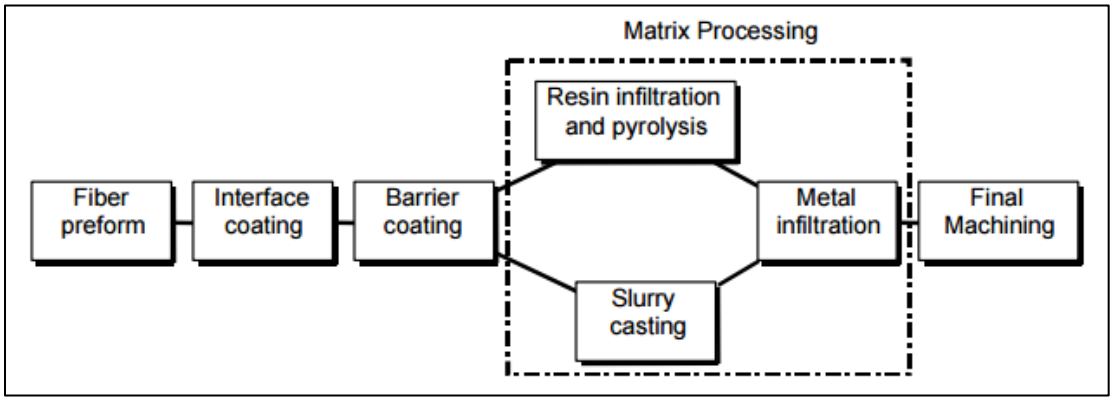

Figure 5: Melt Infiltration Process for SiC/SiC CMCs [7]

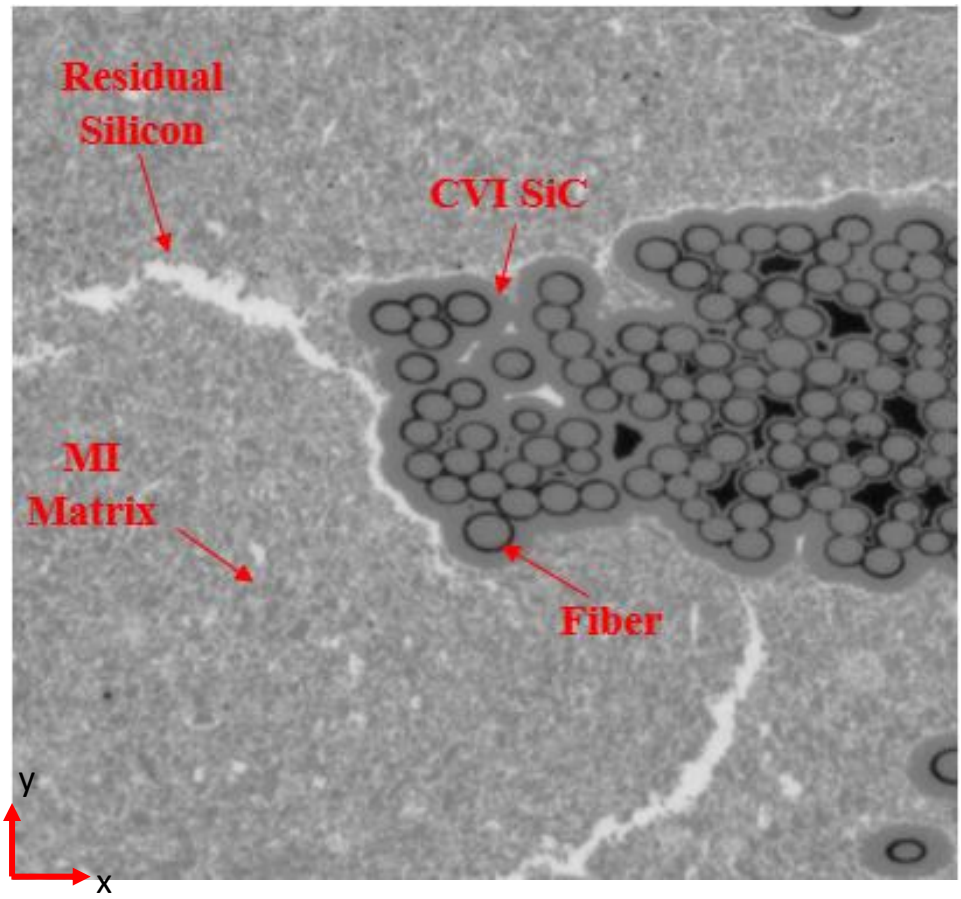

Figure 6: Plate 1 Micrograph

2.3 Residual Stresses

Residual stresses are stresses that are inherent to the material, and do not depend on any external loads [8]. Residual stresses can either be tensile or compressive, but the net force and moment resultants for the material are zero absent any externally applied loads [8]. Residual stresses typically occur due to manufacturing processes, but can also develop or change during the life cycle of the component [8]. Residual stresses affect the material's behavior, and can locally be considered as an addition or subtraction to any stresses that result from externally applied loads [8]. Depending on the location, type, and magnitude of residual stress present, it can improve or degrade material performance

[8]. Compressive residual oriented such that they act opposite to the crack opening stresses generated by the external loading conditions reduce or prevent crack grown [4]. A common method to induce compressive residual stresses oriented parallel to the surface in a ductile metal is through shot peening. On the other hand, stresses oriented such that they act in concert with the crack opening stresses generated by the external loading conditions promote and/or accelerate crack growth [4]. One method employed to relieve residual stresses is typically some form of heat treatment such as annealing. There are various experimental methods of measuring residual stresses, including both destructive and non-destructive techniques. Destructive techniques include common intersection point of hysteresis loops, indentation, and mechanical testing. Non-destructive techniques include Raman spectroscopy and X-Ray Diffraction [8]. These methods will be discussed in Section 2.4.

2.3.1 Processing Residual Stresses in SiC/SiC Composites

There are multiple sources of residual stresses in SiC/SiC composites. In SiC/SiC composites, one source of residual stress is a result of the mismatch in the coefficients of thermal expansion (CTEs) between the fiber and matrix materials. Specifically, these thermally induced residual stresses are proportional to the mismatch in the CTEs between the fiber and matrix materials and the difference between the processing and room temperatures [2]. If the matrix CTE is higher than the fiber CTE, then there will be axial tensile stresses in the matrix, and axial and radial compressive stresses in the fiber. Conversely, if the matrix CTE is lower than the fiber CTE, then there will be axial compressive stresses in the matrix and axial and radial tensile stresses in the fiber. This is the case for the materials used in this study. In order to reduce thermal residual

stresses during processing, it is important to minimize the difference in the CTEs. This will allow for the constituents to expand and contract at the same rate, reducing constituent stresses. The CTEs for the various constituents in the SiC/SiC CMCs in this study are listed in Table 1.

Table 1: Coefficients of Thermal Expansion for Si, SiC and Sylramic Fibers

Material	Coefficient of Thermal Expansion (10^{-6}/°C)
Silicon	2.6 [9]
Cubic 3C-Silicon Carbide	2.7 [10]
Sylramic Fiber	5.4 [11]
Sylramic-iBN Fiber	5.4 [11]

The axial residual stress within a non-cracked matrix can be estimated according to Equation 1 [12]:

$$\sigma_r^m = E_m \frac{\lambda E_f V_f}{\lambda E_f V_f + E_m V_m} (\alpha_f - \alpha_m)(T_o - T_p)$$

Equation 1

where the constants are defined in Table 2 as:

Table 2: Axial Residual Stress Calculation Constants

E_m, E_f	Elastic Moduli of Matrix and Fiber
V_m,V_f	Volume Fraction of Matrix and Fiber
λ	Woven Fiber Architecture Correction Factor
α_m, α_f	Linear CTE of Matrix and Fiber
T_o, T_p	Operating Temperature and Processing Temperature

2.3.2 Residual Stresses from Silicon Expansion in SiC/SiC Composites

A second source of residual stress in SiC/SiC SMI CMCs can be attributed to the residual silicon in the matrix that expands when the material cools after infiltration and the silicon solidifies. As discussed previously, in SiC/SiC SMI CMCs, molten silicon is infiltrated into a fiber preform containing SiC particulates. In some cases, the fiber preform may contain some residual carbon as well. During infiltration, the silicon reacts with any residual carbon in the matrix to form SiC, but unreacted silicon will fill the remaining voids around the SiC particulate, as well as fill any large pores or cracks. This results in the development of large silicon pools and veins throughout the composite. Similar to water, during the cooling and solidification of silicon from the liquid phase, there is a significant volume expansion [13]. This volume expansion then induces compressive residual stresses in the silicon, as the silicon is trying to expand within the much less compliant SiC. The amount of volume expansion can be estimated by correlating the silicon density at processing and room temperatures, seen in Section 4.6.1.

2.4 Residual Stress Measurement Techniques

2.4.1 Raman Spectroscopy

Raman spectroscopy is a technique employed to measure various fundamental vibration modes of a material [14]. With Raman, a laser is first focused onto an area of interest on the surface of a sample of material. Photons are excited by the laser, and those that do not transfer energy with the molecules are scattered back at the same wavelength as the laser. This is referred to as Rayleigh scattering, which is elastic in nature [15]. However, a small portion of the photons (about one in a million) interact

with the material and are scattered in an inelastic manner, at wavelengths corresponding to their material constituent, called Raman scattering [15]. To be Raman active, a material must be able to polarize its electric dipoles. Results from Raman spectroscopy are typically reported in terms of the wavenumber of the constituent being measured [14]. Wavenumber is calculated by Equation 2 [16]:

$$\omega = \frac{1}{\lambda_0} - \frac{1}{\lambda}$$

Equation 2

where ω is the wavenumber, λ_0 is the excitation wavelength, and λ is the measured wavelength of the constituent. Any polarizable material has a known wavenumber that can be used to identify the chemical composition of a material.

By utilizing a motorized stage with the microscope, a technique called Raman mapping can be performed. In this technique, many Raman measurements are completed, and a conglomerate map of these measurements is produced. These maps can be used to measure chemical composition, phase structure, and stresses over an area on the surface of a sample of material in a nondestructive manner [17]. Raman spectroscopy has high strain sensitivity, with a high spatial resolution, making it ideal to measure residual stresses [18]. The Raman spectroscopy technique is able to discretize between constituents and stresses on the micron level, while techniques such as X-Ray Diffraction have a spatial resolution on the order of millimeters.

Due to applied strains on the crystal structure of the constituent, known as a morphic effect, a shift in the known value for the wavenumber will occur [16, 19]. A

shift above the known standard, called a blue shift, will indicate a compressive residual stress [16]. Conversely, a red shift will represent a shift below the known wavenumber, and will be indicative of tensile residual stresses [16]. For polycrystalline materials, the shift is indicative of the average of the trace of the stress tensor in the crystal [15]. Only in very specific cases or experimental setups, such as polarized Raman or off-axis Raman, can more information about the stress tensor be resolved [15]. The average of the trace is assumed when taking stress measurements, as it is assumed that the strain applied is elastic in nature [20]. Typically, these stress measurements are calculated assuming there is no change in the chemical composition of the material. If there is a change in the chemical composition, one can make corrections to the stress-free standard to accurately calculate the stresses. Previous research has been completed using Raman spectroscopy to analyze the mechanical states of heterogeneous materials, such as multilayer composites and functionally graded materials [19, 21].

As mentioned, there are known values for the silicon and silicon carbide wavenumbers. Assuming no dopants, the wavenumbers are presented in Table 3.

Table 3: Raman Wavenumbers for Silicon and Cubic Silicon Carbide

Constituent	**Wavenumber (cm^{-1})**
Silicon	520 [22]
Cubic Silicon Carbide Peak 1	796 [22]
Cubic Silicon Carbide Peak 2	973 [22]

A shift from these values indicates a residual stress within the material [19]. In order to calculate the residual stress (σ_R) from the wavenumber shift (ω_s), a stress to

shift conversion factor has been employed previously, ($C_{Shift \rightarrow Stress}$), as can be seen in Equation 3 [23]:

$$\omega_s = \sigma_R * C_{Shift \rightarrow Stress}$$

Equation 3

The conversion factors for both silicon and silicon carbide were previously found, and can be seen in Table 4. These conversion factors assume no dopants are in the material.

Table 4: Shift to Stress Conversion Factors

Constituent	**Shift to Stress Conversion Factor ($C_{Shift \rightarrow Stress}$)**
Silicon	1.88 ± 0.05 cm^{-1}/GPa [24]
Cubic Silicon Carbide Peak 1	3.53 ± 0.21 cm^{-1}/GPa [23]
Cubic Silicon Carbide Peak 2	4.28 ± 0.22 cm^{-1}/GPa [23]

The depth of material studied is dependent upon the absorption coefficient of the material. For SiC, the absorption coefficient at the laser wavelength used in this study, 514 nm, is 13.98 cm^{-1} [25]. This will give a penetration depth of 715 microns for SiC. On the other hand, the penetration depth for silicon is only 1 micron that has an absorption coefficient of 9877 cm^{-1} at 514 nm [26]. In the case of this composite, if there is SiC on the surface layer, silicon beneath it may be detected by the laser. If silicon is on the surface layer, then only silicon will be detected by the laser.

Another consideration that must be made in the case of these composites is Raman's inability to characterize residual stresses in the boron nitride coatings between the fiber and matrix material. The boron nitride fluoresces under the laser, causing the

Raman signal at the fiber coatings to become distorted with a broad background. A demonstration of the fluorescent boron nitride coatings can be seen in Figure 7, taken with a UV microscope using a 365 nm light source.

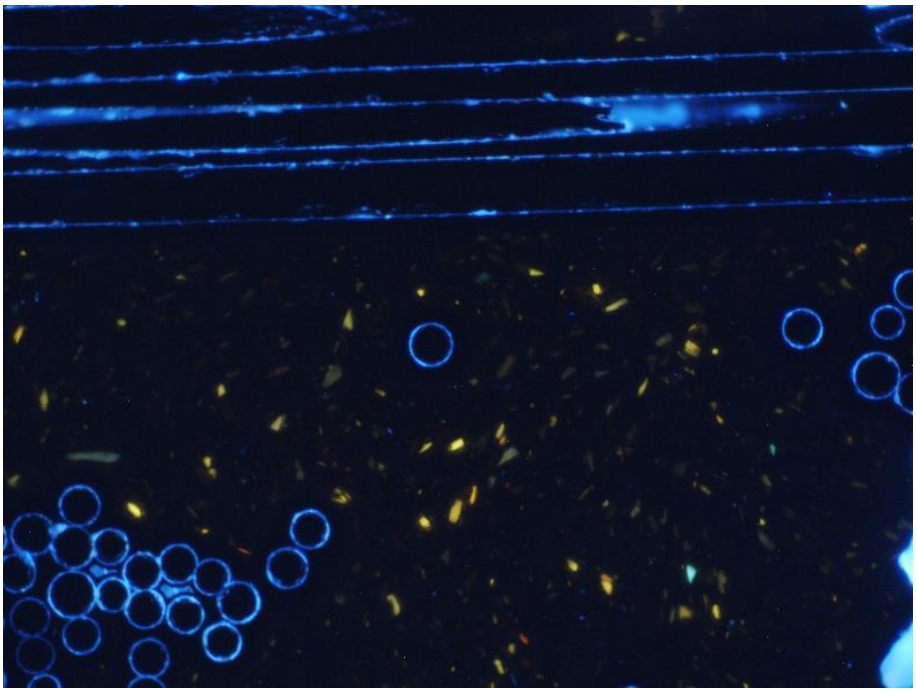

Figure 7: Fluorescence of boron nitride fiber coatings

2.4.2 Stress Measurements in Si, SiC, and SiC/SiC using Raman spectroscopy

Raman spectroscopy has been used to investigate silicon, SiC, and SiC/SiC CMCs, previously. A representative Raman spectra can be seen in Figure 8. Yang et al., employed Raman to investigate the composition of SiC/SiC CMCs with Nicalon fiber reinforcement [27]. Raman spectroscopy has also been utilized on other SiC fibers, including Sylramic fibers [28]. Zhu et al., measured the residual stress states of silicon and silicon carbide with Raman spectroscopy [22]. Recently, composites containing boron carbide, SiC, and silicon phases have been analyzed by Jannotti et al. with Raman

spectroscopy to determine their residual stress state [29]. Another study involving reaction bonded SiC used in MI CMCs has been completed, and will be discussed in Section 2.5.2 as it also contains information on annealing processes [30].

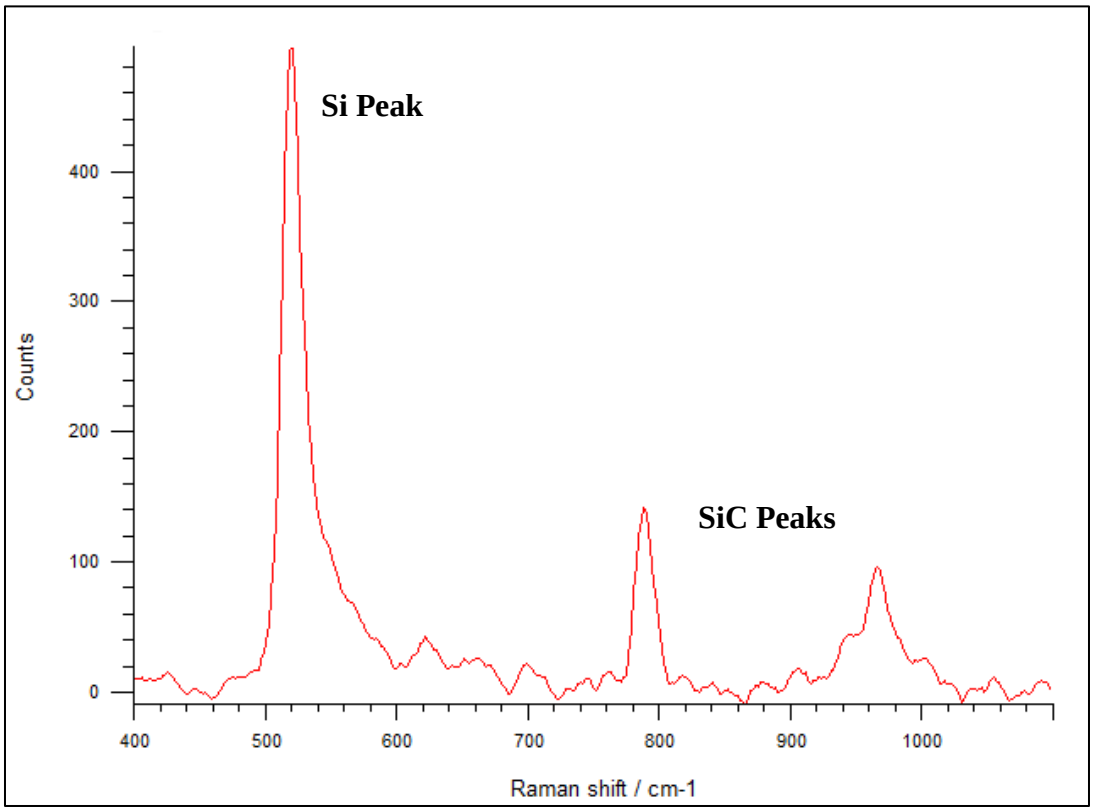

Figure 8: Typical Silicon and Silicon Carbide peaks

Raman spectroscopy can also be useful in determining the composition of SiC/SiC composites. Raman spectra have been obtained from SiC fibers within a ceramic matrix [27]. Along with SiC being present, the D and G carbon bands were also present within the fiber due to excess carbon [27]. In some SiC fibers, the SiC spectrum cannot be recorded due to the C/Si ratio being too high (above 1.1) [28]. However, SiC spectrum can be recorded in Sylramic fibers as the C/Si ratio is nearly 1 [28]. The SiC

spectrum recorded from a Sylramic fiber can be seen in Figure 9 [28]. Notably, there were no carbon bands reported for the Sylramic fibers by Gouadec et. al. [28].

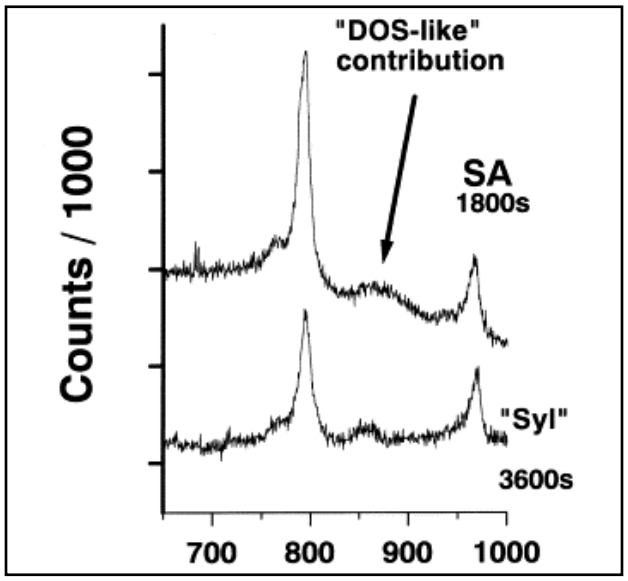

Figure 9: Raman Spectrum of Sylramic Fiber [27]

Not only can Raman be exercised to determine the composition of Si and SiC constituents, it can also be employed to determine the stresses within those constituents. A 3C-SiC film was deposited onto a Si substrate using chemical vapor deposition (CVD) [22]. Because of the thermal mismatch between the film and the substrate, residual stresses occurred. Residual tensile stresses occurred within the SiC, while the Si was in residual compression [22]. The study also found that the residual stresses measured were dependent on the substrate orientation [22].

Jannotti et. al evaluated residual stresses using Raman spectroscopy in B_4C-Si-SiC reaction bonded material of varying concentrations [29]. Using classical modeling that only considered differences in coefficients of thermal expansion [31], predictions of

the residual stresses were made for all phases and volume fractions of the material. Specifically, for the sample containing only silicon and SiC, it was predicted that a silicon grain fully surrounded by SiC would be entirely in hydrostatic compression. of 239 MPa, and the SiC would be in hydrostatic tension of 239 MPa. While predictions were made for all constituents, Raman stress measurements were only reported for the silicon phase. Within relatively small regions of silicon (<5 microns), residual stress measurements were within 20 MPa of the models, reporting a maximum of 260 MPa in hydrostatic compression. However, when the silicon grains were large (>5 microns), the perimeter of the grain was found to be in compression at 260 MPa, but the interior was in tension, with a maximum of 530 MPa. The authors postulate that the nonuniform stresses could be due to 1) the interior of the grain cooling slower than the exterior, 2) a non-hydrostatic stress being applied from the irregular grain shapes, or 3) the different orientations of the surrounding SiC grains having different material constants. Like Wing, et. al, it was found that increasing the Si volume fraction resulted in a decrease in the compressive residual stresses. With a decrease in silicon residual stresses, it was found that the hardness and compressive strength decreased. Jannotti et. al also reported an asymmetric silicon peak shape due to boron dopants.

2.4.3 Indentation Cracking

Residual stresses can be estimated in the matrix material through cracks initiated by indentation. Unlike Raman, this method will not be able to distinguish stress values in the different constituents, but will provide an averaged stress value for the matrix. In brittle materials, when using a Vickers diamond shaped indenter, cracks will be induced into the surface of the material at the corners of the diamond. These methods have

previously been employed to characterize compressive residual stresses in ceramics [32, 33]. With this technique, a few different models with varying crack geometries, including half penny-shaped, semi-circular, and semi-elliptical, have been produced to estimate the residual stresses. For simplicity and the lack of necessary constants for the more advanced models, the most general model, being the half penny-shaped crack, will be examined and used in this study.

When assuming a half penny-shaped crack, Equation 4 [34] is used to calculate the compressive residual stress, σ_{comp}:

$$\sigma_{comp} = K_c \frac{1 - (\frac{c_0}{c_2})^{3/2}}{\sqrt{\pi c_2}}$$

Equation 4

In which K_C is the fracture toughness, c_0 is an unstressed crack length, and c_2 is the stressed crack length. Typically, c_0 is found by indenting a stress-free reference material and measuring the crack length. However, there is no stress-free reference material available in this study. As mentioned, cracks will emanate from the corners of the diamond indenter, in both the horizontal (x-axis) and vertical (y-axis) directions (refer to Figure 6 for the coordinate system). A similar study utilizing a [0/90] laminate composite calculated the stresses using the horizontal crack as the stress-free reference, as no delamination cracks were observed in the y-axis [30]. This logic is applied to the current study, as the 2D weave architecture is similar to the laminate in the fact that there are no 3D interlocks between plies. Therefore, instead of using a crack length from a stress-free material for c_0, the horizontal crack lengths, that run along the x-axis,

produced from the indent will be used for c_0. When using this logic, it can be assumed that the length of the vertical crack along the y-axis will indicate the residual stress state of the matrix material. For example, if the matrix is in residual compressive stress, the vertical crack length will be shorter than that of the horizontal crack, as the residual compression is helping to close the crack growth. On the other hand, if the vertical crack is longer than that of the horizontal crack, then the matrix will be in residual tension, and is helping to open the crack. The last condition occurs when the matrix has no residual stress, and the vertical and horizontal cracks are the same length. A diagram illustrating the three conditions can be seen in Figure 10.

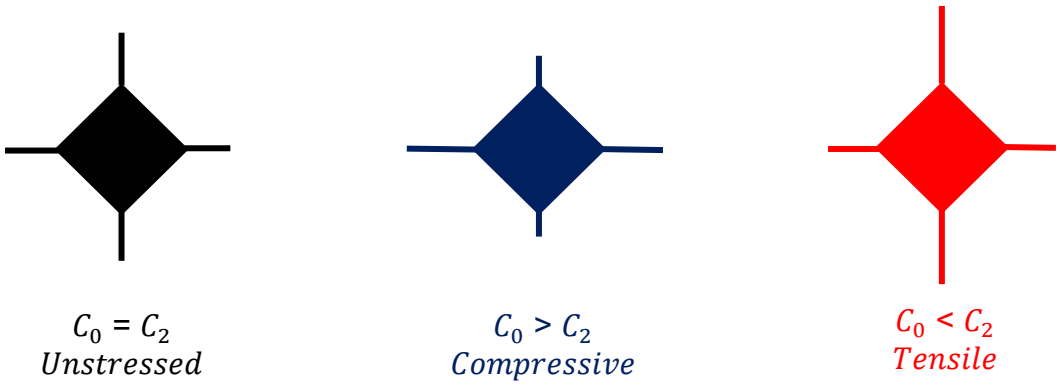

Figure 10: Residual stresses associated with crack indentations

Using this same method, Wing was able to measure residual stresses in a melt infiltrated 0/90 laminate SiC/SiC CMC [30]. Indents were taken in the middle layer of the composite where there was sufficient matrix material, with no other fibers nearby to possibly arrest crack growth and propagation. The first series of samples studied was prepared in such a way that the middle matrix layer was surrounded by two 90 degree plies, and the second set of samples was prepared to have the matrix surrounded with two

0 degree plies. In general, the matrix was found to be in compression in the axial direction. However, the value of the matrix stress was dependent upon the orientation of the plies surrounding it. When surrounded by 90 degree plies, the stress was found to be 63.5 MPa, and when surrounded by 0 degree plies, the stress was found to be 103.4 MPa [30]. The difference in these stresses can be attributed to the difference in the elastic moduli of the 0 and 90 degree plies, with the 90 degree ply having a much lower elastic modulus than the 0 degree ply [30, 35].

2.4.4 Common Intersection Point Method

An experimental method used to determine the axial residual stresses within a CMC is the common intersection point (CIP) method, also known as the hysteresis loop method. In this method, unload-reload cycles are performed on a dogbone specimen during tensile testing [36]. The strain is increased with every reload cycle, resulting in an ultimate failure. The compliance slopes will converge on a common intersection point, whose location is indicative of the residual stress state of the composite [37]. For a specimen with residual compressive stresses in the matrix and residual tensile stresses in the fibers, the CIP occurs at a positive strain and stress. If the CIP does not occur at this location, the curves can be extrapolated into a negative strain and stress region [37]. When the CIP happens in this region, the matrix is under a residual tensile stress and the fibers are under residual compressive stresses. Examples of CIP graphs can be seen in Figure 11 [12] and Figure 12 [37].

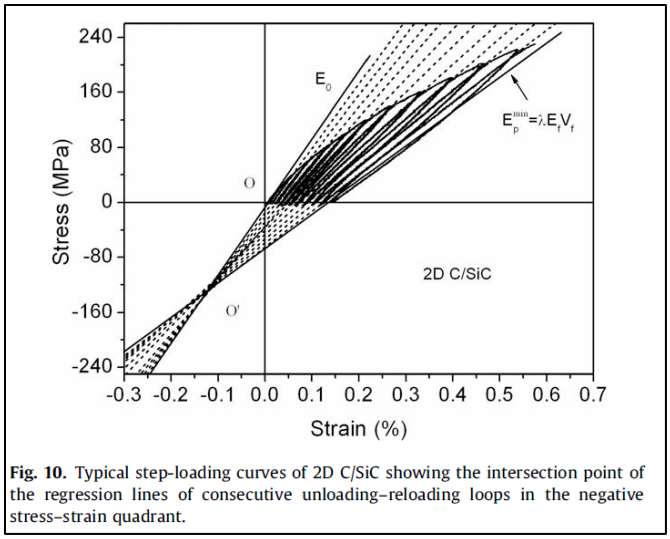

Fig. 10. Typical step-loading curves of 2D C/SiC showing the intersection point of the regression lines of consecutive unloading–reloading loops in the negative stress–strain quadrant.

Figure 11: Common Intersection Point Diagram of 2D C/SiC Composite [12]

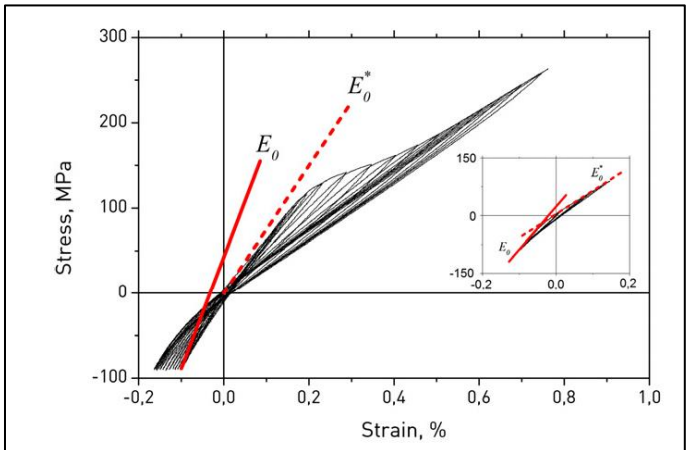

Fig. 4. Effect of translated tensile curve of un-notched specimen on calculated elastic modulus.

Figure 12: Common Intersection Point Diagram of SiC-fiber reinforced CMC [36]

Previous work has been done using the CIP method for other batches of the material used in this study [38]. Mechanical testing was completed on plates of material made with as produced and in-situ BN Sylramic fibers in a MI SiC matrix with a 0/90 layup. The number of plies differed between the plates. There were several key findings from this study. First, the volume fraction between different panels varied significantly

[38]. Therefore, it was necessary to complete volume fraction studies on both plates of material for the present study. Also, specimens from the same panel had little variation in their stress-strain data [38]. Lastly, from using the CIP method, it was found that the matrix was in residual compression, as the CIP occurs in the positive stress-strain quadrant, as seen in Figure 13 [38].

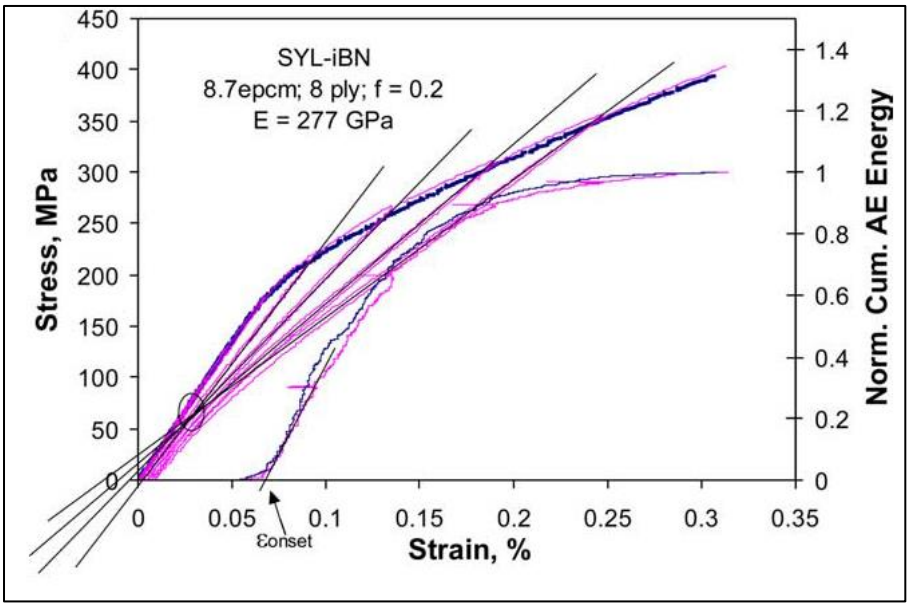

Figure 13: Common Intersection Point for Woven MI SiC/SiC composite [37]

2.5 Annealing

Annealing is a process in which a material is heated to an elevated temperature, quenched, and subsequently cooled [39]. Annealing causes processes that are thermally activated, such as diffusion, to remove defects or rearrange them to have a lower energy [40]. Annealing is used to relieve the residual stresses of the material [39]. Specifically, in ceramics, the thermal residual stresses within the brittle material can weaken it. If the thermal stresses are significant, it can lead to failure through thermal shock [41].

When annealing, time is an important factor that will have a considerable effect on the relief of residual stresses [41]. Increasing the annealing temperature can accelerate the process, as diffusional processes may have an effect on the material [41]. In order to avoid oxidation on the surface of the material, the specimen can be annealed in an atmosphere where no oxidizing will occur, such as in an argon rich furnace [41]. Additionally, there are annealing techniques where samples can be encased in quartz tubes backfilled with argon that can be loaded into a furnace.

2.5.1 Annealing in Silicon

Previous work has been done on annealing silicon. A relationship has been formed between annealing temperatures and residual stresses in monocrystalline silicon wafers [42]. Also, work has been completed on relaxing compressive residual stresses in low pressure CVD polysilicon [43].

When fabricating silicon wafers for use in semiconductors, they are scribed to assist in breaking apart the wafer. This is done by using a diamond scribe or a laser scribe. However, these processes induce residual stresses into the material [42]. Monocrystalline silicon wafers were annealed at temperatures ranging from 300° C to 900° C, with times spanning from thirty minutes to forty hours. It was found that residual stress reduction started occurring at 500° C, and continued until no further reductions occurred at around 700° C [42]. No significantly different trends occurred for longer time cycles [42]. The relationship between the residual stress and annealing temperatures can be seen in Figure 14 [42].

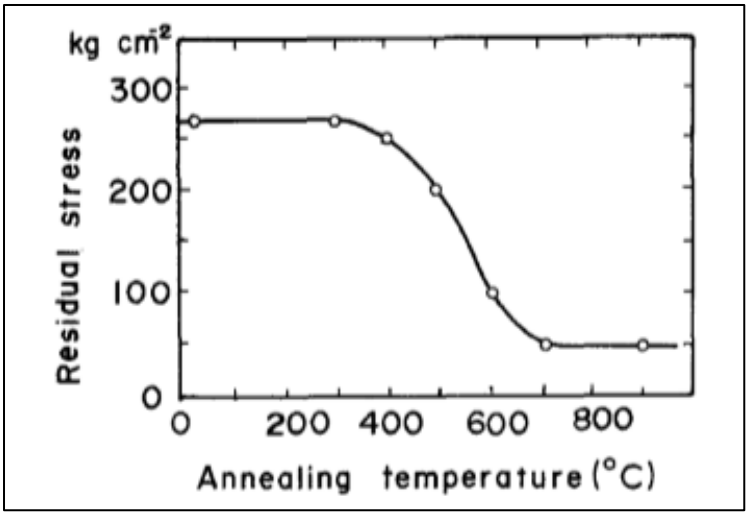

Figure 14: Residual Stress of Silicon Wafer vs. Annealing Temperature [41]

Other annealing work has been completed on low pressure CVD polycrystalline silicon. It was found that when annealing above the deposition temperature, 620° C, residual compressive stresses decrease [43]. The reduction is greater for higher annealing temperatures. The residual stresses almost completely relaxed when the silicon was annealed for two hours at 1100° C [43].

2.5.2 SiC/SiC Composites

Little work has been done on annealing pure silicon carbide. However, there have been previous studies done on annealing SiC, as well as Si, within SiC/SiC composites. Raman measurements were completed on as-manufactured and annealed reaction bonded (RBSiC), which is used in SiC/SiC composites [30]. Mechanical properties, as well as residual stresses, were examined in as-manufactured and annealed dogbone specimens made with HiPerComp™ fibers [44]. Lastly, thermal conductivity and creep strain were compared for as-manufactured and annealed CVI MI SiC/SiC composites.

Using Raman spectroscopy, the microstresses within RBSiC and unreacted Si were measured in monolithic RBSiC and in a MI SiC/SiC composite [30]. Within the monolithic RBSiC, tensile stresses of 2-2.3 GPa were measured, and compressive stresses of 1.7-2 GPa were measured within the Si [30]. Higher compressive residual stresses were measured in the samples containing lower amounts of silicon, with lower tensile residual stresses. Using a modified Kingery-Turner model [45, 46] to account for both thermal residual stresses and silicon expansion, Wing, et. al were able to model a relationship between the silicon volume fraction and residual stresses, but the model overestimated the value of stresses by ~1 GPa for silicon. When measuring the residual stresses within a MI SiC/SiC composite, the same trends occurred. Tensile residual stresses up to 1.7 GPa in the SiC were reported, and compressive residual stresses ranging from 2-3.8 GPa were measured in the unreacted silicon phase [30]. In order to relieve these residual stresses, the composite samples were annealed at a temperature of 1200° C ranging from thirty minutes to eighty hours, and the monolithic RBSiC were annealed from thirty minutes to two hours [30].

In the monolithic RBSiC, there were immediate relaxations in residual stresses for both the Si and SiC phases. There was a 75% reduction on the compressive stresses in the Si phase in thirty minutes, and no further reductions after a total of two hours of annealing [30]. There was also a 33% reduction in the tensile stresses in the SiC, with no noticeable reductions after the first annealing cycle of thirty minutes [30]. The reductions in residual stresses can be seen in Figure 15 [30].

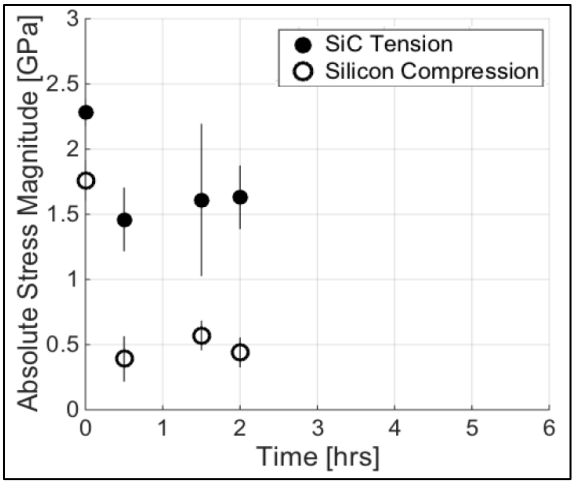

Figure 15: Residual Stress vs. Annealing Time for RBSiC [29]

Similar reduction trends were seen in the composite samples, except at a lower rate [30]. The composite samples saw a 50% reduction in residual stresses after five hours, and a 58% total reduction after eighty hours [30]. Figure 16 illustrates the reductions in residual stresses for the composite samples [30].

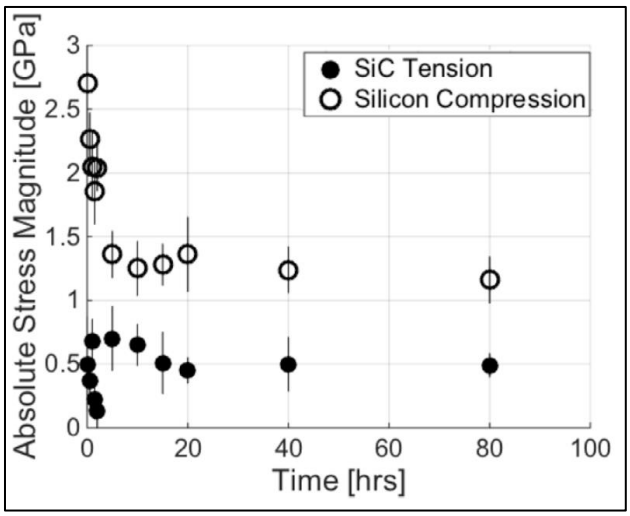

Figure 16: Residual Stress vs. Annealing Time for MI Matrix Material in SiC/SiC composite [29]

Additional work has been completed using both Raman spectroscopy and X-ray diffraction to measure residual stresses within a five-harness satin weave melt-infiltrated CMC produced by Rolls Royce [47]. With Raman spectroscopy, experiments were conducted from room temperature to 1300° C. SiC constituents were found to be in tension, before heat treatment averaging around 270 MPa and 300 MPa after heat treatment. These differences were not statistically significant. The silicon constituents were found to be in compression, and did not change after heat treatment, maintaining a range of 250-500 MPa. In this study, Knauf also noted the presence of Fano resonance due to boron doping, and applied a method relating the half-width of the Fano profile to determine the stress-free wavenumber for that half-width. For surface and subsurface silicon, the stress-free wavenumber averaged near 515 cm^{-1}.

Other work has been completed on annealing dogbone specimens of a SiC/SiC composite with HiPerComp™ fibers, and then performing mechanical testing on the samples [44]. It is important to note that the annealing process is unknown in this study as it was conducted by the manufacturer in post-processing. When comparing the mechanical data for as-manufactured and annealed dogbone specimens, it was found that there is no reduction in the elastic modulus [44]. However, a reduction in both the proportional limit stress as well as the ultimate stress was reported [44]. These trends can be seen in Figure 17. In order to estimate the reduction of compressive residual stresses within the matrix, acoustic emission (AE) was used to detect the stress at which the first crack initiated within the matrix [44]. It was found that for a cross-ply sample, annealing caused an average of a 75 MPa reduction in the compressive stress within the matrix [44].

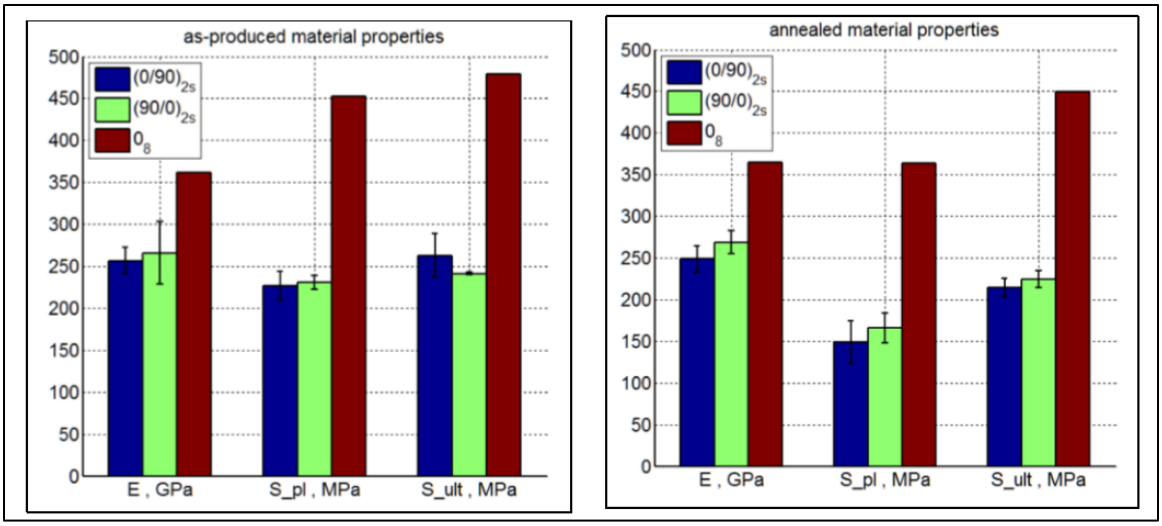

Figure 17: Trends for Elastic Modulus, Proportional Limit Stress, and Ultimate Stress for as-manufactured and annealed specimens [43]

Lastly, NASA developed a thermal treatment technique to obtain better thermomechanical properties for CVI MI SiC/SiC composites [48]. After the CVI process and before adding any MI material, the composite went through an annealing heat treatment [48]. By adding this step, the thermal conductivity and the creep resistance was improved for the material, as seen in Figure 18 [48]. By increasing the thermal conductivity of the material through annealing, the thermal stresses from thermal gradients will be reduced [48]. Also, increasing the creep resistance of the material will allow for a longer life cycle of the component [48].

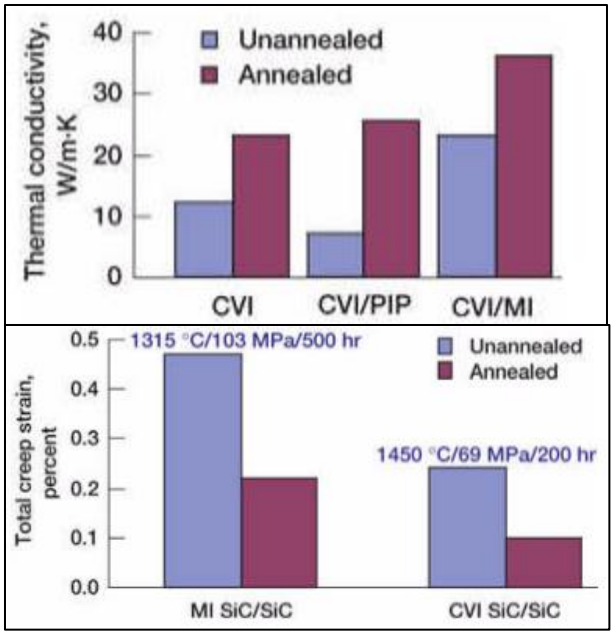

Figure 18: Improvement in thermal conductivity and creep resistance of annealed specimens [46]

III. MATERIALS AND METHODS

This chapter will describe the materials used and outline the testing methodology for this study. First, a description of the two plates of material will be given along with historical mechanical testing information. Then, the testing procedures for volume fraction, annealing, mechanical testing, crack indentation, and Raman spectroscopy will be given.

3.1 Material Information

The material investigated in this study was supplied by the Air Force Research Laboratory, and was produced by Honeywell Advanced Composites in 2001. Two plates were provided, each processed slightly different from the other. The plates have a SiC matrix, with residual silicon, containing continuous Sylramic and Sylramic-iBN SiC fibers.

3.1.1 Material Orientation

The fibers were first woven into five-harness satin weave plies. Various types of weave patterns are imaged in Figure 19, including the five-harness satin weave [7]. The warp direction is typically referred to as the longitudinal direction of the material, and is the direction of fibers that are held in tension that the transverse fibers are woven around. The fibers that are woven into the warp are called weft or fill. In Figure 19, the dark grey

fibers are in the warp direction and the light grey fibers are in the weft direction. The plies were laid up into a 2D weave with a $[0/90/0]_{sym}$ orientation with regards to the warp direction. The 2D weave has many advantages, including high in-plane properties and its ability to be formed into complex shapes [7]. However, the out-of-plane and transverse properties are much lower than the in-plane properties [7]. The five-harness satin weave pattern can be seen on the surface of a sample in Figure 20.

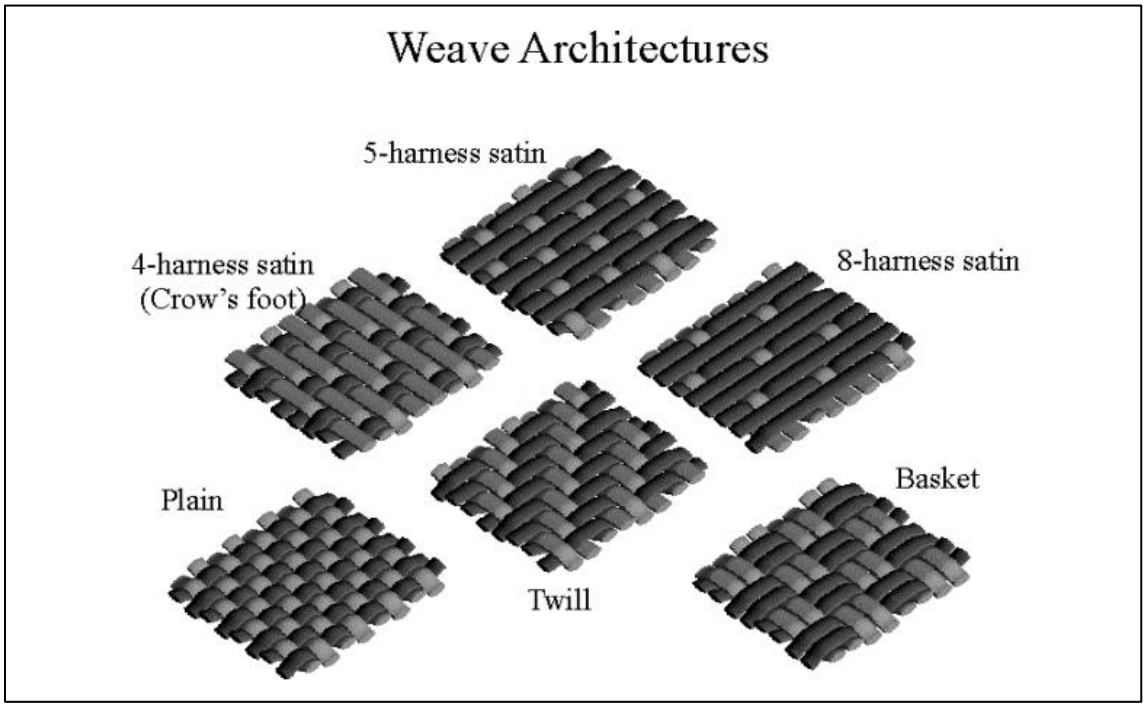

Figure 19: Various weave architectures used for ceramic matrix composites [7]

Figure 20: Five-harness satin weave pattern seen on surface of sample

3.1.2 Sylramic Fibers

In SiC/SiC CMCs, SiC fibers are used. These fibers are produced by curing and heat treating material from polymer precursors. When taken through the heat treatment, which causes impurities to decompose, the polymer precursor converts into ceramic silicon-carbide fibers [11]. The two plates contain fibers produced by COI ceramics. Plate 1 contains the original Sylramic fiber, while Plate 2 contains the variant Sylramic-iBN fiber, made to improve upon the original. Both the Sylramic and Sylramic-iBN fibers are advertised as having diameters of 10 microns, and once sized can be woven into fiber preforms [49].

In both fibers, boron was added into the fiber's microstructure as a sintering aid to produce fibers with higher tensile strength, and the fibers were sintered at 1600° C after going through the heat treatment process [3, 11]. By adding the sintering aids during processing, the resulting fiber is more dense with a higher tensile strength than non-sintered fibers [11]. However, the boron sintering aids in Sylramic fibers remain after processing, while an additional heat treatment is performed during the processing of the Sylramic-iBN fibers to remove the boron sintering aids. This additional heat treatment in processing of the Sylramic-iBN fibers diffuses the boron to the surface resulting in improved creep resistance and electrical conductivity, while retaining the fiber tensile strength [3, 50]. The boron is diffused to the surface in a nitrogen rich environment, resulting in an in-situ boron nitride (iBN) fiber coating to form. This coating prevents direct contact between the SiC fibers when laid up in the fiber preform. By avoiding direct SiC-SiC contact, the fibers will not bond to one another during subsequent high temperature processing steps. If the fibers do bond, which happens when using the

Sylramic fibers, it is seen as a defect in the composite, and the points of contact will become areas of stress concentration. Once these areas fail, it will not only result in the original fiber from fragmenting, but it will also result in the failure of the fibers bonded to it. In addition to preventing fiber to fiber bonding, the iBN fiber coatings provide increased oxidation resistance [3, 50].

3.1.3 Sample Processing

For Plate 1, the fiber preforms first went through CVI of boron nitride [3]. This preform was then placed into a CVI SiC reactor [3]. After going through the CVI processes, a SiC particulate was infiltrated into any of the remaining porosity at room temperature [3]. Following this, silicon metal, at 1400° C, was melt infiltrated into the fiber preform [3]. The silicon reacted with excess carbon to form silicon carbide. This process resulted in a low porosity for the matrix material [3]. The processing for this material is outlined in Figure 21.

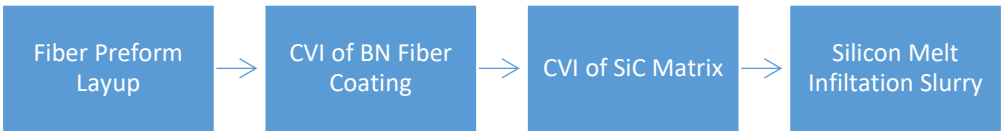

Figure 21: Processing Steps for Plate 1

For Plate 2, the fiber preform went through a similar process, with one major change. Before any CVI or MI, the fiber preform went through another thermal treatment, developed by NASA [3, 11, 50]. The heat treatment forced the excess boron, from the sintering aids, to diffuse to the surface and interact with nitrogen in the environment, creating an in-situ boron nitride (iSBN) fiber coating around the fibers [3,

19, 50]. The fiber preform then went through the same CVI and MI process as the previous plate. The processing steps for Plate 2 are listed in Figure 22. The comparison of the different contact areas of fibers for the two plates can be seen in Figure 23 [3].

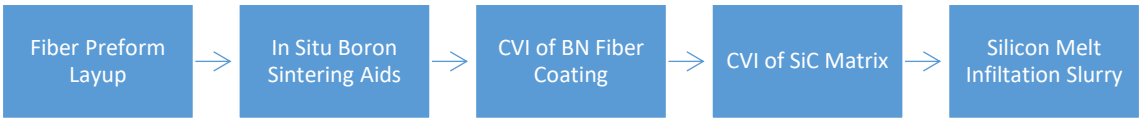

Figure 22: Processing Steps for Plate 2

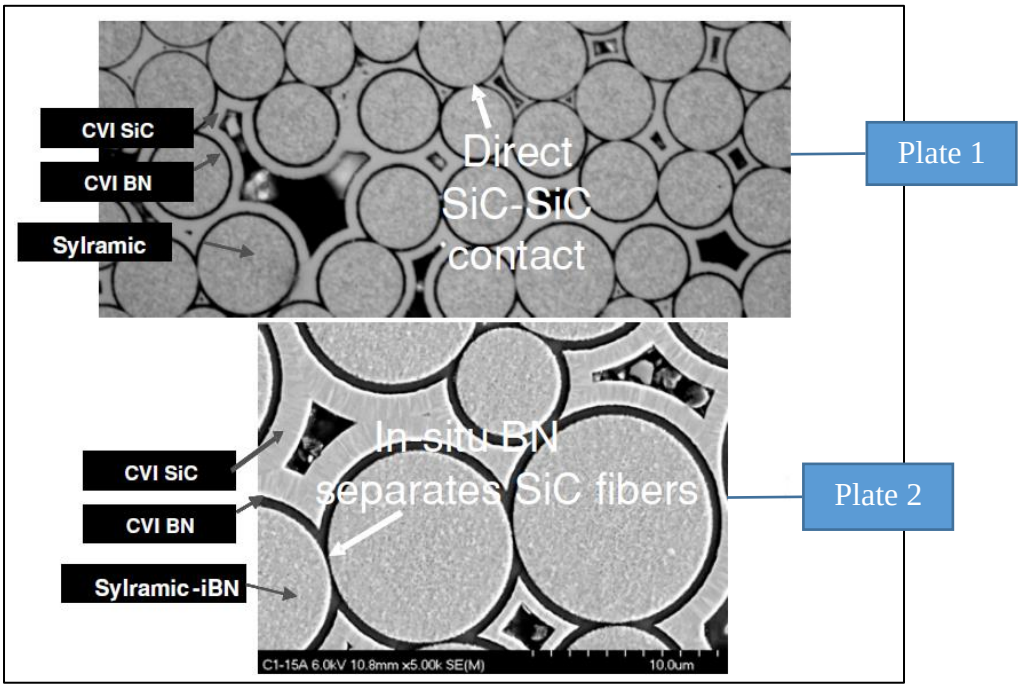

Figure 23: With the in-situ boron nitride coating, the SiC fibers are separated from one another [3]

3.2 Historical Mechanical Testing

Mechanical testing performed on the samples at Honeywell Advanced Composites testing facility. The properties in Table 5 were from tension tests in a room temperature [51]. Example stress-strain plots for these tests can be found in Figures 24 and 25. It is important to note that no information could be found on the loading or strain rate of these tests, the grip pressures, etc. Therefore, this data could not be used as baseline data for the current study.

Table 5: Mechanical Properties of Honeywell Material [51]

		Peak Stress (MPa)	Peak Strain (%)	Proportional Limit (MPa)	Elastic Modulus (GPa)
Plate 1	Sample 1	250	.2546	150	209
	Sample 2	292	.3234	165	192
Plate 2	Sample 1	447	.5814	180	198
	Sample 2	398	.5384	150	199

In Figure 24, the stress-strain plot is shown for Sample 1 of Plate 1. The peak stress value is at 250 MPa, with a proportional limit of 150 MPa. The elastic modulus of the specimen was measured at 209 GPa.

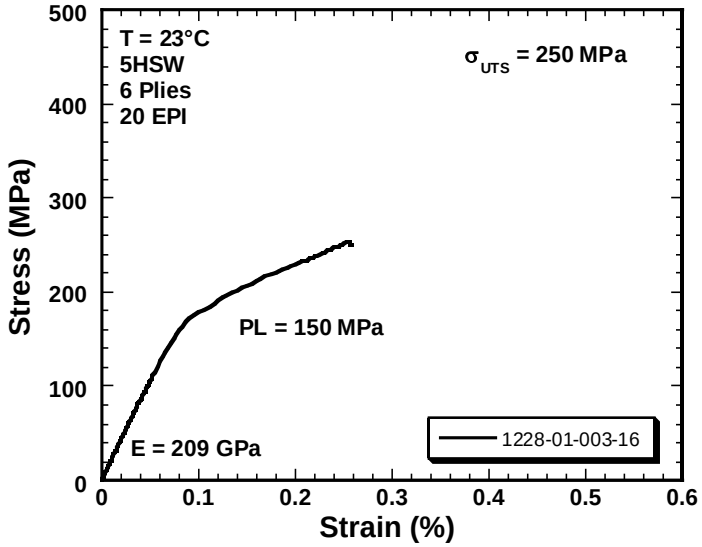

Figure 24: Stress-Strain Plot of Plate 1 Sample 1 from a Tension Test of MI Sylramic Material

In Figure 25, the stress-strain plot is shown for Sample 1 of Plate 2. The peak stress value is at 447 MPa, with a proportional limit of 180 MPa. The elastic modulus of the specimen was measured to be 198 GPa.

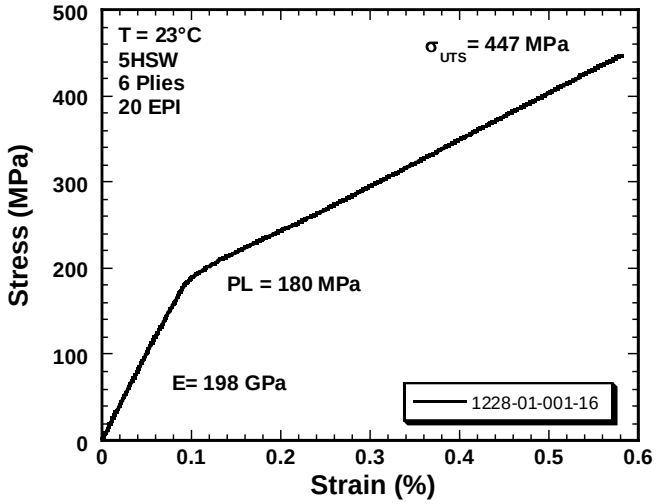

Figure 25: Stress-Strain Plot of Plate 2 Sample 1 from a tension test of iBN MI Sylramic Material

The differences in the mechanical properties for the two plates have only been attributed to the different processing techniques used for each plate and its effect on the composite microstructure. The material for Plate 1 had a degraded ultimate tensile strength, due to excess boron on the fiber surface aiding silica based glass formation when the composite was processed in an oxygen rich environment [3]. When the glass formed, neighboring fibers were bonded, resulting in the reduced ultimate tensile stress [3]. The boron on the fiber bulk usually occurred at the fiber grain boundaries, resulting in reduced creep resistance, rupture resistance, and thermal conductivity [3]. These issues were alleviated in the Plate 2 material by employing the previously mentioned technique developed by NASA, by diffusing the mobile boron sintering aids to the surface of the fiber, resulting in improved mechanical properties [3].

No studies have been completed on the differences in residual stresses between the two plates, previously. Through this study, the residual stresses within the plates will be tested through various methods, with resolutions ranging on the micron scale to the macro scale. It is the goal of this study to note any differences in residual stresses between the two plates through a variety of annealing cycles.

3.3 Testing Overview

First, matchstick specimens were made in order to study the microstructure of both plates. A volume fraction analysis was completed to find the percentage of fibers, CVI SiC, and matrix material. This will be discussed in Section 3.4.

Dogbone specimens from each plate were used for mechanical testing. Two mechanical testing runs were completed to acquire the necessary data. The procedures for these test runs can be found in Section 3.6. Baseline tension testing to failure was completed for room temperature and high temperature conditions first. Then, dogbone specimens were annealed for ten hours at 1315° C and then tested to failure at room temperature. The annealing procedure can be found in Section 3.5.

Eight specimens were cut from each plate for indentation testing to induce crack to estimate the residual stress state. The first four samples from each plate were mounting and polishing without any additional heat treatment. The second set of four from each plate were annealed for ten hours at 1315° C, and then mounted and polished. Both the as-received and heat treated samples were then tested using the same procedure outlined in Section 3.7.

Four specimens were cut from each plate for characterization with Raman spectroscopy. For the first set of samples, Raman scans were performed around three fibers from each specimen. The specimens were then annealed at 1150° C and 1315° C as done for the previous tests. This test matrix summarized in Section 3.8. The procedure was then repeated until the specimen was annealed for a total of five hours. For the second set of specimens, one fiber, two matrix areas, and two silicon veins were characterized using Raman spectroscopy. First, the areas were scanned prior to annealing, and then scanned again after being annealed for ten hours at 1315° C.

3.4 Volume Fraction

3.4.1 Testing Apparatus

Within the ImageJ image processing software, the CellCounter Analysis feature was used, along with gridlines, to conduct a volume fraction study. This feature, along with an image, is pictured in Figure 26.

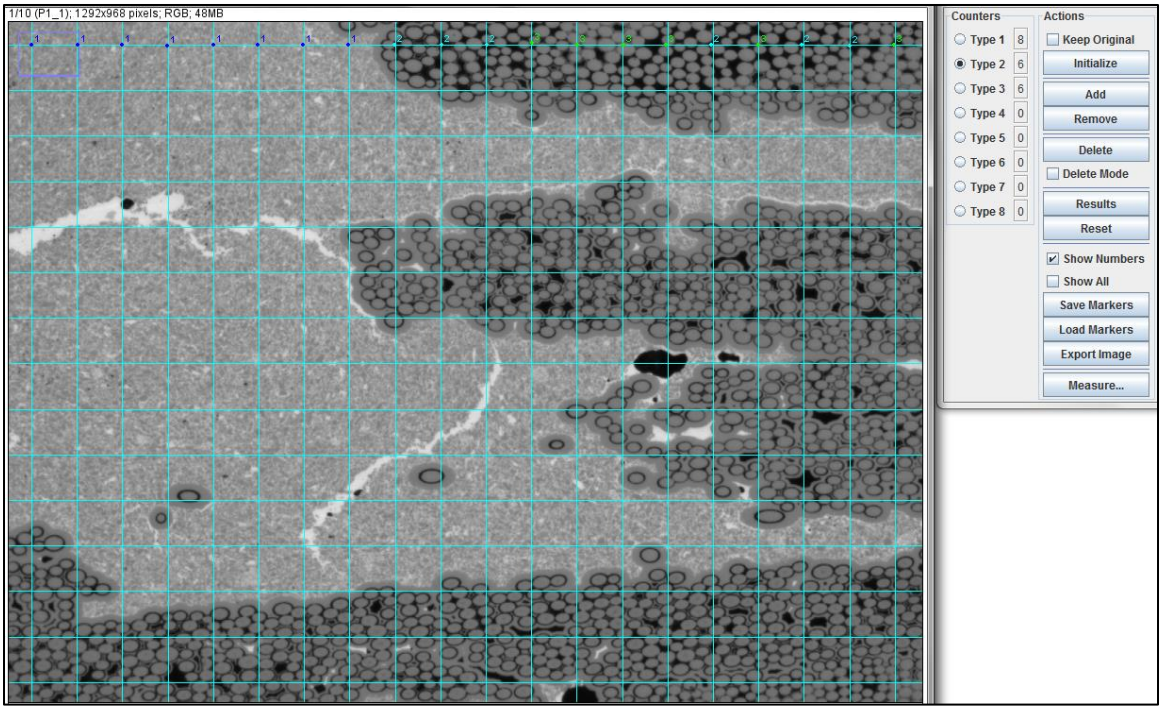

Figure 26: ImageJ Cell Counter Feature and Volume Fraction Image

3.4.2 General Procedure

The volume fraction was found according to ASTM E562-11 [52]. Using an image of a ±45º cut sample taken at 100x, the total number of fibers in the image was counted. Then, using an average diameter of the fibers to calculate the area, the total volume fraction of the fibers in the image was found. A convergence study was then conducted using various grid sizes in order to find the proper grid spacing. When using the optimal grid spacing, wherever a gridline intersection occurred, the point was taken either as a fiber, CVI SiC, porosity, or matrix material. These values were then divided over the total number of points to find the volume fraction of each constituent. The BN fiber coatings were not considered during point counting, as their volume fraction is minimal. If a grid point landed in the middle of a fiber coating and fiber, the point was counted as a fiber.

3.5 Annealing Procedures

3.5.1 Testing Apparatus

The dogbone specimens employed for mechanical testing and the matchstick specimens characterized by Raman spectroscopy were annealed in a front-loading furnace. When using an inert gas, such as Argon, the furnace can reach temperatures of up to 2500° C. The temperature was measured using two C-type thermocouples when under 1600º C. When temperatures exceed 1600º C, an infrared optical pyrometer tracked the temperature. The furnace was heated with a graphite heating element surrounded by fibrous graphite insulation. The furnace was purged to vacuum, and then backfilled with argon to a low positive pressure. This was done a total of three times, with argon constantly purging the furnace system throughout at 2 psi. Once the system was purged, the furnace was engaged to achieve the desired temperature. When the cycle was complete, the furnace was allowed to cool down to room temperature without intervention. When room temperature was reached, the vacuum was released.

3.5.2 General Procedure

The dogbone specimens were heated to 1315º C at a rate of 40° C/min. For each plate, two specimens were placed into the furnace for ten hours. Only one specimen was placed into the furnace at the time to avoid large amounts of outgassing from the specimens.

The matchstick specimens were heated to both 1150º C and 1315º C at a rate of 40° C/min. For the first cycle, the specimens were held at a constant temperature for fifteen minutes. The initial annealing cycle for fifteen minutes is seen in Figure 27.

After conducting Raman spectroscopy on the specimens, the cycle was then repeated for another fifteen minutes after which the material was again characterized with Raman spectroscopy. This regimen was repeated with the same specimens, for up to a total time of five hours for each temperature. Also, after studying the original data, another anneal was performed on an additional set of specimens for ten hours without interruption at 1315º C.

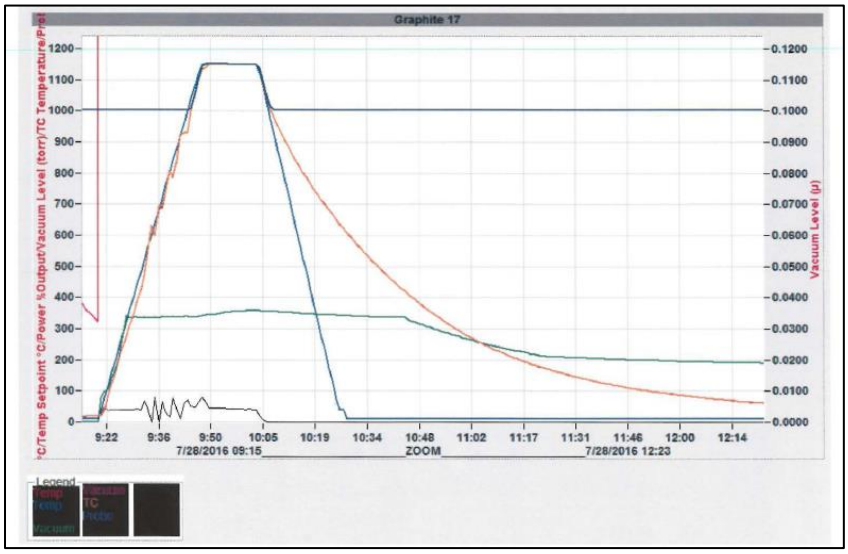

Figure 27: Initial Annealing Cycle for Matchstick Specimens at 1150º C

3.6 Indentation Cracking

Using a hardness tester, indentation was performed on four samples from each plate, per the testing matrix seen in Table 6.

Table 6: Crack Indentation Testing Matrix

	Number of Samples	Condition
Plate 1	2	No anneal
	2	Annealed for 10 hours at 1315º C
Plate 2	2	No anneal
	2	Annealed for 10 hours at 1315º C

3.6.1 Sample Geometry and Preparation

Four 12 mm x 2 mm x 2 mm samples were cut from each plate, with a low concentration diamond sawblade, from each of the as-manufactured plates produced by Honeywell. Two of the samples from each plate were then annealed for ten hours at 1315º C using the annealing procedure described in Section 3.5. The samples were then mounted and polished with diamond embedded plates to a three-micron finish.

3.6.2 Testing Apparatus

A Buehler Vickers indentation machine was employed to apply indents to the samples. An optical microscope with 20x and 50x objectives is connected to the indentation machine, allowing for precise placement of the indenter. The indentation machine is equipped with a 10, 100, 500, and 1000 g load cell.

3.6.3 General Procedure

A 1000-gram load was applied for ten seconds in order to induce cracks. Lower loads were attempted, but no measurable cracks were produced until the 1000-gram load cell was engaged. Using crosshairs visible through the optical lenses, the crack length was measured, as well as the size of the indent. Only matrix rich regions were studied with no neighboring fibers that could have possibly impeded crack growth. The size of the indent was used to calculate the hardness of the samples, per Equation 5 [49]:

$$Hardness\ Value = \frac{Test\ Load}{Surface\ Area\ of\ Indentation}$$

Equation 5

The estimated residual stresses were calculated using Equation 4 in Section 2.4.3. A value of 3 MPa $\sqrt{m}$ [53] was used for the fracture toughness of the matrix material.

3.7 Mechanical Testing

Four samples from each plate were tested using standard tensile testing procedures. First, one specimen from each plate was tested in the Rapid Heating Investigation of Materials Laboratory (RHINO lab) at Wright-Patterson Air Force Base. The next three specimens were tested in the Materials and Manufacturing Directorate (MMD lab) of the Air Force Research Laboratory. The different testing conditions for the specimens are listed in Table 7.

Table 7: Mechanical Testing Matrix

	Number of Samples	**Condition**	**Testing Location**
Plate 1	1	Room Temperature Testing, no anneal	RHINO lab
	1	Room Temperature Testing, no anneal	MMD lab
	2	Room Temperature Testing, Annealed for 10 hours at 1315º C	MMD lab
Plate 2	1	Room Temperature Testing, no anneal	RHINO lab
	1	Room Temperature Testing, no anneal	MMD lab
	2	Room Temperature Testing, Annealed for 10 hours at 1315º C	MMD lab

3.7.1 Sample Geometry and Preparation

Dogbone specimens of both plates were cut with the same geometry. The specimens were 154 mm in length, with the gage section being 28 mm in length. The

radius of the gage section was machined to be 50 mm. The specimens were to have a thickness of 2 mm; however, there was variation in this thickness due to the weave geometry. Using a machinist's microscope at 20x, the exact dimensions of each specimen were measured, and used to calculate stresses. The specimen geometry can be seen in Figure 28.

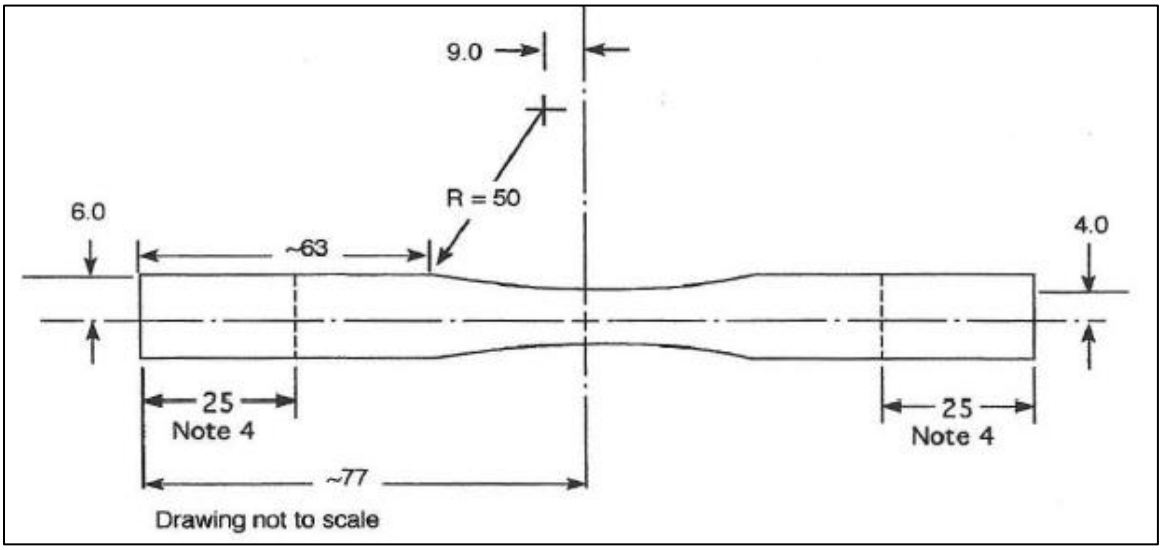

Figure 28: Dogbone Specimen Geometry (units in millimeters)

Fiberglass tabs were adhered to the specimen in the grip section to avoid early cracking in the grip section. For the specimens tested at the RHINO lab, the gage section of each specimen was speckle patterned with a Ceramabond™ blackbody surface and a Ceramabond™ alumina speckle to obtain Digital Image Correlation (DIC) strain measurements. This was not done for the tests completed at the MMD lab.

3.7.2 Testing Apparatus

At the RHINO lab, an MTS® tension testing system was used to apply load to the specimens. DIC cameras were positioned in front of the specimen to track changes in the

strain on the front surface of the specimen. Acoustic Emission (AE) sensors were placed on the edge of the tab sections of the specimen to track crack propagation within the specimen. The testing setup is imaged in Figure 29.

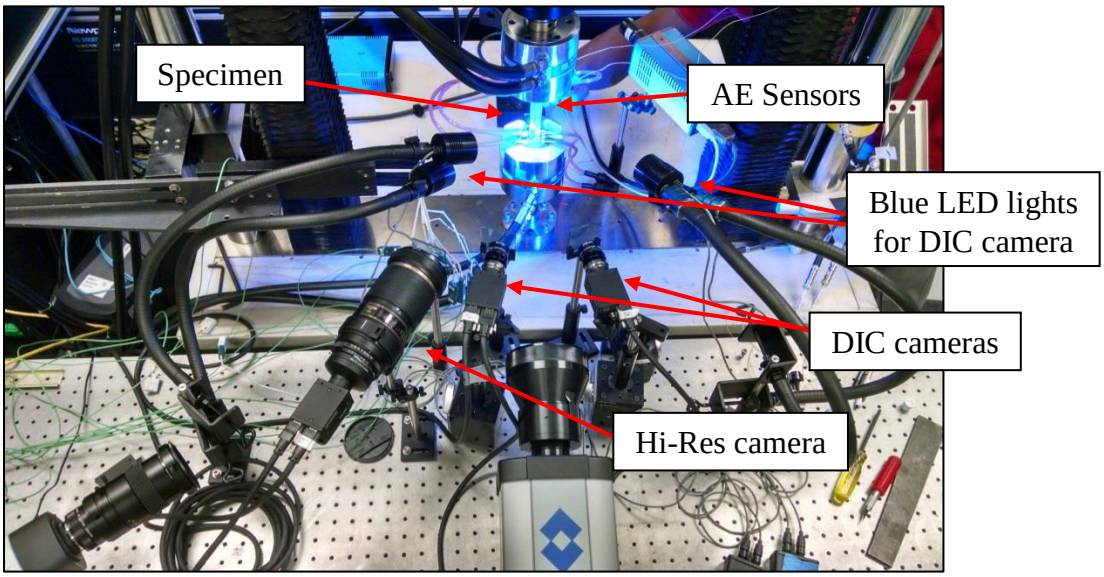

Figure 29: RHINO Lab Testing Configuration

At the MMD lab, a horizontal MTS® tension testing machine was used. Instead of DIC cameras, a ½ inch Epsilon room temperature knife edge extensometer was used to track strain. AE sensors were placed on the top surface and along the tab edges to detect crack propagation during testing. The testing configuration can be seen in Figure 30.

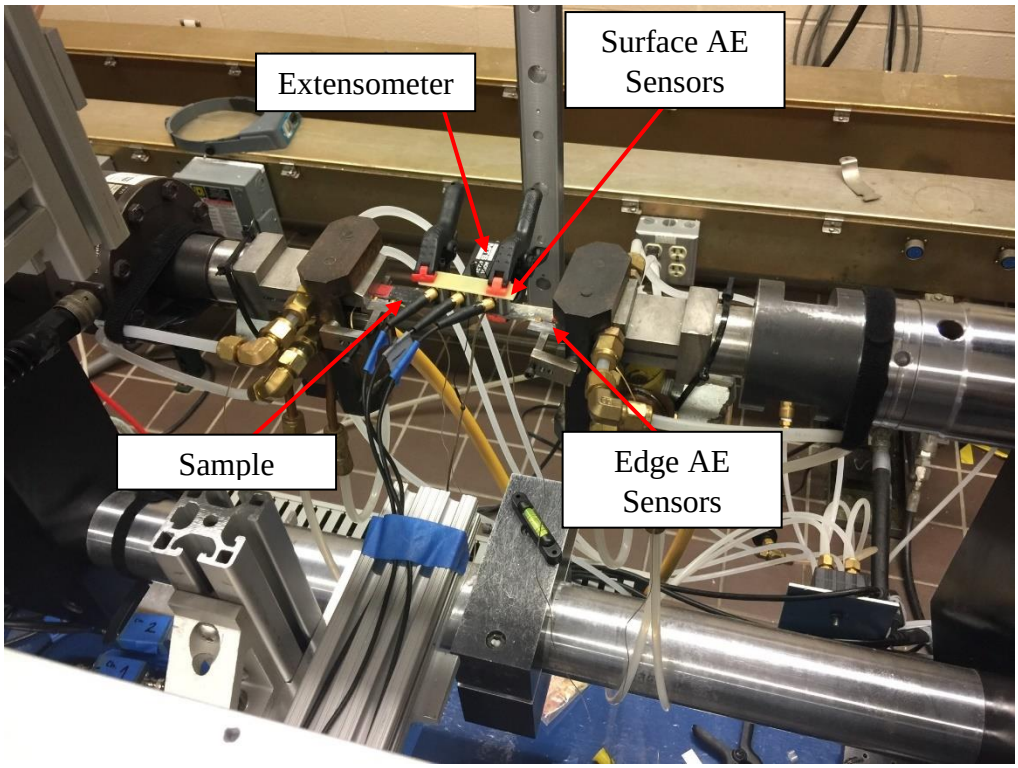

Figure 30: Testing Configuration at the MMD lab

3.7.3 General Procedure

When testing at the RHINO lab, the specimens were first aligned within the test machine. The AE sensors were placed on the specimen, and the DIC cameras were focused on the speckle pattern of the specimen. After conducting equipment checks, the specimen was loaded to failure under stroke control with a test rate of 0.001 mm/s. Following testing, the AE data was analyzed using MATLAB code [54]. The DIC data was analyzed via VIC 3D DIC software.

At the MMD lab, the specimens were placed into the test machine and aligned in the center. Then, the extensometer was attached to the gage section of the specimen using rubber bands. Couplant gel, used to assist in the travel of acoustic waves from the sample to the sensor, was applied to areas where AE sensors were to be placed, and then

the AE sensors were gripped onto the specimen. Then, at least three modulus checks were performed before the specimens were tested to failure under stroke control rate at a loading rate of 0.001 mm/s. The data obtained from the extensometer and tension machine were analyzed in Excel, and the AE data was analyzed using a MATLAB code.

3.8 Raman Testing

Three major test runs were completed for Raman testing. The first test run was done for samples annealed at 1150° C in a cyclic manner to five hours. Then, the same test run was completed, but for samples annealed at 1315° C. The testing matrix for these two runs can be seen in Table 8. Another test run was done at 1315° C, but completed for ten hours straight, instead of cyclic annealing. The test matrix for this can be seen in Table 9.

Table 8: Raman Testing Test Matrix ran at both 1150° C and 1315° C

	Number of Samples	**Testing Condition**
Plate 1	1, 3 fibers	no anneal
	1, 3 fibers	15 minute anneal
	1, 3 fibers	30 minute anneal
	1, 3 fibers	60 minute anneal
	1, 3 fibers	120 minute anneal
	1, 3 fibers	180 minute anneal
	1, 3 fibers	240 minute anneal
	1, 3 fibers	300 minute anneal
Plate 2	1, 3 fibers	no anneal
	1, 3 fibers	15 minute anneal
	1, 3 fibers	30 minute anneal
	1, 3 fibers	120 minute anneal
	1, 3 fibers	180 minute anneal
	1, 3 fibers	240 minute anneal
	1, 3 fibers	300 minute anneal

Table 9: Raman Testing Matrix ran at 1315° C

	Number of Samples	Testing Condition
Plate 1	1 fiber 2 silicon pools 2 free matrix areas	no anneal
	1 fiber 2 silicon pools 2 free matrix areas	600 minute anneal
Plate 2	1 fiber 2 silicon pools 2 free matrix areas	no anneal
	1 fiber 2 silicon pools 2 free matrix areas	600 minute anneal

3.8.1 Sample Geometry and Preparation

3 12 mm x 2 mm x 2 mm sample was cut, using a low concentration diamond sawblade, from each of the as-manufactured plates produced by Honeywell. The samples were then mounted and polished using diamond embedded plates to a one-micron finish, as pictured in Figure 31. It is important to note that the samples were then unmounted for Raman testing in order to avoid inducing any extraneous stresses. After initial Raman testing, the samples were annealed according to the cycles seen in Tables 8 and 9.

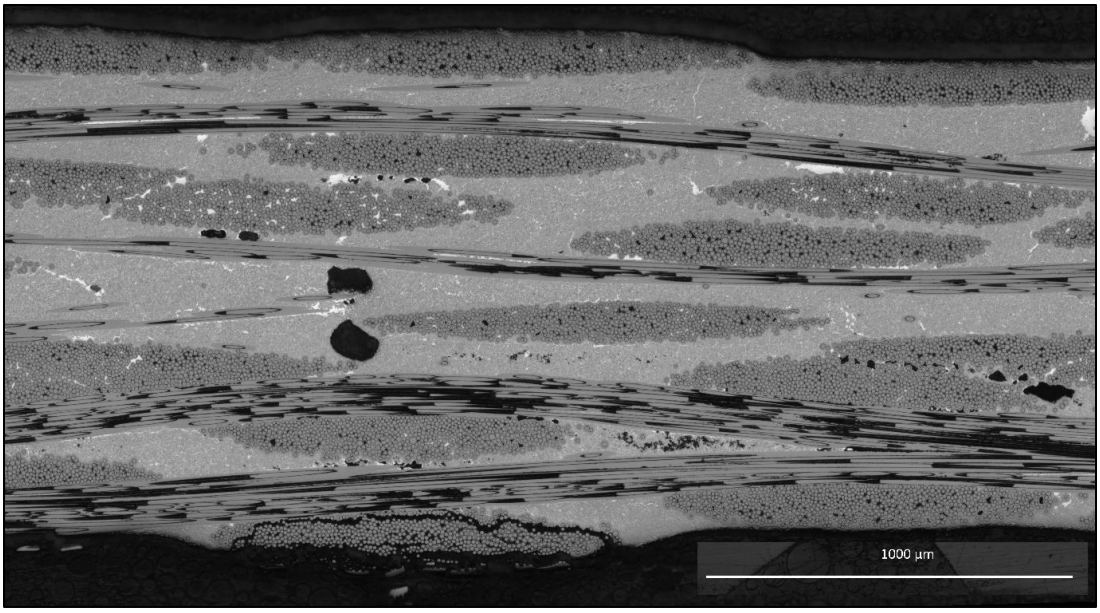

Figure 31: Plate 2 Micrograph Polished to 1 Micron Finish

3.8.2 Testing Apparatus

Raman spectra were then collected on the material using a Renishaw 2000 system equipped with a 514.5 nm excitation Ar^+ laser, a 1800 line/mm grating, and a back depleted CCD for data collection. Laser power at the sample was kept below 2 mW to avoid sample heating. A 50x objective was utilized to focus on the sample. A motorized stage was used in order to map the sample. The signals were detected with a CCD camera.

3.8.3 Curve Fitting

After the Raman signals are obtained, curve fits were applied to the spectrum to identify peaks. SiC and carbon peaks were fit using Renishaw Wire 4.1 software, and were fit with Lorentzian curves. Typically, silicon can be fit in a similar manner. However, during the initial Raman spectroscopy scans, it was seen that an effect called Fano Resonance was occurring within the silicon peaks.

Before MI processing, low amounts of dopants, including boron, were added to the silicon to form a silicon alloy [6]. While the exact nature of these additional constituents is unknown, it results in the Fano effect on the silicon peaks collected with Raman spectroscopy. When semiconductors, such as silicon, are doped, the resulting carrier concentration induces a broad scattering background that overlaps with the typical silicon curve [55]. This results in an asymmetric spectral curve around the silicon peak. To properly characterize the asymmetric peak, the Fano background must be fit along with Lorentzian curves. The equation employed to fit the Fano background is given in Equation 6 [55]:

$$I(\omega) = I_0 \frac{(Q_F + \eta)^2}{(1 + \eta^2)}$$

Equation 6

where η is equal to Equation 7 [55]:

$$\eta = \frac{\omega - \omega_0}{\Gamma_F}$$

Equation 7

The constants for Equation 6 and Equation 7 can be seen in Table 10.

Table 10: Fano Equation Constants

Constant	**Property**
I_0	Fitting prefactor
Q_F	Fano asymmetry factor
η	Reduced frequency
Γ_F	Fano broadening factor

ω	Wavenumber
ω_0	Wave center

3.8.4 General Procedure

As previously mentioned, there were two sets of annealing conditions for the specimens characterized by Raman spectroscopy. First, specimens were annealed in a cyclic manner for a total of five hours as done in the previous experiments. In order to stay consistent throughout testing, three areas were chosen from each of the samples where Raman maps were collected. The same areas were scanned after each anneal cycle. Specifically, the areas characterized with Raman spectroscopy consisted of a single fiber located in the left, middle, and right sides of each sample, respectively. In each case, the fiber was surrounded by matrix material in the middle tow. An example of a location were the Raman map was collected on a sample can be seen in Figure 32.

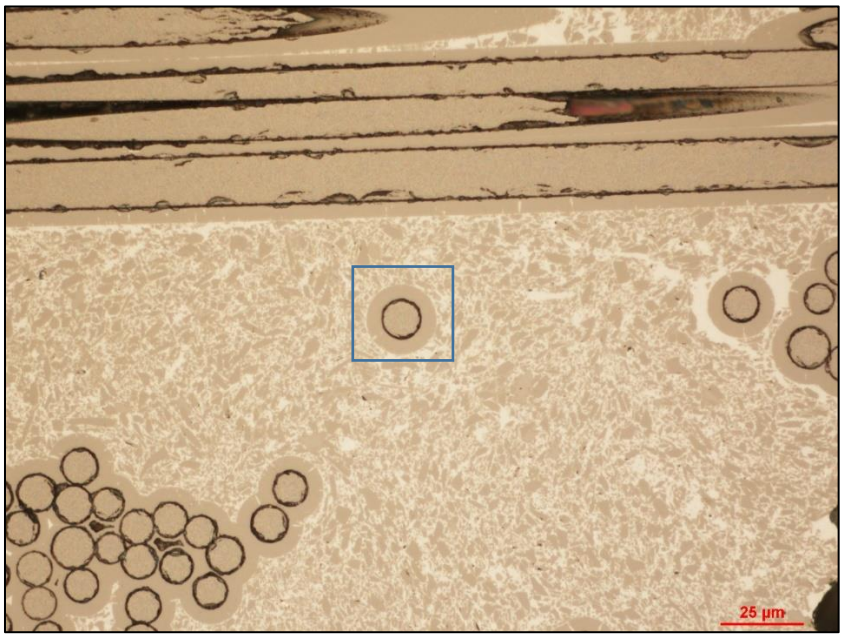

Figure 32: Example of Fiber characterized via Raman Spectroscopy

Different characteristic areas were chosen for characterization by Raman spectroscopy in the second set of specimens studied. Additionally, a different annealing cycle was applied. The areas mapped with Raman spectroscopy in this case included two silicon veins, one fiber, and two free matrix areas. After an initial scan before any annealing, the specimens were annealed for ten hours straight at 1315º C after which a second scan was performed.

The maps collected using Raman spectroscopy were performed via high resolution streamline scans with a 1-micron step size. The data collected was then imported into MATLAB®, which estimated the chemical composition and residual stress and output respective maps of the area analyzed. The composition maps were estimated based off the peak areas for Si, SiC, and C. The stress maps were derived from Equation 3 in Section 2.4.1. For Si and SiC, the stress data reported included the average, maximum, and standard deviations. An example of the plots created can be seen in Figure 33.

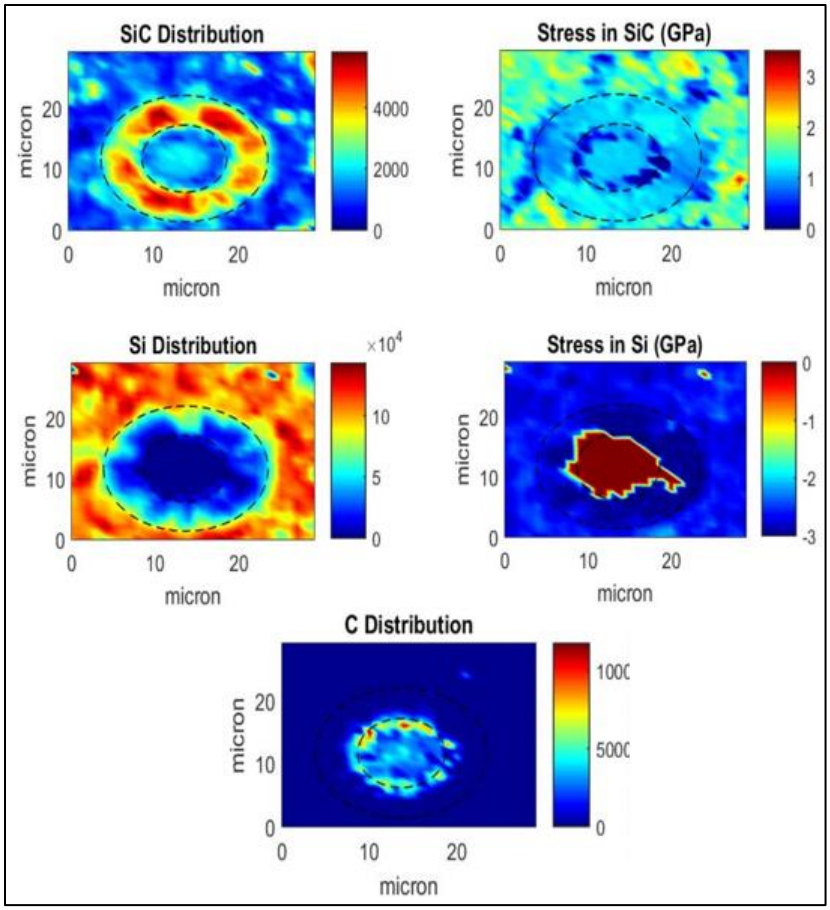

Figure 33: Raman Composition and Stress Maps produced from MATLAB

IV. RESULTS

This chapter will focus on the findings of this study. First, the volume fraction results of both plates will be discussed. Next, the calculation of the theoretical residual stresses will be presented. The findings of the indentation testing will be discussed. Then, the results of the mechanical testing will then be described for room temperature, high temperature, and annealed specimens. Lastly, the results for Raman spectroscopy will be discussed.

4.1 Volume Fraction Results

Using the point counting method described in Section 3.4, the volume fraction of each plate was found. The results for Plate 1 are listed in Table 11.

Table 11: Plate 1 Volume Fraction

Constituent	**Volume Fraction**
MI Matrix	.35
CVI SiC	.19
Fiber	.41
Porosity	.05

The volume fraction results for Plate 2 are listed in Table 12.

Table 12: Plate 2 Volume Fraction

Constituent	**Volume Fraction**
MI Matrix	.29
CVI SiC	.22
Fiber	.46
Porosity	.03

4.2 Theoretical Macro-Residual Stress Calculations

In order to calculate the theoretical residual stress of the matrix, Equation 1 from Section 2.3.1 was used. The constituent properties used for the calculations for the axial residual stresses in both plates are listed in Table 13.

Table 13: Constituent Properties

Material	**CTE (10^{-6}/°C)**	**Elastic modulus (GPa)**	**Poisson's Ratio**
Si At 1400ºC	2.69 [9]	165 [56] 123.75 [56-59]	0.27 [60]
C- SiC	2.77 [61]	390 [62]	0.17
MI SiC	4.7 [63]	310 [63]	n/a
CVI SiC	4.6 [63]	380 [63]	n/a
Sylramic Fiber	5.4 [64]	400 [65-67]	0.17 [66, 67]
Sylramic-iBN Fiber	5.4 [64]	400 [65-67]	0.17 [66, 67]

To account for both the MI SiC and CVI SiC portions of the matrix, a simple rule of mixtures, seen in Equation 8, was followed to calculate the elastic modulus of the matrix, and similarly the CTE of the matrix:

$$E_m = \frac{E_{CVI} * V_{CVI} + E_{MI} * V_{MI}}{V_{CVI} + V_{MI}}$$

Equation 8

The code for these calculations can be found in Appendix I. Both plates were found to be in residual compression, with Plate 1 having a stress of -105 MPa, and Plate 2 having a stress of -121 MPa.

4.3 Crack Indentation Results

The crack indentation samples were prepared and tested per the procedure listed in Section 3.6. The results for the tests are listed in Table 14.

Table 14: Crack Indentation Results

	Hardness		**Residual Stress (MPa)**	
	As Received	Annealed	As Received	Annealed
Plate 1	1244	1253	-214	-171
Plate 2	1254	1220	-221	-191

There was not a significant change in hardness between the as received and the annealed samples for either plates. Plate 1 experienced a 0.7% increase in hardness, while Plate 2 experienced a 2.7% decrease in hardness. On the other hand, there was a significant decrease in the measured residual stress for both plates. For Plate 1, there was a 20% decrease in the residual stress. Plate 2 had a 13.6% decrease in its measured residual stress.

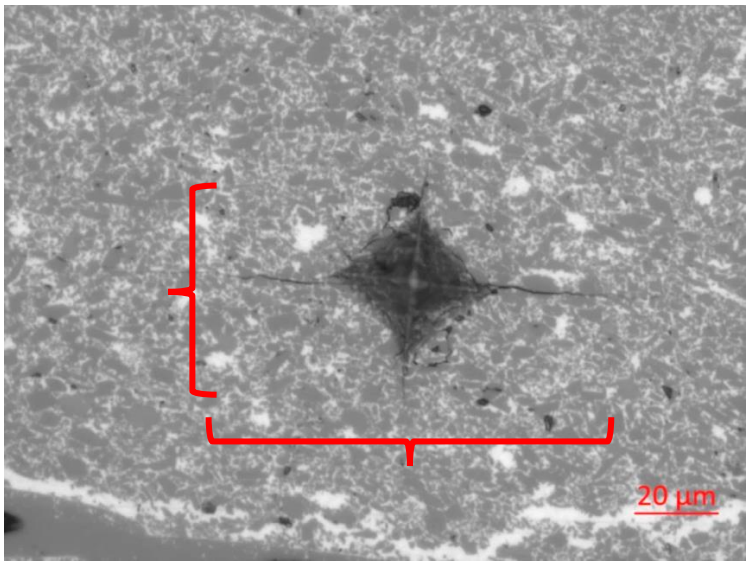

Figure 34: Indentation with Cracks Emanating from Corners

4.4 Mechanical Testing Results

4.4.1 Tension Testing of Plate 1 as-received sample

Using the procedure described for the RHINO testing facility in Section 3.4, mechanical testing of a dogbone specimen from Plate 1 was completed at room temperature. The elastic modulus was found to be 212 GPa and the ultimate failure occurred at 318 MPa. The proportional limit, found using a 0.0005 strain offset method, was 190 MPa. The stress-strain curve for this test can be found in Figure 35.

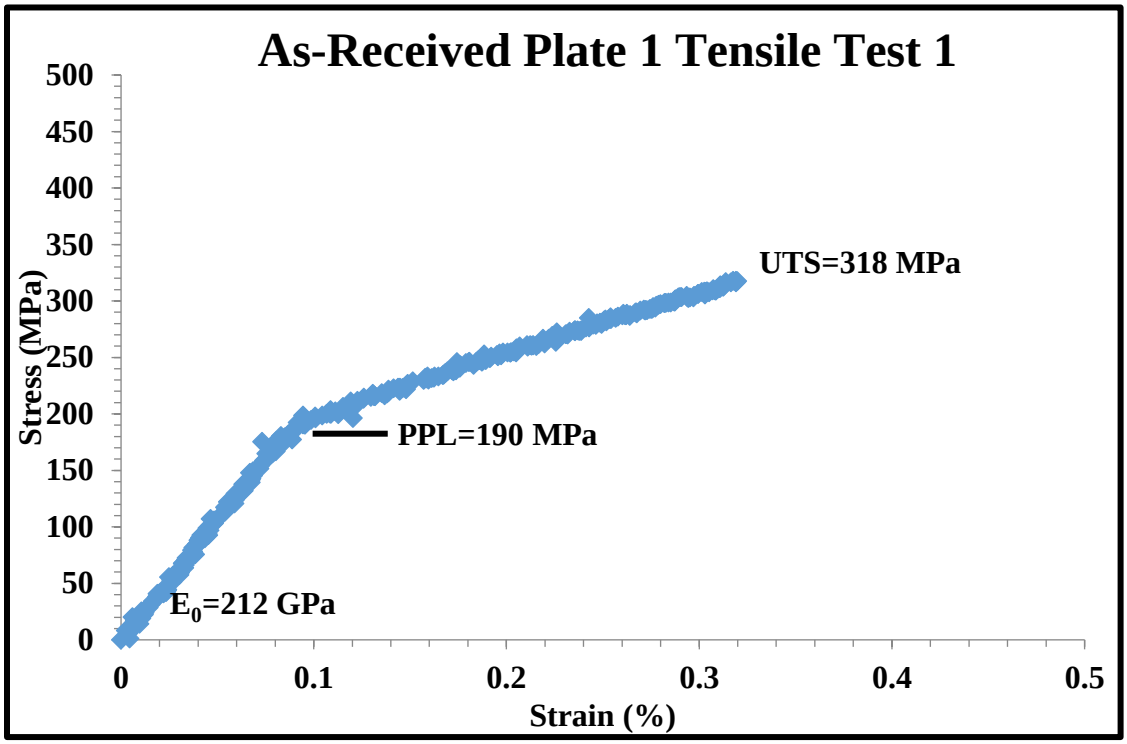

Figure 35: As-Received Plate 1 Tensile Test 1 Stress-Strain Curve at RHINO Lab

During testing, AE and DIC were used to monitor in-situ damage behavior. DIC behavior shows high areas of strain forming along the edges with increasing load, with ultimate failure occurring at one of the strain bands. However, compared to 0/90 laminate composites, there is no strain banding as seen in previous studies [54]. Strain mapping

during testing shows the progressive failure, as seen in Figure 36. The first frame is from early in the test, while the middle image is the frame just before failure, and the last image is the frame just after failure.

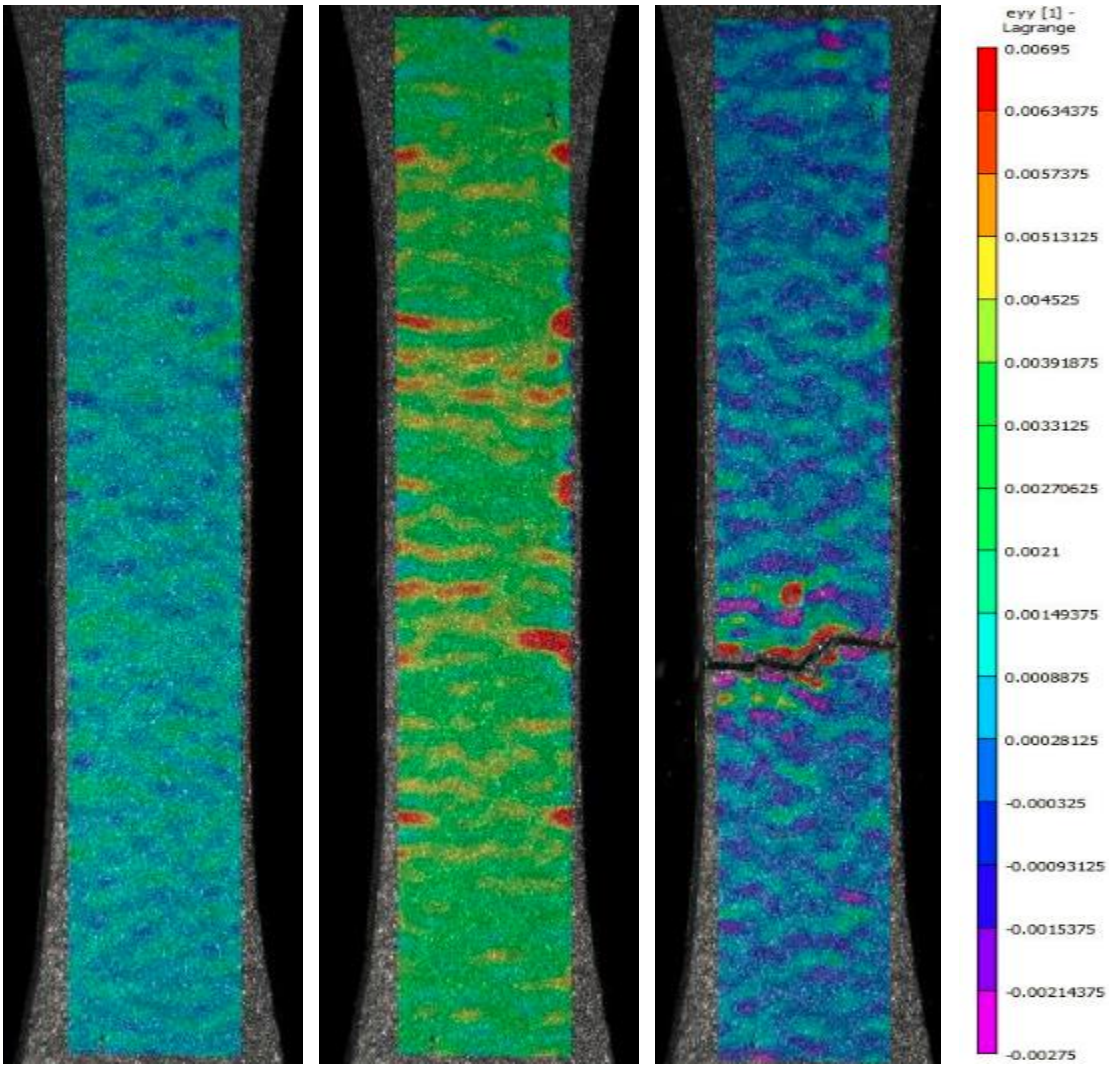

Figure 36: As Received Plate 1 Tensile Test 1 DIC Results

Images of the fracture surface were taken in a SEM. Across the length of the sample, there were areas of substantial fiber pullout. Figure 37 was taken from the center of the sample at a 0° angle, and the top of the image is towards the painted DIC surface.

In order to better image the fiber pullout, the sample was tilted to 30°, as seen in Figure 38. The image is taken from the top of Figure 37, which is boxed in red.

Figure 37: Fracture Surface for Plate 1 As-Received Dogbone Tested at RHINO lab

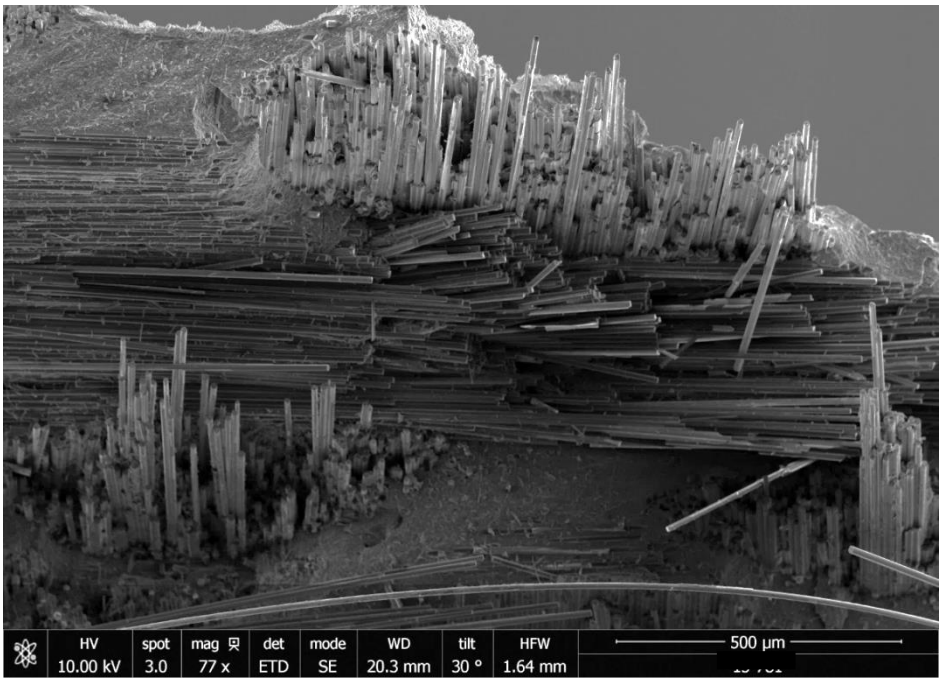

Figure 38: Fiber Pullout for Plate 1 As-Received Dogbone Tested at RHINO lab

Another as-received dogbone specimen from Plate 1 was tested at room temperature at the MMD lab. The elastic modulus was 201 GPa and the ultimate tensile strength was 285 MPa. The proportional limit was found to be 180 MPa. AE events were onset at 173 MPa. The stress-strain curve for this test can be found in Figure 39.

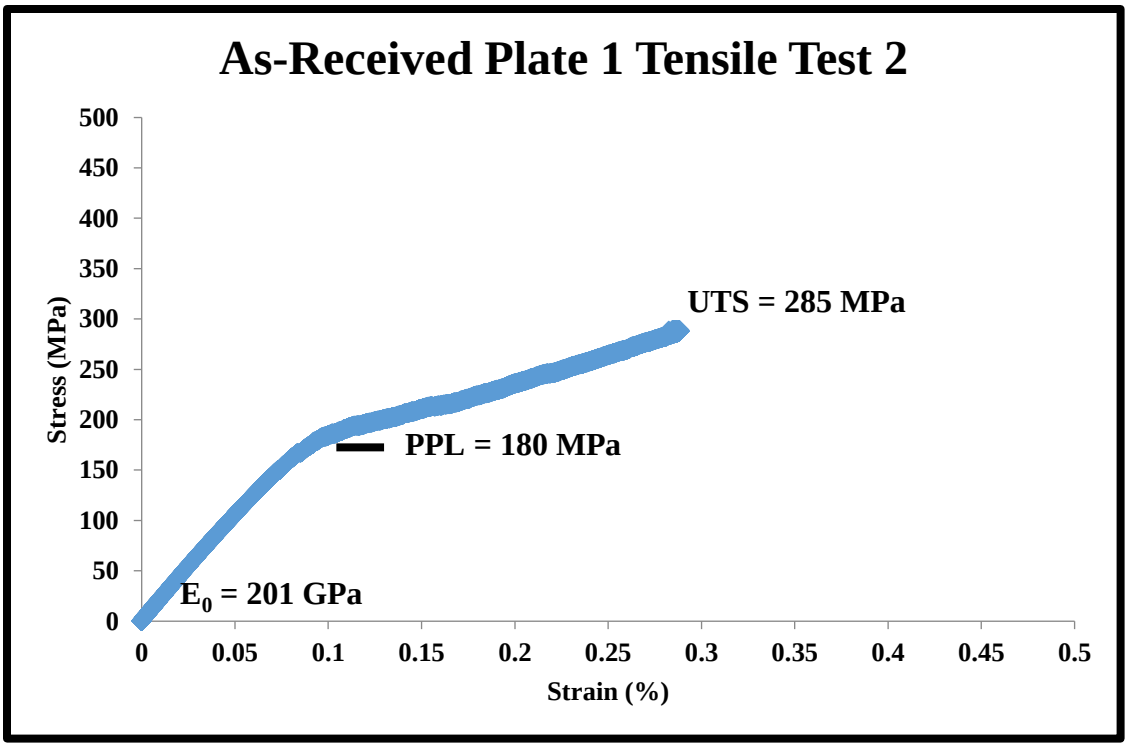

Figure 39: As-Received Plate 1 Tensile Test 2 Stress-Strain Curve at MMD Lab

4.4.2 Tension Testing of Plate 2 as-received sample

As expected, Plate 2 performed with better mechanical properties than Plate 1. The elastic modulus was measured at 192 GPa, and the proportional limit was found to be 220 MPa. The ultimate tensile strength was measured to be 436 MPa. Figure 40 displays the stress-strain curve for Plate 2 at room temperature.

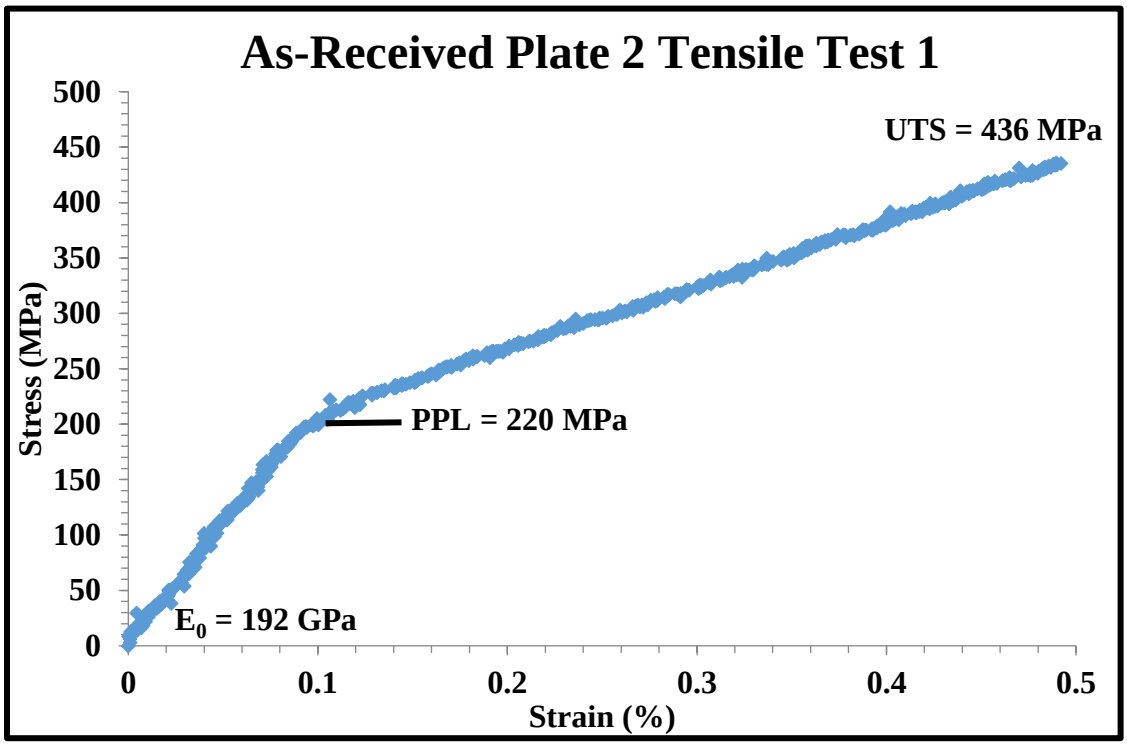

Figure 40: As-Received Plate 2 Tensile Test 1 Stress-Strain Curve at RHINO Lab

DIC strain maps and AE data were also collected during these tests. Similar to Plate 1 at room temperature, Plate 2 showed no strain banding in the DIC results. Once again, the high strain areas were formed on the edges of the gage section. The DIC results for Plate 2 can be seen in Figure 41.

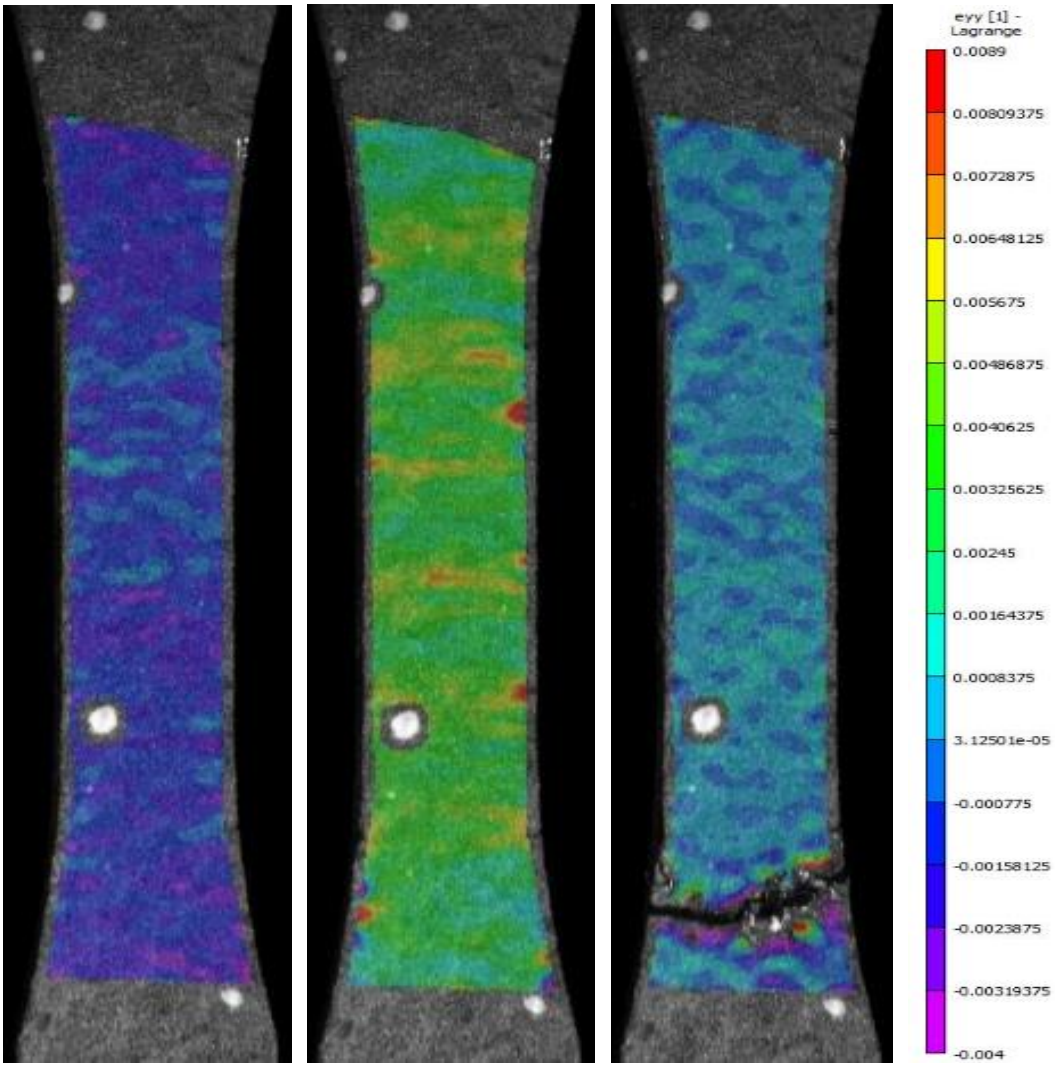

Figure 41: DIC Results for As-Received Plate 2 Tensile Test 1

Images of the fracture surface for the Plate 2 sample were taken with a SEM. The amount of fiber pullout across the sample and length of the pullout was similar to that of Plate 1. An image from the middle of the sample taken at 0° tilt can be seen in Figure 42. Another image displaying the fiber pullout better was taken at 30° tilt, and can be seen in Figure 43.

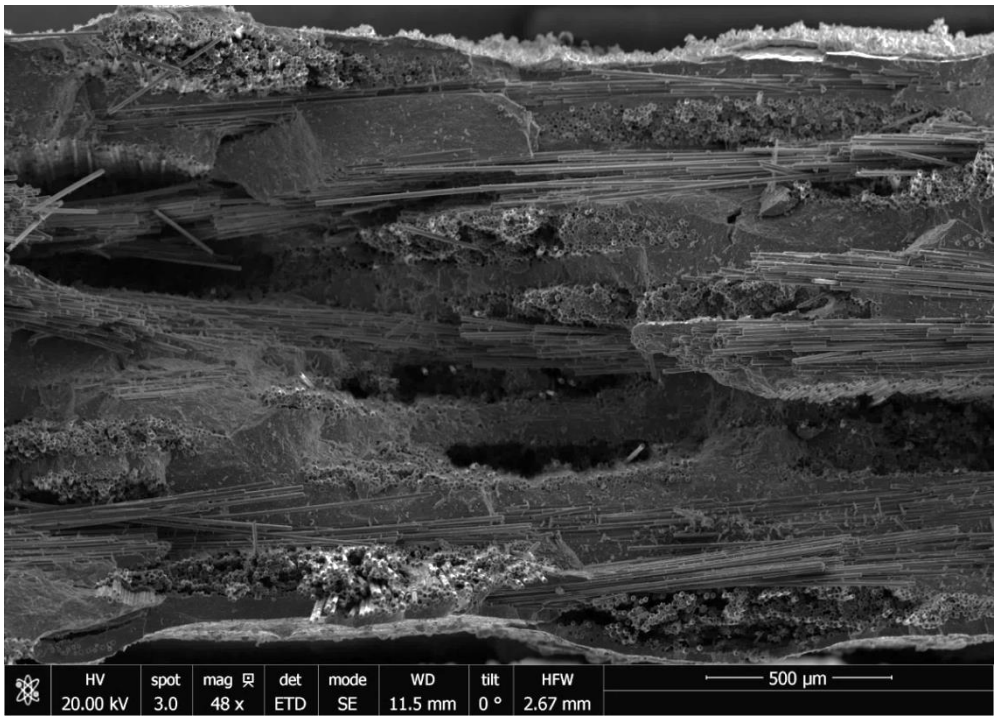

Figure 42: Fracture Surface for Plate 2 As-Received Dogbone Tested at RHINO lab

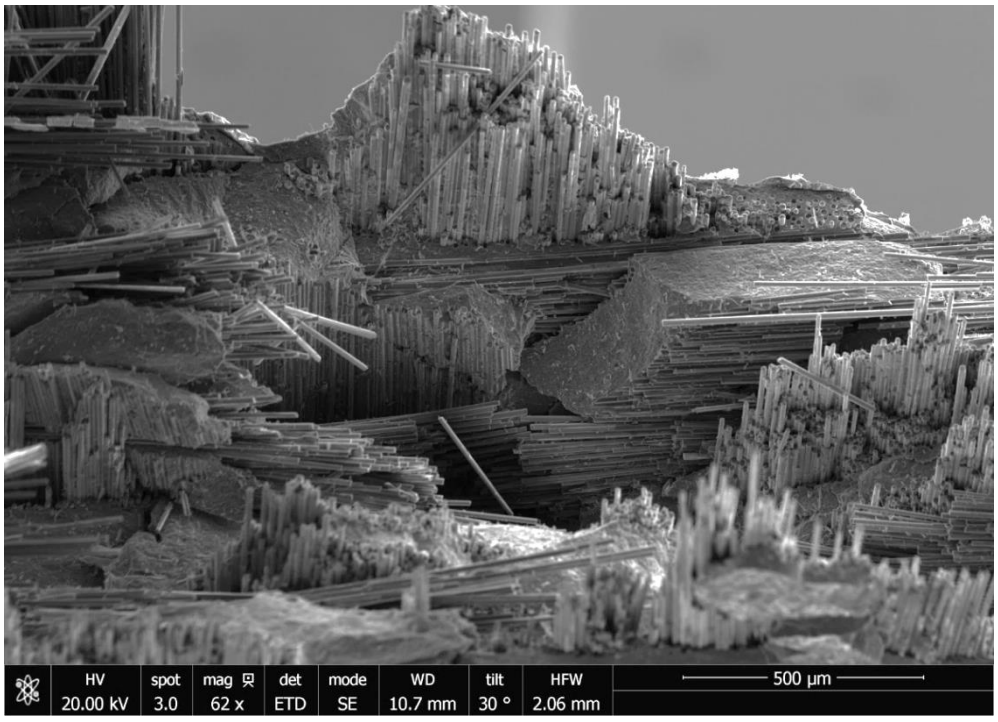

Figure 43: Fiber Pullout for Plate 2 As-Received Dogbone Tested at RHINO lab

Another as-received dogbone specimen from Plate 2 was tested at room temperature at the MMD lab. The elastic modulus was 219 GPa and the ultimate tensile strength was 443 MPa. The proportional limit was found to be 208 MPa. AE events were onset at 193 MPa. The stress-strain curve for this test can be found in Figure 44.

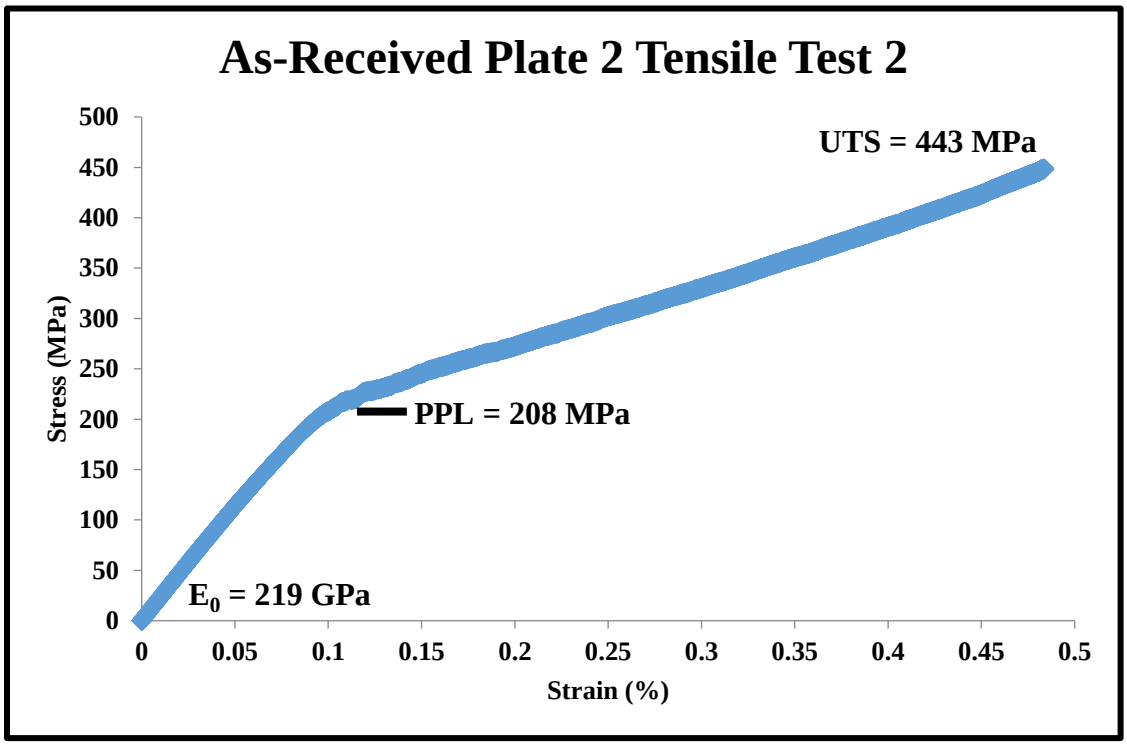

Figure 44: As-Received Plate 2 Tensile Test 2 Stress-Strain Curve at MMD Lab

4.4.3 Tension Testing of Plate 1 Annealed Samples

Two annealed specimens were tested at the MMD lab for Plate 1. The first test is presented in Figure 45. The elastic modulus was 228 GPa and the proportional limit was 178 MPa. However, this test was not completed to failure. AE events were onset at 168 MPa. At 278 MPa, a loud noise was heard, that is typically indicative of the specimen failing. At this point, the load readout on the MTS machine should read a load near zero.

However, for this sample the load readout was at 2000 N. This would usually indicate that the specimen slipped in the grips, but there is uncertainty as a noise associated with failure was heard at the same time. The test was stopped, and the sample was removed to examine any potential failure points. Failure was found within the grip section of the sample. The failure location was cut off, and an equivalent length was cut from the other end. The sample was retested using a lower grip pressure so the fracture surface could be interrogated. However, the mechanical testing data from the re-test is invalid due to the prior testing past the proportional limit of the material.

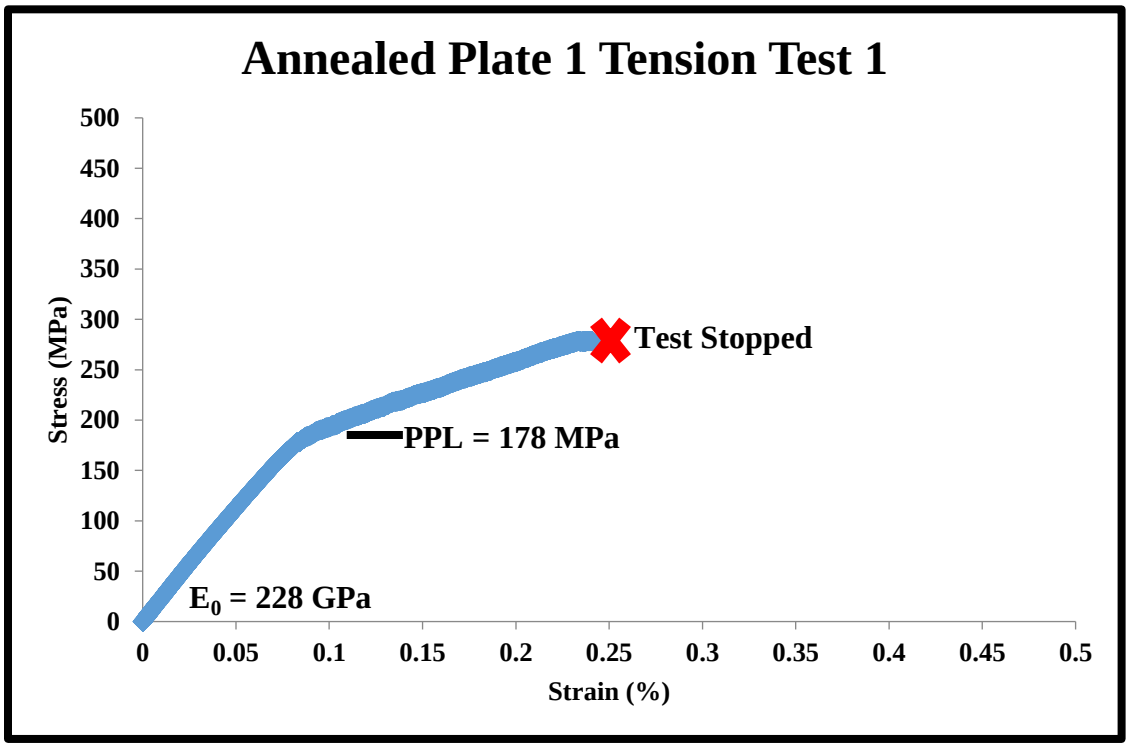

Figure 45: Annealed Plate 1 Tensile Test 1 Stress-Strain Curve at MMD Lab

A second annealed sample from Plate 1 was tested using the lower grip pressure obtained from the re-test of the first annealed specimen. The elastic modulus was 215 GPa, the proportional limit was 175 MPa, and the ultimate tensile strength was 274 MPa. AE events were onset at 156 MPa. The strain to failure was 0.31%. The stress-strain curve can be seen in Figure 46.

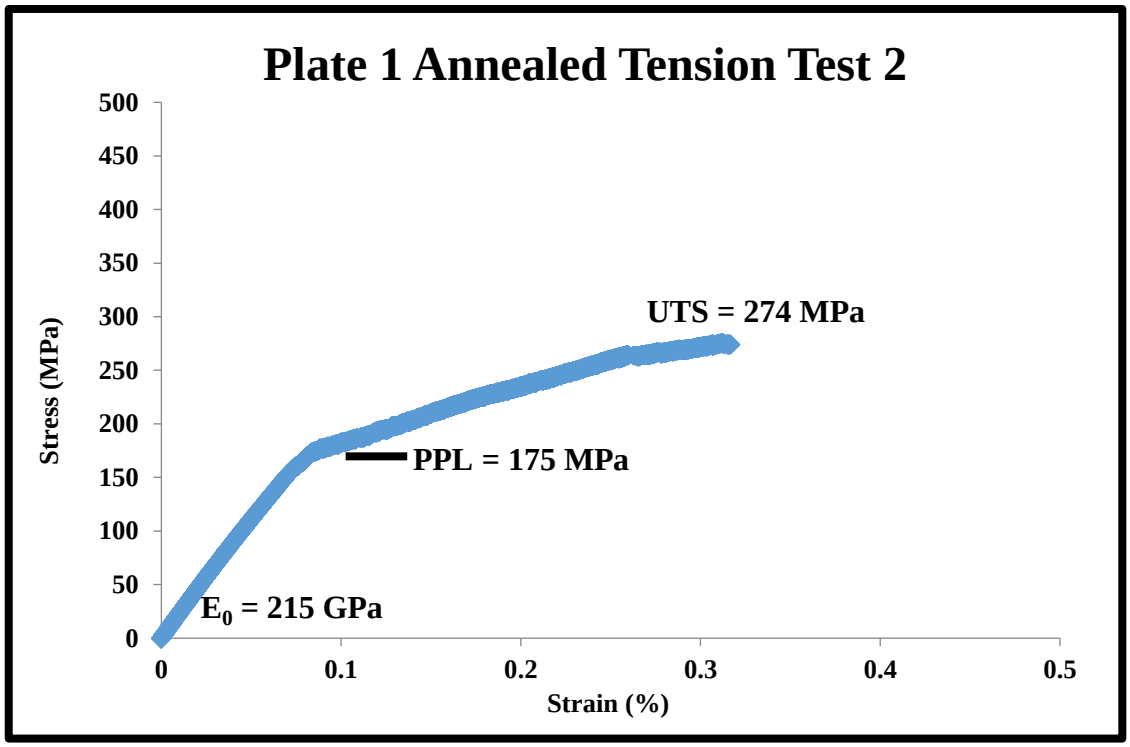

Figure 46: Annealed Plate 1 Tensile Test 2 Stress-Strain Curve at MMD Lab

Images of the fracture surface for the second sample from Plate 1 were taken with a SEM. An image from the middle of the sample taken at 0° tilt can be seen in Figure 47. Another image displaying the fiber pullout better was taken at 30° tilt, and can be seen in Figure 48. The fracture surface is less torturous than the as-received specimens, and had shorter fiber pullout.

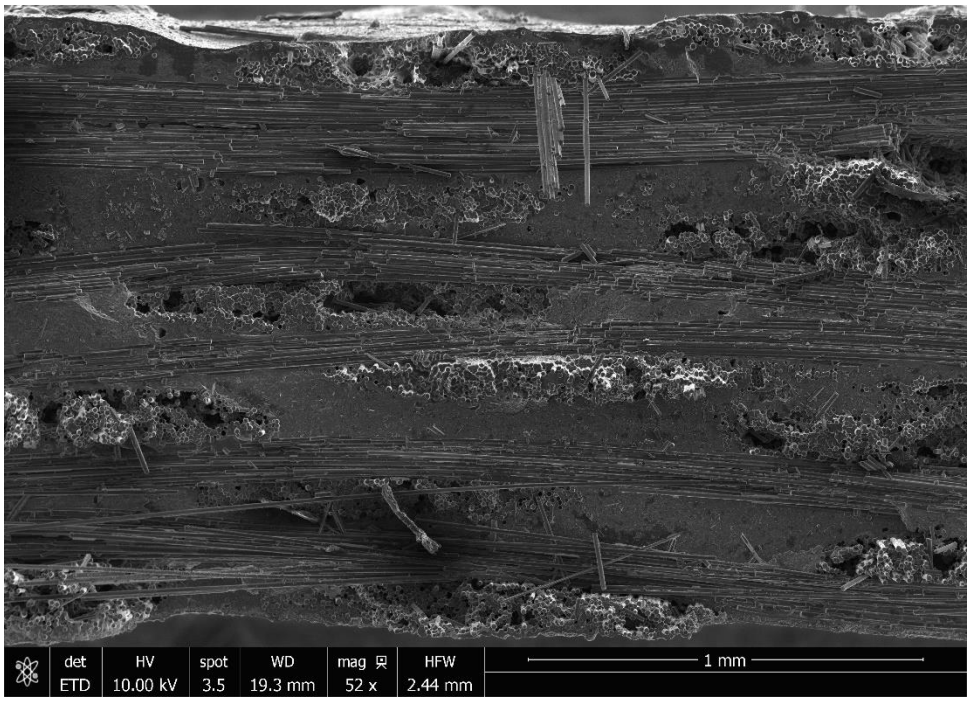

Figure 47: Fracture Surface for Plate 1 Annealed Dogbone Tested at MMD lab

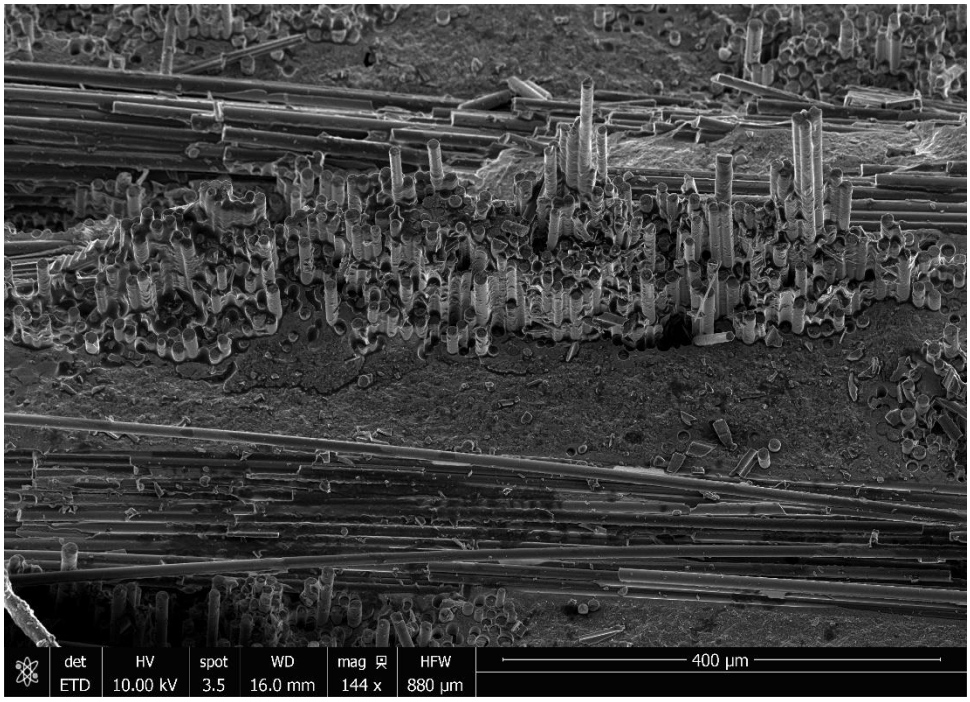

Figure 48: Fiber Pullout for Plate 1 Annealed Dogbone Tested at MMD lab

4.4.4 Tension Testing of Plate 2 Annealed Samples

Two annealed samples from Plate 2 were tested at the MMD lab. The first sample had an elastic modulus of 209 GPa. The proportional limit was 182 MPa, and the ultimate tensile strength was 350 MPa. The sample also had an ultimate strain of 0.37%. AE events were onset at 182 MPa. The stress-strain curve can be seen in Figure 49.

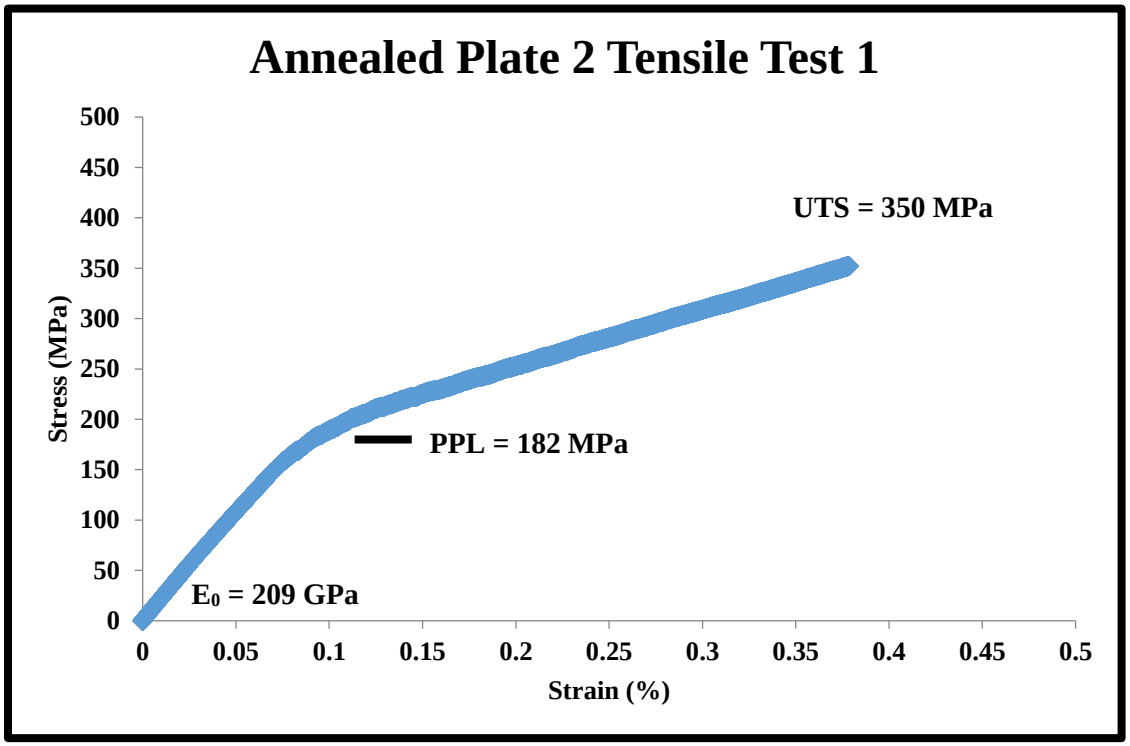

Figure 49: Annealed Plate 2 Tensile Test 1 Stress-Strain Curve at MMD Lab

The second annealed sample from Plate 2 behaved similarly. The elastic modulus was 222 GPa, the proportional limit was 189 MPa, and the ultimate tensile strength was 361 MPa. The ultimate strain was also 0.37%. AE events were onset at 176 MPa. The stress-strain curve can be seen in Figure 50.

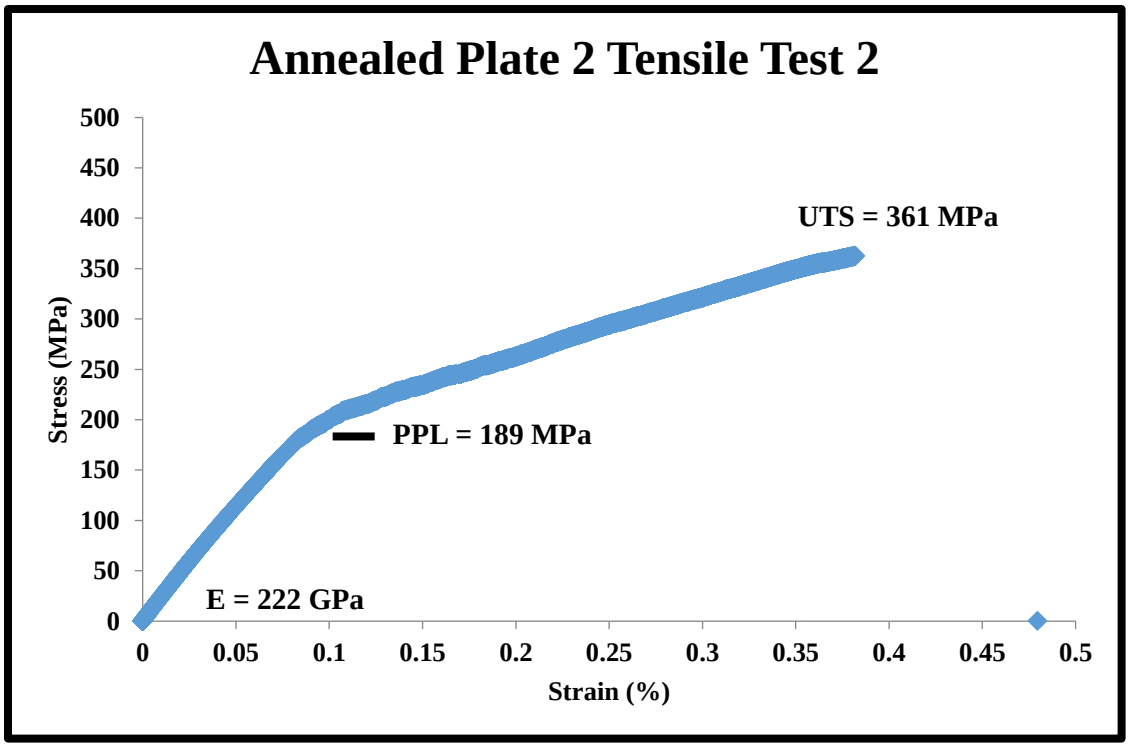

Figure 50: Annealed Plate 2 Tensile Test 2 Stress-Strain Curve at MMD Lab

A SEM was used to take images of the fracture surface from the second annealed sample from Plate 2. An image from the middle of the sample taken at 0° tilt can be seen in Figure 51. Figure 52 shows an image taken at 30° to display the fiber pullout.

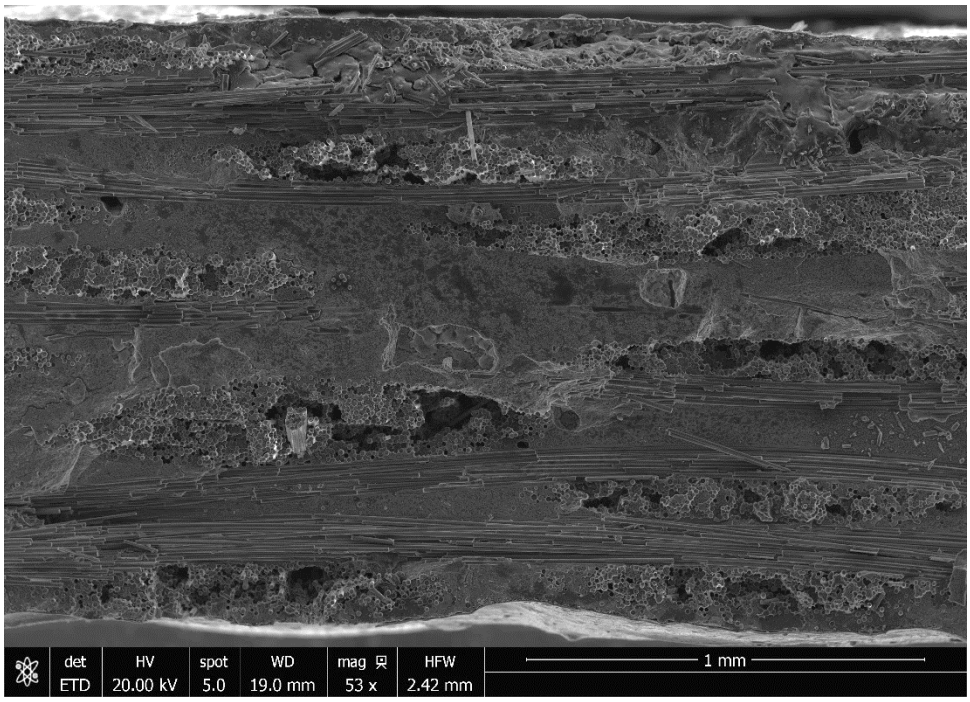

Figure 51: Fracture Surface for Plate 2 Annealed Dogbone Tested at MMD lab

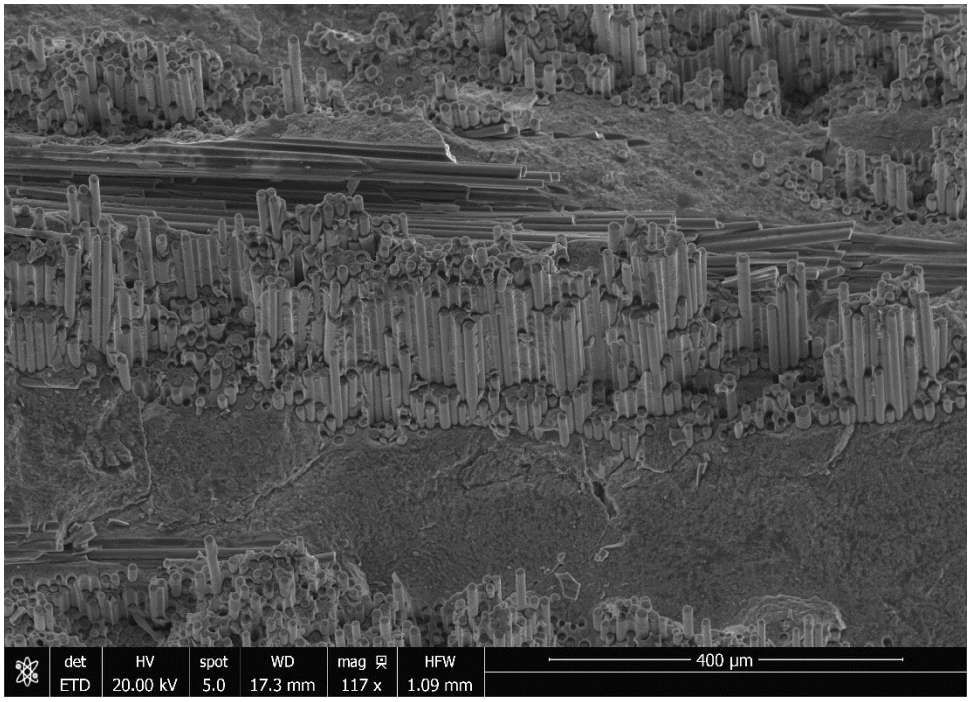

Figure 52: Fiber Pullout for Plate 2 Annealed Dogbone Tested at MMD lab

4.5 Tension Testing Summary

Table 15 provides a summary of the mechanical testing presented in Section 4.4. The elastic moduli, ultimate tensile strengths, proportional limits and ultimate strains are averages between two samples, except for the Annealed Plate 1. For the Plate 1 annealed specimens, the elastic modulus, and proportional limits are averaged between the two tests, but the ultimate tensile strength and ultimate strain are only based off Tensile Test 2. The AE events reported are only from the tests conducted at the MMD lab, resulting in the as-received data being based off of one test and the annealed AE data being averaged between two specimens.

Table 15: Summary of Mechanical Testing Data

	Condition	Elastic Modulus (GPa)	Ultimate Tensile Strength (MPa)	Proportional Limit (MPa)	Ultimate Strain (%)	AE onset (MPa)
Plate 1	as-received	207	302	185	.30	173
	annealed	222	274	177	.31	162
Plate 2	as-received	206	440	214	.49	193
	annealed	216	356	186	.37	179

As seen in Table 15, the elastic modulus of both plates slightly increased with heat treatment, with Plate 1 increasing from 207 GPa to 222 GPa, and Plate 2 increasing from 206 GPa to 216 GPa. However, these small increases are well within the expected variability of the material. The ultimate tensile strength of both plates decreased with heat treatment, where Plate 1 decreased by 28 MPa and Plate 2 decreasing by 84 MPa.

For Plate 1, the decrease in ultimate tensile strength could certainly be within the variability of the material, but Plate 2's decrease is likely not within the variability. The proportional limits decreased by 8 MPa and 28 MPa for Plate 1 and Plate 2, respectively, which is also within the ceramic variability of the material. In Plate 1, the ultimate strain did not change, while it decreased by .12% for Plate 2. The AE onset stress decreased by 11 MPa for Plate 1 and by 14 MPa for Plate 2, once again being within the variability of the material.

4.5 As-Received Raman Spectroscopy Results

4.5.1 Virgin and In-Composite Fibers

A study was completed on virgin Sylramic and Sylramic-iBN fibers and fibers that were present within the composite. It was seen in both cases that there is excess carbon present in the fibers. Figure 53 displays a Raman map showing the excess carbon within the in-composite fibers.

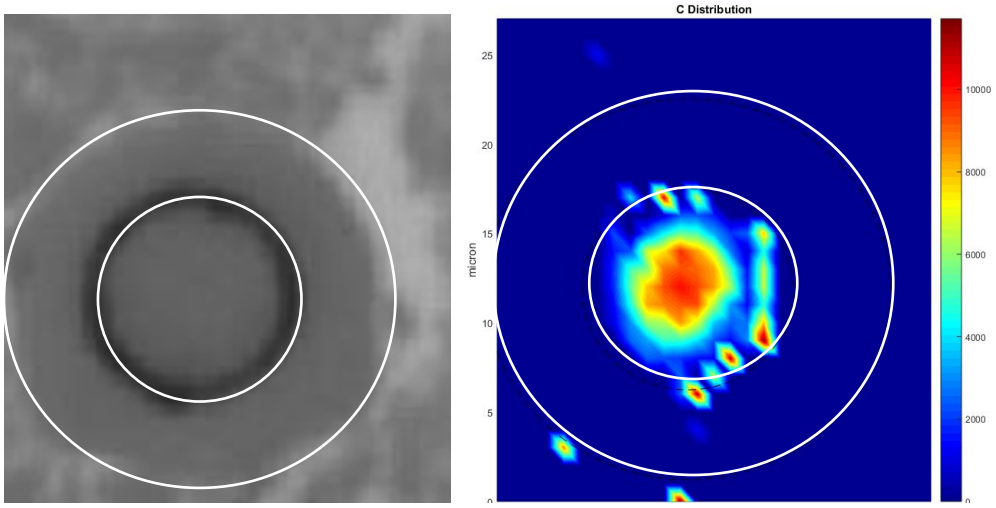

Figure 53: Excess Carbon Present in In-Composite Fiber

4.5.2 Powder Study

Fano resonance in the silicon caused a shift in the unstressed wavenumber. To find the unstressed wavenumber, a sample was taken from Plate 1 and ground into a powder using a mortar and pestle. After conducting Raman scans using the same parameters as the composite studies, on the powder, it was found that the Fano effect caused the standard peak center of silicon to shift from 520.5 to 515.3. The new value was used to more accurately calculate the stresses in silicon.

4.5.3 As-received composite stress data

Figures 54 & 55 depict typical micro-Raman spectroscopy maps for chemical composition as well as residual stress distribution away from the fiber interface for both silicon and silicon carbide in Plates 1 and 2, respectively. The maps show that Plate 1 has a much higher fraction of unreacted Si, a slightly lower residual stress in SiC, and similar stress in Si compared to their counterparts in Plate 2.

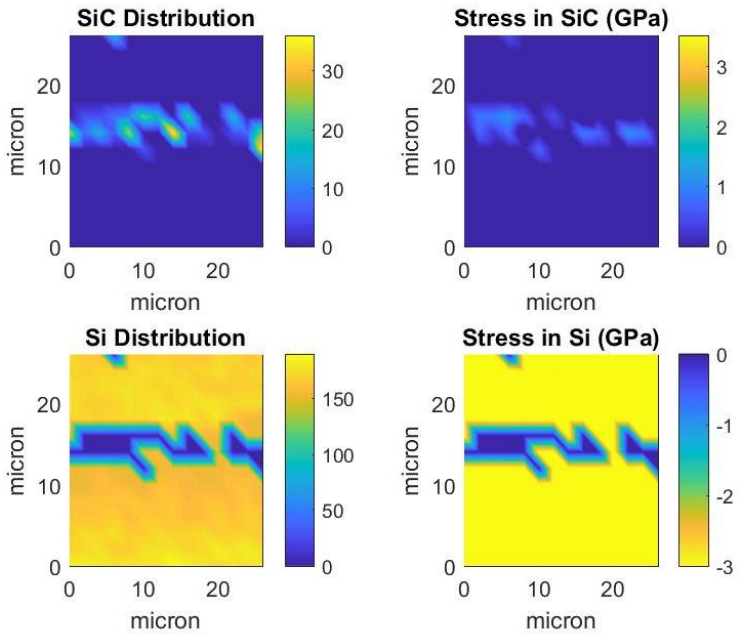

Figure 54: Silicon and SiC distribution and residual stress maps within the matrix away from fibers in Plate 1

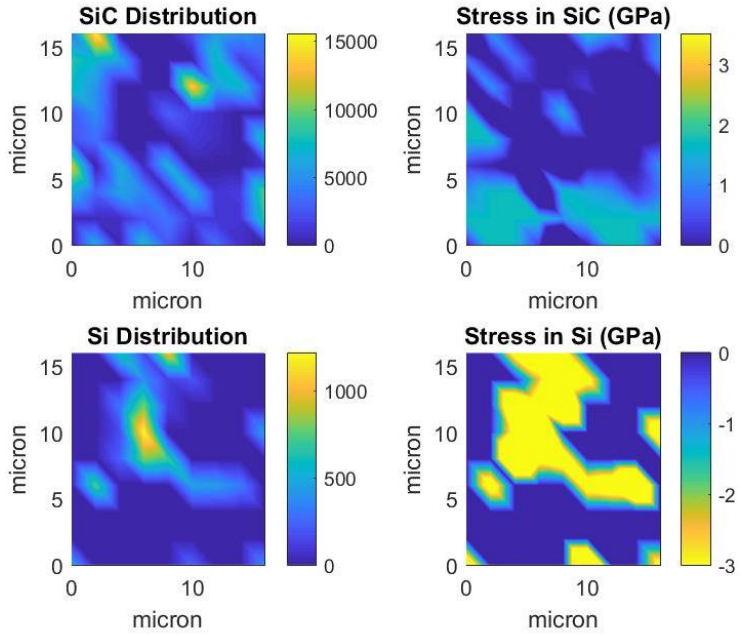

Figure 55: Silicon and SiC distribution and residual stress maps within the matrix away from fibers in Plate 2

Figure 56 depicts the Raman mapping results for both SiC and Si distribution and their residual stress around Sylramic fiber in Plate 1. As mentioned, when using Raman spectroscopy to measure stress, the stated residual stress values are the average of the trace of the stress tensor. Figure 57 shows the same measured maps around the Sylramic-iBN fiber in Plate 2. The Raman maps show that Plate 2 has higher residual tensile stress in the fiber and higher residual stress in the SiC than Plate 1. Also, Plate 1 has much higher unreacted silicon content, with similar residual compressive stress in the silicon as Plate 2. As seen in Table 16, for Plate 1, the residual stress in fiber reaches a maximum of +1.87 GPa, +2.58 GPa in the SiC CVI coating, and +3.05 GPa in the SiC matrix. In the silicon, however, the residual stress maximum is around -2.97 GPa. In Plate 2, the maximum residual stress in the fiber reaches +1.81 GPa, +2.72 GPa in the SiC CVI coating, and +3.02 GPa in the SiC matrix. In Si, the residual stress is found to at a maximum of -2.99 GPa.

Table 16: Raman stress measurements for Plate 1 and Plate 2 as-received composites

	SiC Fiber Average Stress (GPa)	SiC Fiber Maximum Stress (GPa)	SiC CVI Coating Average Stress (GPa)	SiC CVI Coating Maximum Stress (GPa)	SiC Matrix Average Stress (GPa)	SiC Matrix Maximum Stress (GPa)	Free Silicon Average Stress (GPa)	Free Silicon Maximum Stress (GPa)
Plate 1	.50 ± .11	1.87	.93 ± .05	2.58	1.46 ± .08	3.05	-2.04 ± .07	-2.97
Plate 2	.69 ± .10	1.81	1.24 ± .07	2.72	1.45 ± .05	3.02	-1.96 ± .04	-2.99

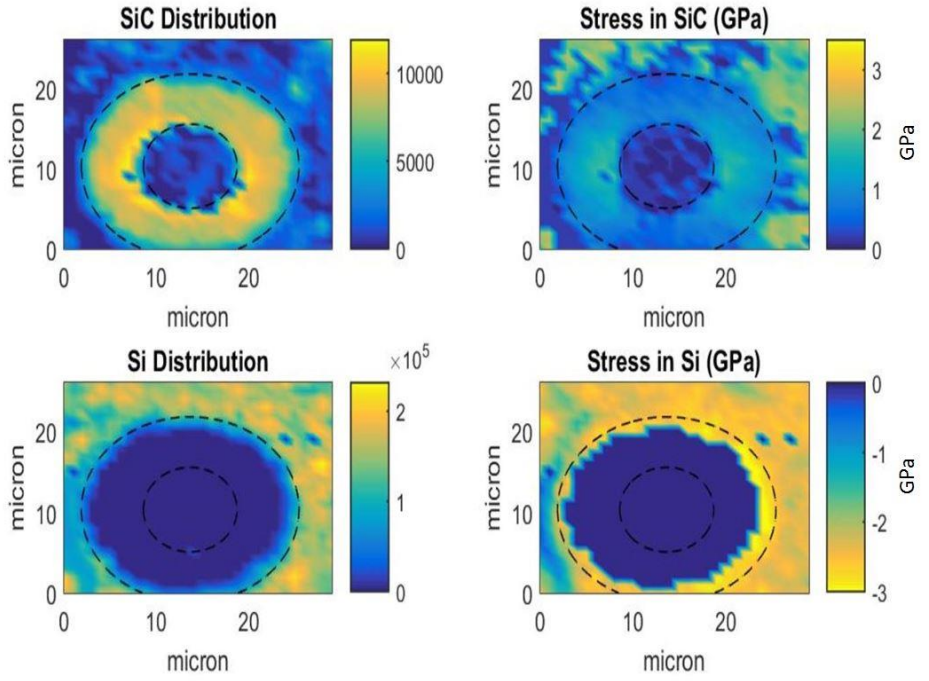

Figure 56: SiC and unreacted Si distributions as well as residual stresses around the Sylramic fibers in Plate 1

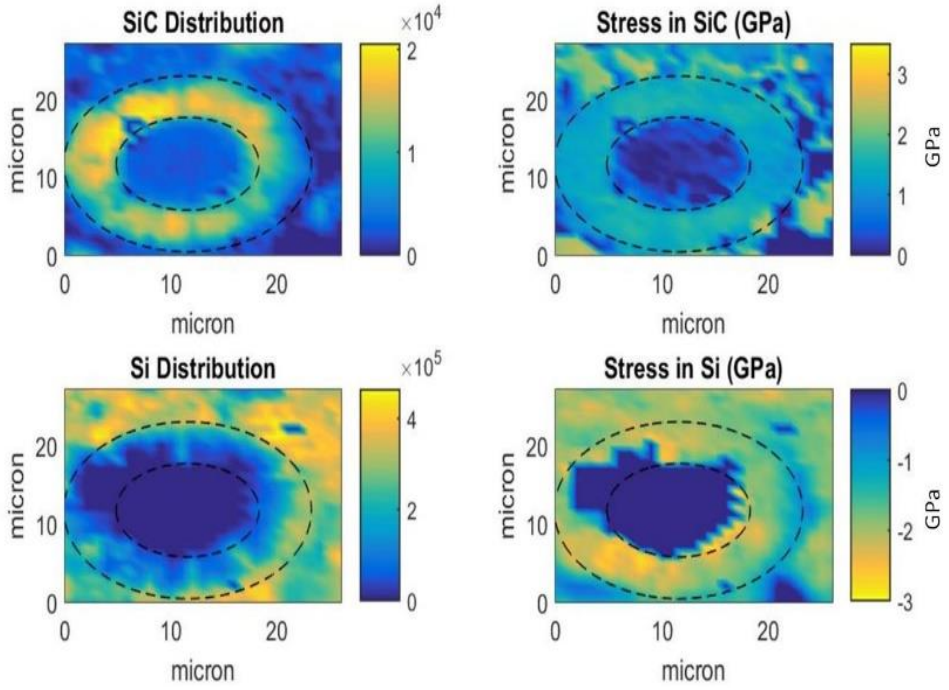

Figure 57: SiC and unreacted Si distributions and residual stress maps around the Sylramic-iBN fibers in Plate 2

4.6 Theoretical Micro-Residual Stress Calculations

4.6.1 Micro-Residual Stresses in the matrix due to silicon solidification expansion

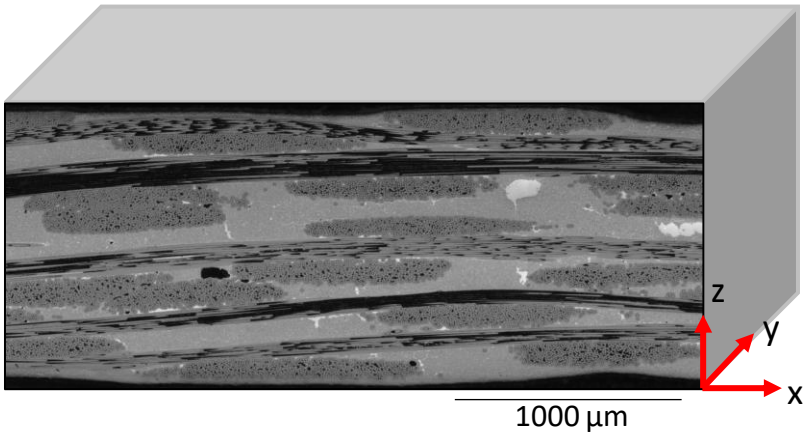

Figure 58: A schematic of the Cartesian axes system used in this stress analysis

Figure 58 depicts an optical micrograph and a schematic representing the SiC/SiC CMC investigated and the Cartesian axes system considered in the discussion and theoretical calculation of the expected residual stresses. The volume expansion of silicon can be estimated according to Equation 9 as [61, 68]:

$$\frac{\Delta V}{V_o} = \frac{\rho_{1410^\circ C} - \rho_{RT}}{\rho_{RT}}$$

Equation 9

where ΔV is the change in volume from liquid to solid, V_o is the volume at room temperature, and ρ represents the densities at 1410° C and at room temperature. Substituting for the density values of liquid silicon at the melting point, 2.55 g/cm^3, and

in the solid state at room temperature, 2.33 g/cm^3, leads to a volumetric expansion of 9.4% upon cooldown.

Realizing that the expanding silicon is surrounded by a matrix of SiC, the final increase in the silicon volume must equal the shrinkage in SiC volume within the affected zone, as seen in Equation 10:

$$0.094 = \frac{V_{SiC}}{V_{Si}}\left[\frac{P}{k_{SiC}}\right] + \frac{P}{k_{Si}}$$

Equation 10

Where, *e* is volumetric strain, *k* is the bulk modulus, *V* is the volume, and P is the maximum measured silicon stress, obtained to be 3 GPa from Raman spectroscopy. It is important to note that the value of such stress will depend on the volume of the affected zone compared to the volume of the silicon pools. Specifically, the larger the ration of the SiC volume over the silicon volume, or V_{SiC}/V_{Si}, the lower the developed internal pressure.

Shown in Figure 59a, the fiber and surrounding matrix material can be modeled as concentric spheres. The Si bulk modulus, k_{Si}, is estimated to be 73.2 GPa (0.75 of the room temperature value of 97.6 GPa) [56-59] near 1400 ºC and the SiC bulk modulus is 235 GPa [69]. Substituting these values into Equation 11 yields a value for $V_{SiC}/V_{Si} = 4.14$.

(a) **(b)**

Figure 59: Schematics showing the geometry used to model residual stresses around a) an unreacted silicon pool embedded in the SiC matrix away from the fiber, and b) an unreacted silicon pool next to a fiber.

The silicon spherical pool will be under hydrostatic pressure with a stress tensor in the form of Equation 11. This stress tensor uses the maximum stress measured in the silicon from Raman spectroscopy.

$$\sigma_{Si} = \begin{vmatrix} -3.0 & 0 & 0 \\ 0 & -3.0 & 0 \\ 0 & 0 & -3.0 \end{vmatrix} GPa$$

Equation 11

In this case, for $V_{SiC}/V_{Si} = 4.14$, the outer diameter (d_o) of the affected spherical zone must be 3.45 the internal diameter (d_i). Using Equation 12 [70], the radial stresses for SiC can be calculated at the interface using the elastic theory treatment of thick-walled spherical pressure vessel equation with an internal pressure (p_i).

$$\sigma_{rr} = p_i \left[\frac{(d_0^2 + d_i^2)}{(d_0^2 - d_i^2)}\right]$$

Equation 12

With the calculated radial stresses, the stress tensor at the Si/SiC interface will be:

$$\sigma_{SiC} = \begin{vmatrix} -3.0 & 0 & 0 \\ 0 & +3.54 & 0 \\ 0 & 0 & +3.54 \end{vmatrix} GPa$$

Equation 13

Another source of residual stresses in the matrix is thermal residual stresses (TRS) due to the mismatch in the coefficients of thermal expansion (CTEs) between the silicon and silicon carbide. Using the CTE values listed in Table 13 and calculating the TRS in both silicon and silicon carbide resulted in small values in the range of 0.03 GPa. Such values are negligible compared to the stress values resulted from the silicon expansion upon solidification. Realizing the Raman measurements under such stress state would yield a value representing the average of the tensor trace [71-74], it is realized that the average measurements of -2.0 GPa in the free silicon in the matrix are near the theoretical calculations of -2.11 GPa, confirming that the affected zone around the unreacted silicon has a diameter that extends to 3.45 times that of the silicon pool size.

4.6.2 Residual stresses around the fibers

In addition to stresses resulting from silicon solidification around the Sylramic and Sylramic-iBN fibers, the large difference in CTE of the composite constituents will also contribute to the developed residual stresses in processed composite.

In this case, the composite was modeled as 4 concentric cylinders as shown in Figure 59b. Knowing that the fiber diameter is 10 μm, the thickness of the CVI-SiC coating around the fibers was measured experimentally using high resolution optical microscopy and was found to be 4.4 μm. The silicon cylinder thickness was determined

from the Raman composition map and is estimated to be 3 μm. The area of the SiC matrix in the model was determined by the V_{SiC}/V_{Si} ratio of 4.14.

Assuming a perfect interfacial adhesion between all cylinders, equilibrium conditions due to 0.03 axial expansion of the silicon upon solidification can be expressed as Equation 14:

$$0.03 - \frac{P_{Si}}{A_{Si}E_{Si}} = \frac{P_f}{A_f E_f} = \frac{P_{cvi}}{A_{CVI}E_{CVI}} = \frac{P_{SiC}}{A_{SiC}E_{SiC}}$$

Equation 14

Also, the force equilibrium condition in the fiber axial direction necessitates that Equation 15 be true:

$$-P_{Si} = P_f + P_{CVI} + P_{SiC}$$

Equation 15

To account for the thermal residual stresses developing upon cooling the composite from 1410ºC to room temperature, considered to be 25ºC, equilibrium conditions can be expressed as Equation 16:

$$\alpha_f \Delta T - \frac{P_f}{A_f E_f} = \alpha_{CVI}\Delta T - \frac{P_{CVI}}{A_{CVI}E_{CVI}} = \alpha_{Si}\Delta T - \frac{P_{Si}}{A_{Si}E_{Si}} = \alpha_{SiC}\Delta T - \frac{P_{SiC}}{A_{SiC}E_{SiC}}$$

Equation 16

And the forces equilibrium condition necessitates that:

$$P_f = -P_{Si} + P_{CVI} + P_{SiC}$$

Equation 17

By solving these equations, the axial stresses due to silicon expansion can be calculated. These stresses, the residual thermal stresses and the total approximated residual stresses are presented and compared to the measured stresses in Table 17.

Table 17: Approximated and measured residual stresses in as-received composite

	Fiber Stress (GPa)	Silicon Stress (GPa)	SiC CVI Stress (GPa)	SiC Matrix Stress (GPa)
Silicon Expansion	+.342	-1.348	+.358	+.647
Thermal Residual Stresses	+.665	-0.057	+.216	+.3918
Total Approximation	+1.007	-1.405	+.574	+1.0388
Measured: Plate 1	+.50	-2.04	+.93	+1.46
Measured: Plate 2	+.69	-1.96	+1.24	+1.45

4.7 Cyclic Annealed Raman Spectroscopy Results

4.7.1 Plate 1 Annealing Cycle at 1150º C

The 1150º C annealing cycle results for SiC in the matrix material, SiC in the CVI coating, and the SiC fiber can be seen in Figures 60 through 62. The results for free silicon in the matrix and silicon contained within the CVI coating can be seen in Figures 63 through 64. The error bars on all graphs represent 95% confidence intervals. Dashed lines are to guide the eye.

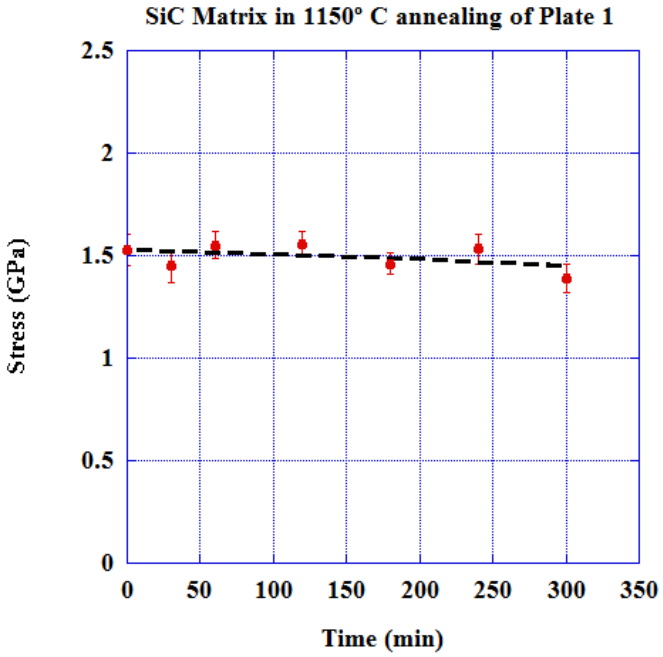

Figure 60: SiC Matrix Residual Stress vs. Time for Plate 1 at 1150° C

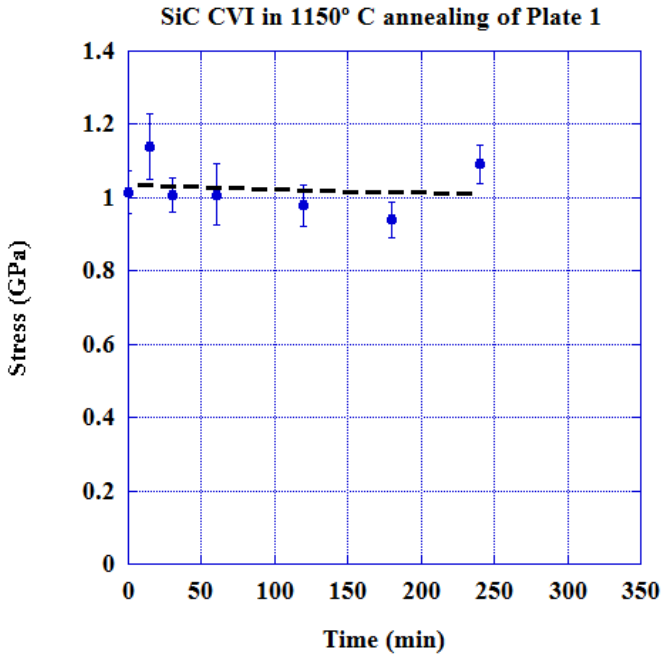

Figure 61: SiC CVI Residual Stress vs. Time for Plate 1 at 1150° C

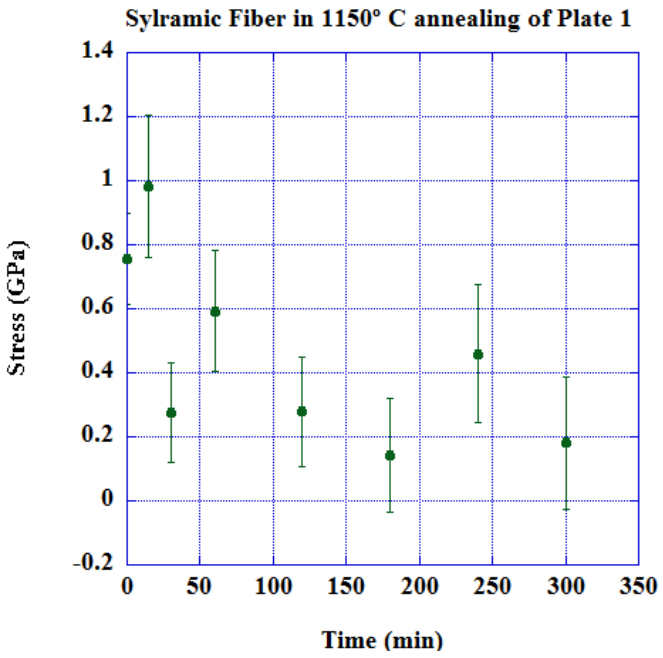

Figure 62: Sylramic Fiber Residual Stress vs. Time for Plate 1 at 1150° C

From Figure 60, it is seen that there is no major change in the residual stresses within the SiC MI matrix throughout the annealing process. The residual stress is nearly constant at 1.5 GPa in tension. The CVI SiC residual stress is also nearly constant at 1 GPa in tension, as seen in Figure 61. However, unlike the other SiC constituents, the Sylramic fiber's residual stresses decrease from around 0.9 GPa to 0.2 GPa with the heat treatment. All of the fibers are curve fit in Figure 80.

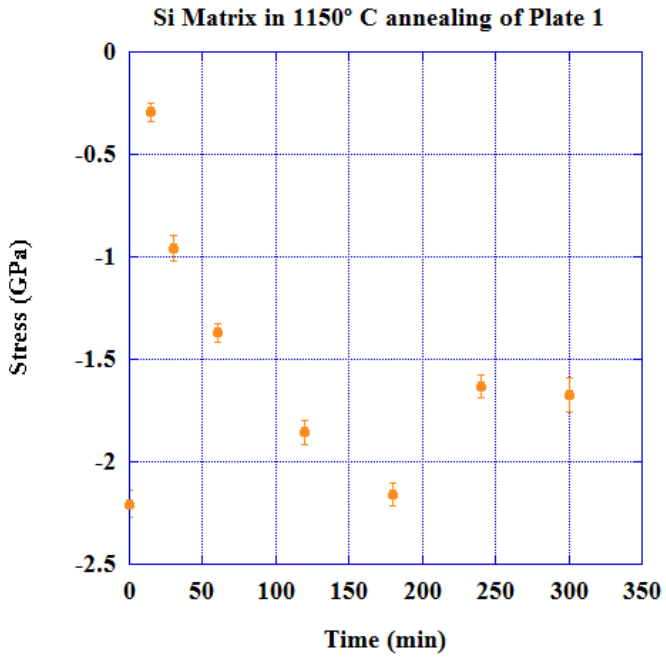

Figure 63: Si Matrix Residual Stress vs. Time for Plate 1 at 1150° C

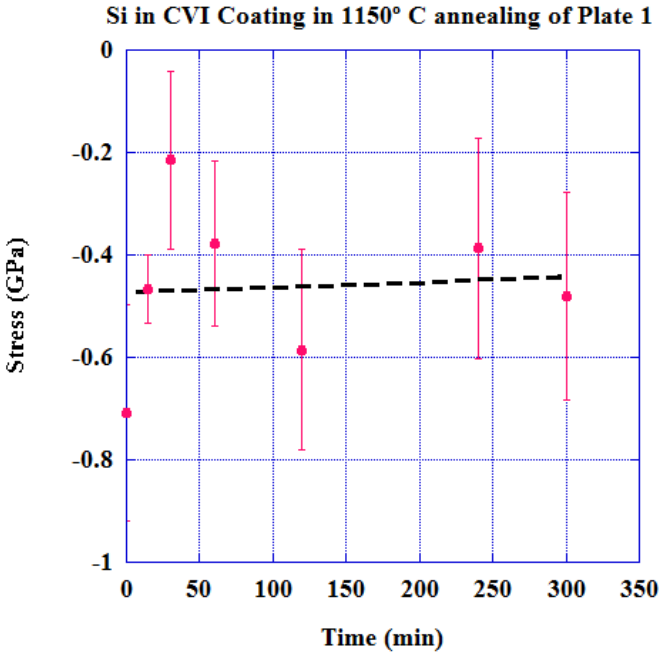

Figure 64: Si in CVI Residual Stress vs. Time for Plate 1 at 1150° C

As seen in Figure 63, the silicon within the matrix behaves unexpectedly, with an initial decrease in the compressive residual stress, and then increases, leveling out around -1.7 GPa. The silicon within the CVI coating stayed nearly constant near -0.5 GPa.

4.7.2 Plate 2 Annealing Cycle at 1150º C

The results for the SiC constituents in Plate 2 annealed at 1150º C can be seen in Figures 65 through 67. The silicon results can be seen in Figures 68 and 69. Error bars on all charts represent a 95% confidence interval for the respective data. Dashed lines are to guide the eye.

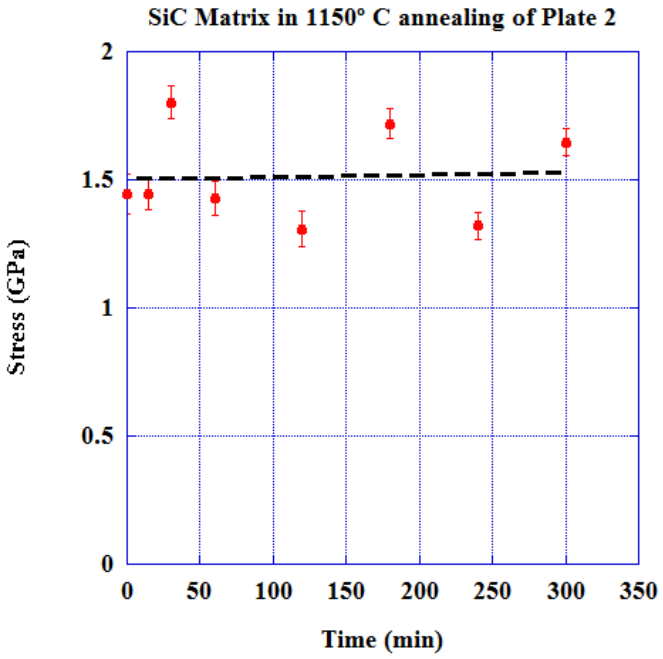

Figure 65: SiC Matrix Residual Stress vs. Time for Plate 2 at 1150° C

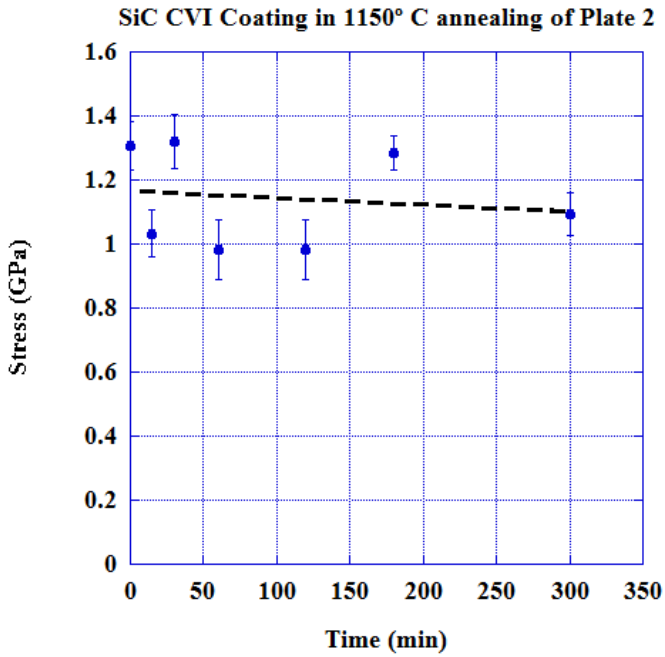

Figure 66: SiC CVI Residual Stress vs. Time for Plate 2 at 1150° C

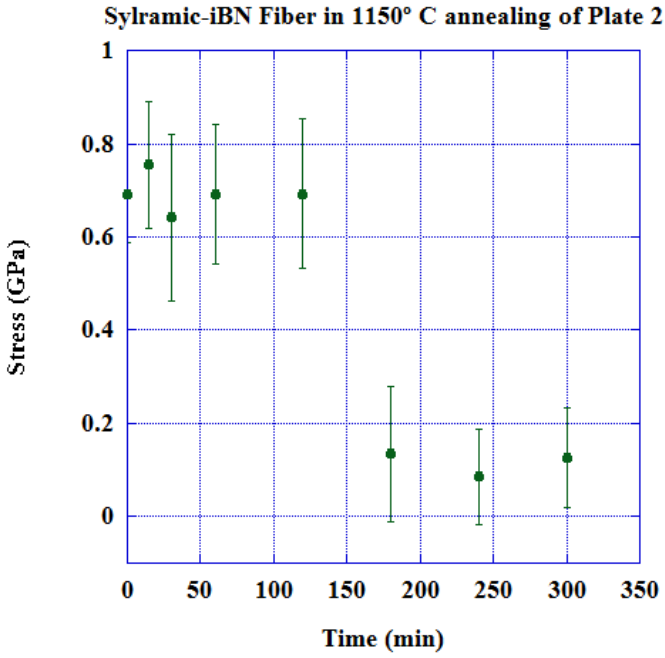

Figure 67: Sylramic-iBN Fiber Residual Stress vs. Time for Plate 2 at 1150° C

As seen in Figure 65, the residual stresses within the MI SiC particulates stay nearly constant at 1.5 GPa in tension. The SiC CVI stresses also stay fairly constant at 1.1 GPa in tension. The Sylramic-iBN fiber stresses decrease from 0.7 GPa to 0.1 GPa in tension, seen in Figure 67. The exponential decay fit for the fiber can be found in Figure 80.

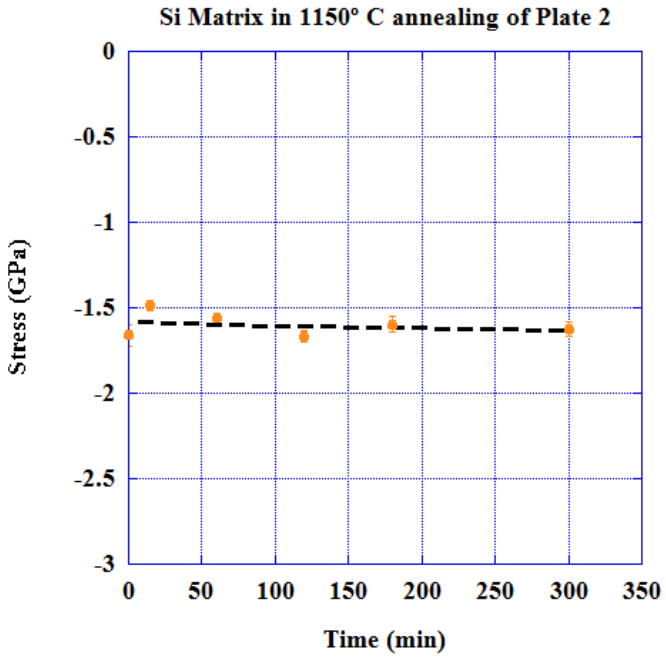

Figure 68: Si Matrix Residual Stress vs. Time for Plate 2 at 1150° C

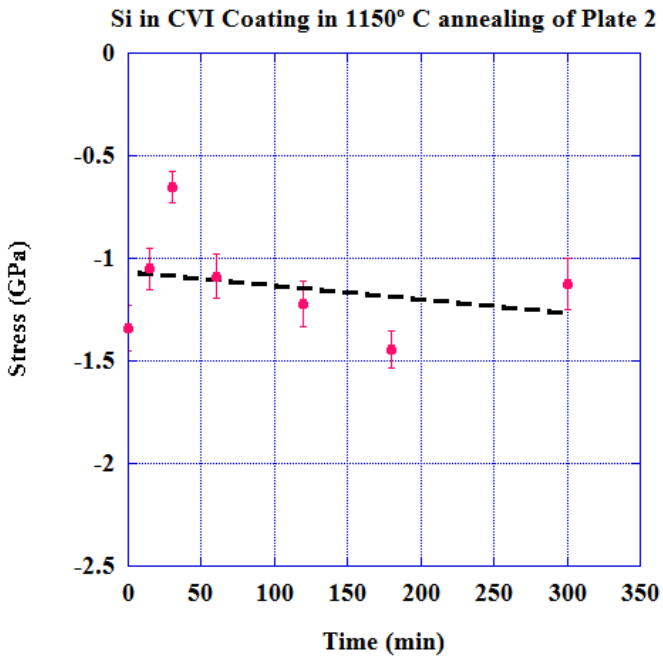

Figure 69: Si in CVI Residual Stress vs. Time for Plate 2 at 1150° C

The stresses within the excess silicon in the matrix are constant at -1.6 GPa throughout heat treatment. Within the CVI coating, the stresses are nearly constant averaging around -1.1 GPa, with some fluctuation at 30 minutes and 180 minutes.

4.7.3 Plate 1 Annealing Cycle at 1315º C

The results for the SiC constituents in Plate 1 for the annealing cycle completed at 1315º C can be seen in Figures 70 through 72. Figures 73 and 74 show the effects of the annealing cycle on the silicon components in Plate 1. The error bars shown are 95% confidence intervals. Dashed lines are to guide the eye, while solid lines represent curve fits.

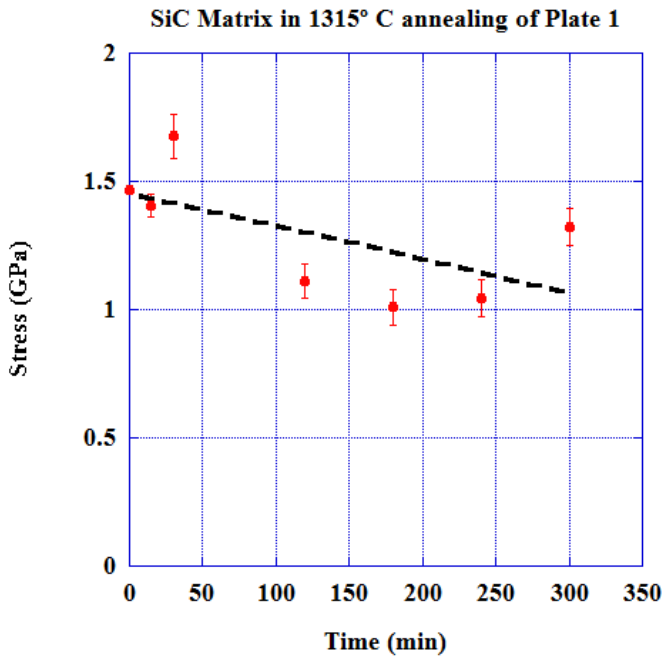

Figure 70: SiC Matrix Residual Stress vs. Time for Plate 1 at 1315° C

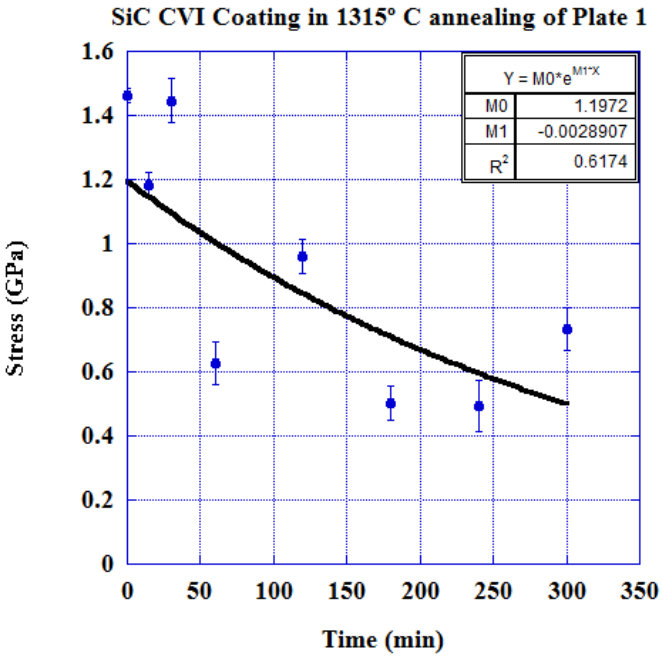

Figure 71: SiC CVI Residual Stress vs. Time for Plate 1 at 1315° C

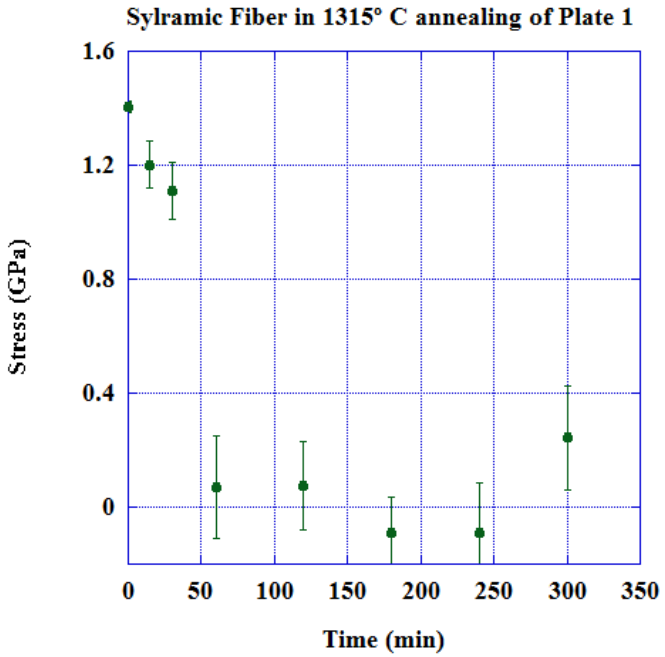

Figure 72: Sylramic Fiber Residual Stress vs. Time for Plate 1 at 1315° C

The SiC matrix stress begins at 1.5 GPa, and then decreases to around 1.1 GPa, with some fluctuation in the data. The stress within the SiC CVI coating also decays in an exponential manner, beginning near 1.3 GPa and decreasing to 0.6 GPa. The fiber stresses decrease from 1.2 GPa to near 0 GPa.

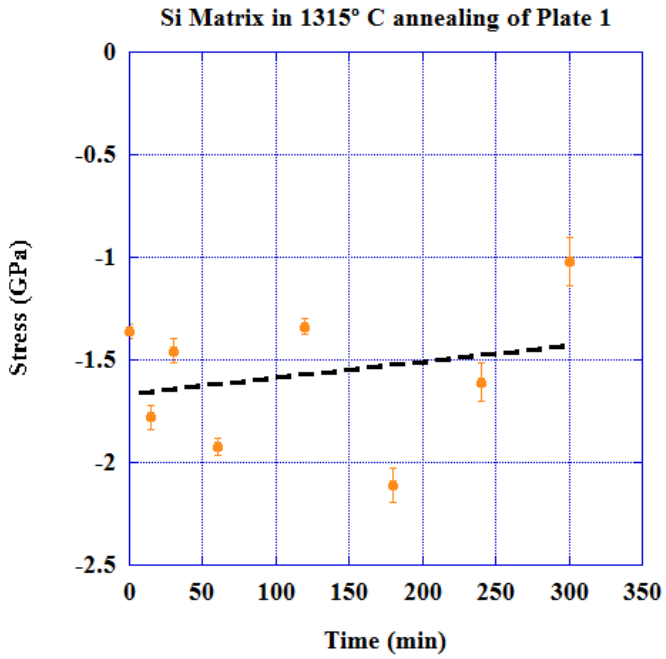

Figure 73: Si Matrix Residual Stress vs. Time for Plate 1 at 1315° C

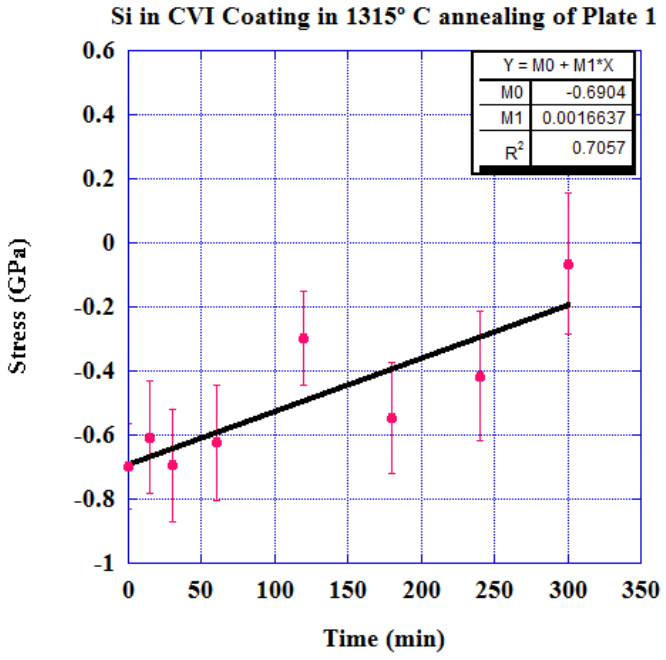

Figure 74: Si in CVI Residual Stress vs. Time for Plate 1 at 1315° C

The silicon within the matrix does not have a clear trend and there is a lot of fluctuation throughout the heat treatment. The stresses average around -1.5 GPa for the

excess silicon. For the silicon within the CVI, the stresses decrease from -0.7 GPa to -0.1 GPa.

4.7.4 Plate 2 Annealing Cycle at 1315º C

Figures 75 through 77 display the results for the SiC constituents in Plate 2 for the annealing cycle completed at 1315º C. The effects of the annealing cycle on the silicon components in Plate 1 are shown in Figures 78 and 79. The error bars shown are 95% confidence intervals. Dashed lines are to guide the eye, while solid lines represent curve fits.

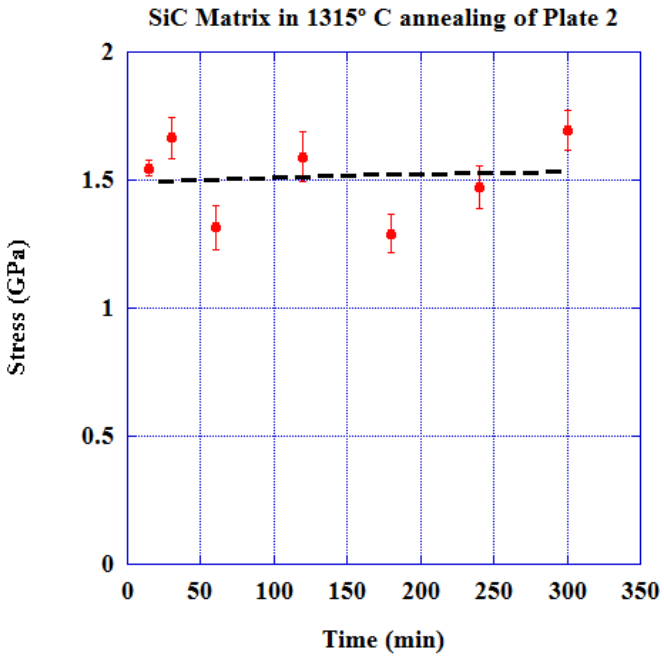

Figure 75: SiC Matrix Residual Stress vs. Time for Plate 2 at 1315° C

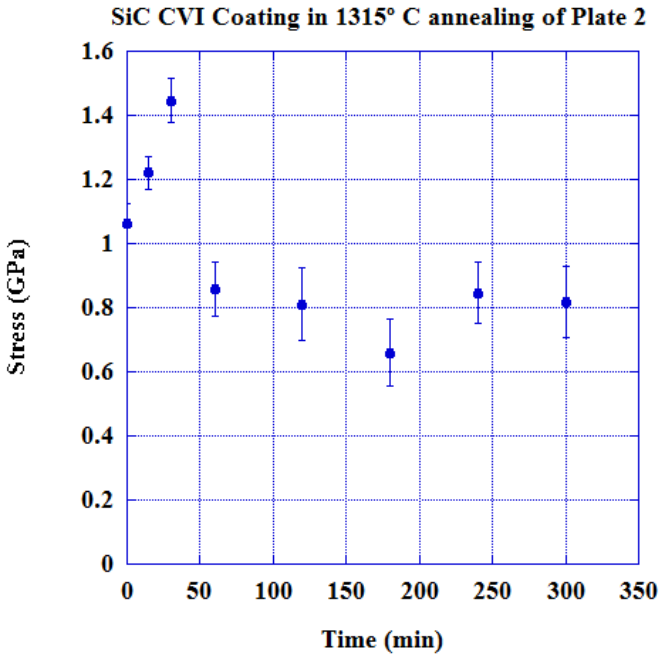

Figure 76: SiC CVI Residual Stress vs. Time for Plate 2 at 1315° C

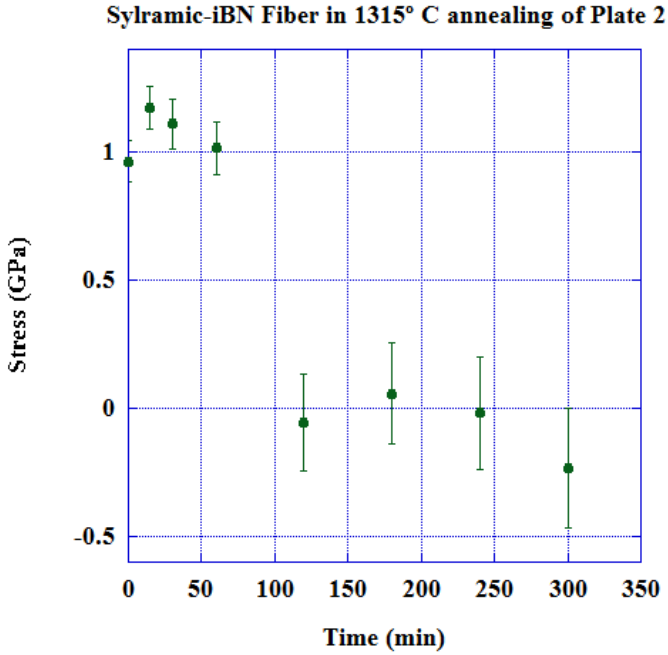

Figure 77: Sylramic-iBN Fiber Residual Stress vs. Time for Plate 1 at 1315° C

The SiC stresses within the matrix stay constant at 1.5 GPa in tension. The CVI SiC stresses decrease from around 1.2 GPa to 0.8 GPa in tension. The stresses within the fiber decrease from 1 GPa in tension to 0 GPa.

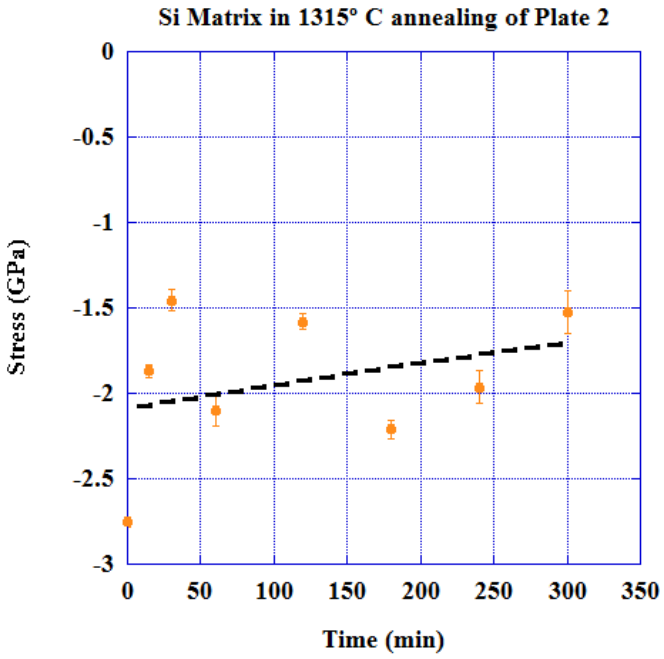

Figure 78: Si Matrix Residual Stress vs. Time for Plate 2 at 1315°

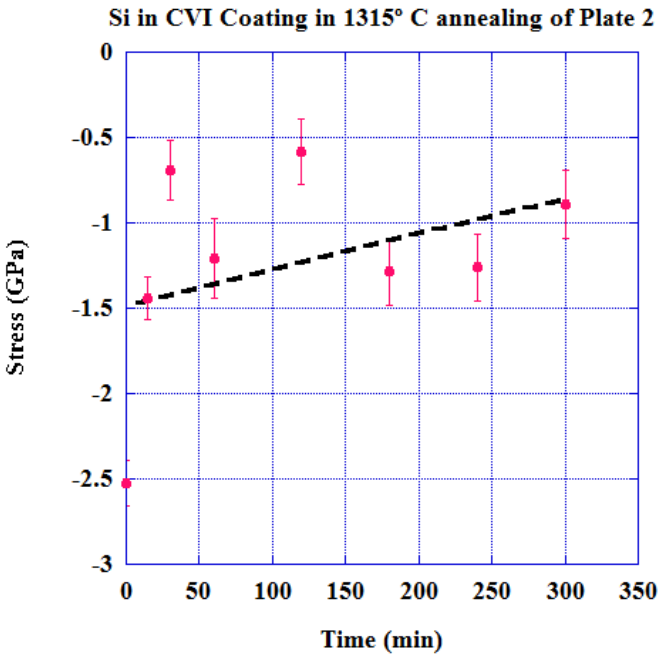

Figure 79: Si in CVI Residual Stress vs. Time for Plate 2 at 1315° C

Once again, as seen in Plate 1, the stresses within the silicon matrix do not have a clear trend for the heat treatment at 1315° C. The stresses seem to fluctuate around an average of -1.8 GPa in compression. The stresses in the silicon within the CVI also do not have a clear trend, fluctuating around -1 GPa.

4.7.5 Fiber Analysis

Figure 80 displays the behavior of the fiber stresses throughout heat treatments. The solid lines represent exponential fits.

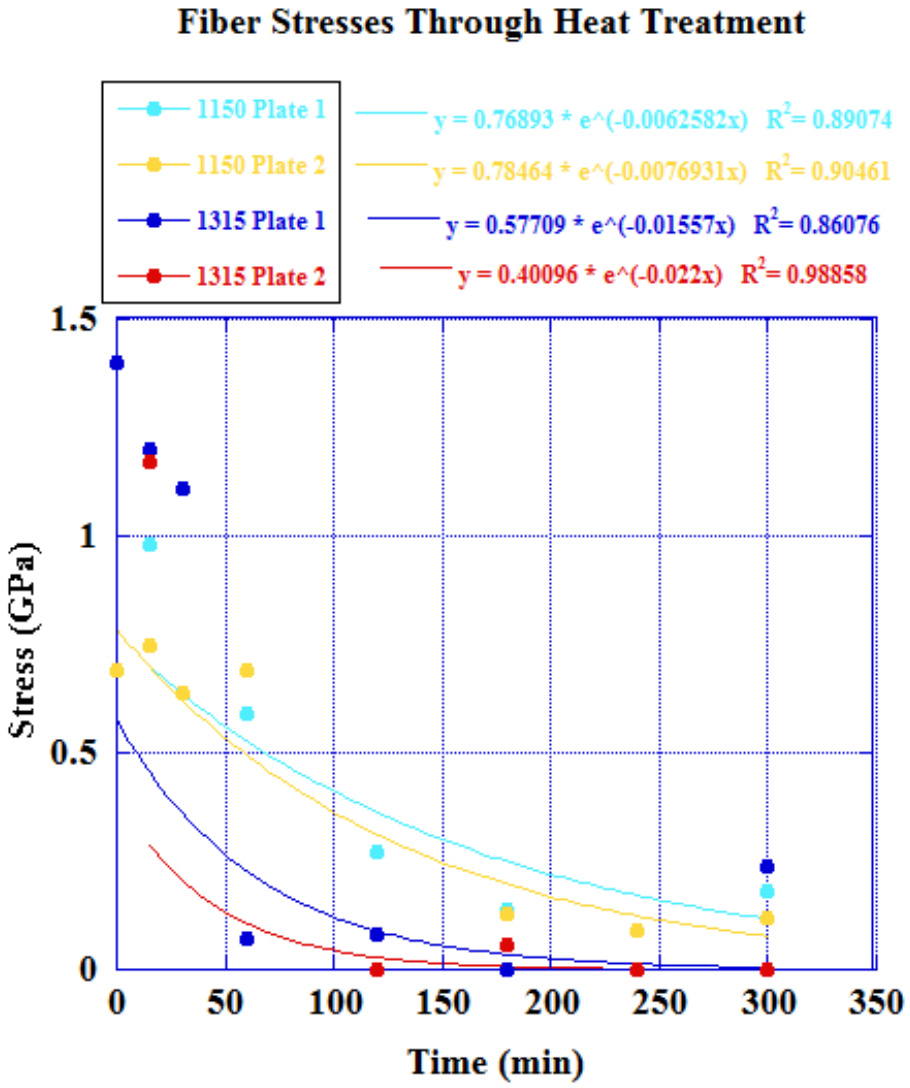

Figure 80: Fiber Stresses Throughout Heat Treatment

There are a few notable differences between the data sets. First, with the higher heat treatment at 1315° C, the stresses decay at a faster rate than the 1150° C heat treatment. Also, for the higher heat treatment, the stresses reach 0 GPa, while the lower heat treatment at 1150° C plateaus at 0.1 or 0.2 GPa in tension.

4.7.6 Summary of Heat Treatment Data

Table 18 provides a summary of each constituent for both heat treatment temperatures and plates.

Table 18: Summary of Raman Heat Treatment Data

	1150° C Plate 1	**1150° C Plate 2**	**1315° C Plate 1**	**1315° C Plate 2**
SiC Matrix	Constant *+1.5 GPa*	Constant *+1.5 GPa*	Decrease (w/ fluctuations) *+1.5 → +1.1 GPa*	Constant *+1.5 GPa*
SiC CVI	Constant *+1 GPa*	Constant *+1.1 GPa*	Decrease *+1.3 → +0.6 GPa*	Decrease *+1.2 → +0.8 GPa*
Fiber	Expo. Decay *+0.9 → +0.2 GPa*	Expo. Decay *+0.7 →+0.1 GPa*	Expo. Decay *+1.2 → 0 GPa*	Expo. Decay *+1 → 0 GPa*
Si Matrix	Decrease, then increase *-2.2 → -1.7 GPa*	Constant *-1.6 GPa*	No clear trend, averages around *-1.5 GPa*	No clear trend, averages around *-1.8 GPa*
Si within CVI	Constant *-0.5 GPa*	Constant (w/ fluctuations) *-1.1 GPa*	Decrease *-0.7 → -0.1 GPa*	No clear trend, averages around *-1 GPa*

4.8 Noncyclic Annealed Raman Spectroscopy Results

Specimens from each plate were annealed for ten hours straight at 1315º C. Similar to the cyclic annealing, a 30x30 micron area around a fiber was studied. Matrix-rich regions and silicon veins were studied as well.

4.8.1 Near fiber results

Similar results were seen near the fiber as seen previously with the cyclic annealing. The fiber stresses reduced nearly to zero in both plates. The SiC matrix stresses were similar before and after annealing, barring a few locations. At these locations, alpha SiC, detected by Raman, grew on spots that were previously just silicon grains. The compressive silicon stresses in the matrix and CVI reduced by about 1 GPa in both plates.

4.8.2 Matrix-rich regions

Two matrix-rich regions with no neighboring fibers or large silicon pools were studied in each plate before and after annealing. A map taken before annealing from Plate 1 can be seen in Figure 81. The SiC stresses range from 1 GPa to 3.5 GPa. The silicon stresses were nearly uniform at 0.75 GPa.

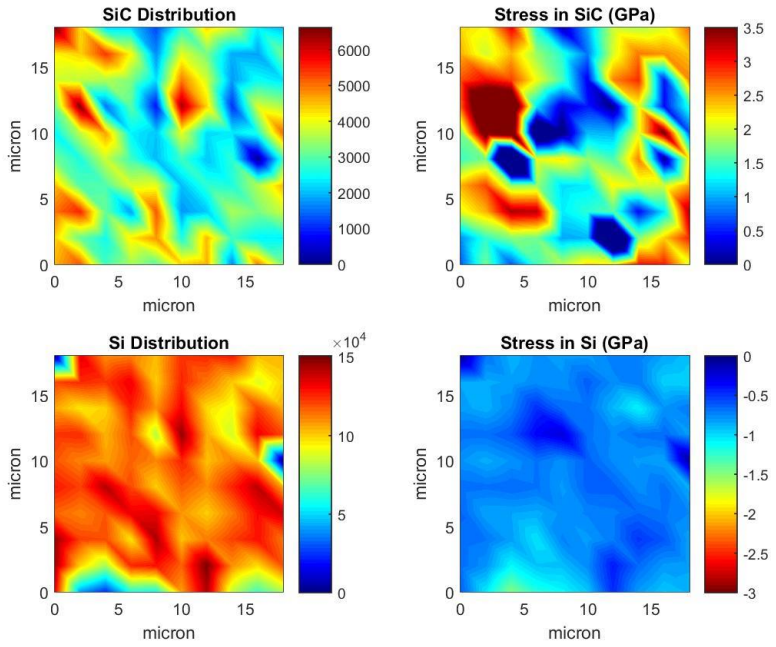

Figure 81: Raman maps of matrix-rich region in Plate 1 before anneal

Following the 10 hour anneal, the stresses changed slightly. The measured SiC stresses became had a lower range, but were more consistently near 3 GPa. The silicon stresses stayed nearly constant around 0.75 GPa. The post-anneal images can be seen in Figure 82.

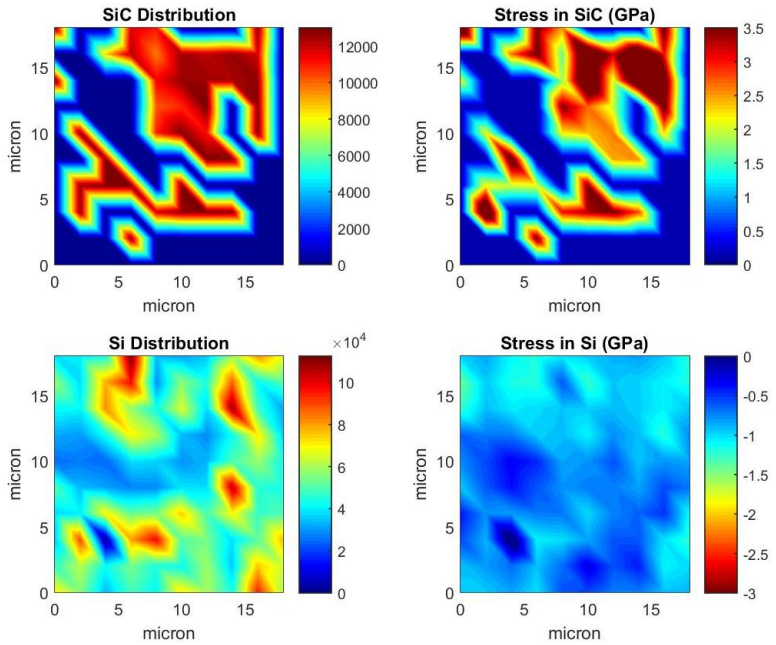

Figure 82: Raman maps of matrix-rich region in Plate 1 after anneal

However, slightly different trends were seen for Plate 2. The as-received matrix rich region for Plate 2 can be seen in Figure 83. The SiC stresses range from 1.5 to 3 GPa. The silicon stresses are nearly constant near 1.5 GPa in compressive residual stress.

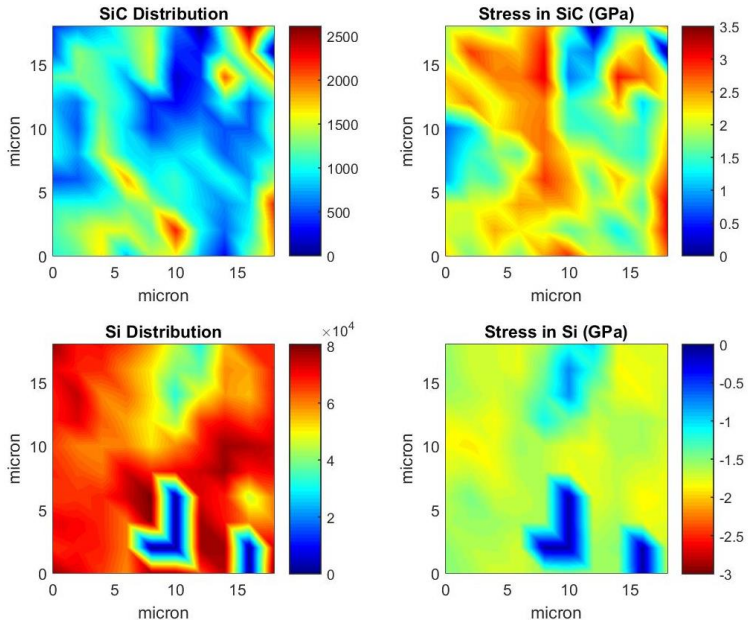

Figure 83: Raman maps of matrix-rich region in Plate 2 before anneal

As seen in Plate 1, the measured residual stresses in the SiC reduced their range and averaged around 3 GPa. However, unlike Plate 1, the residual stresses within the silicon reduced from 1.5 GPa to 1 GPa on average. The composition and stress maps for Plate 2 for after the anneal are in Figure 84.

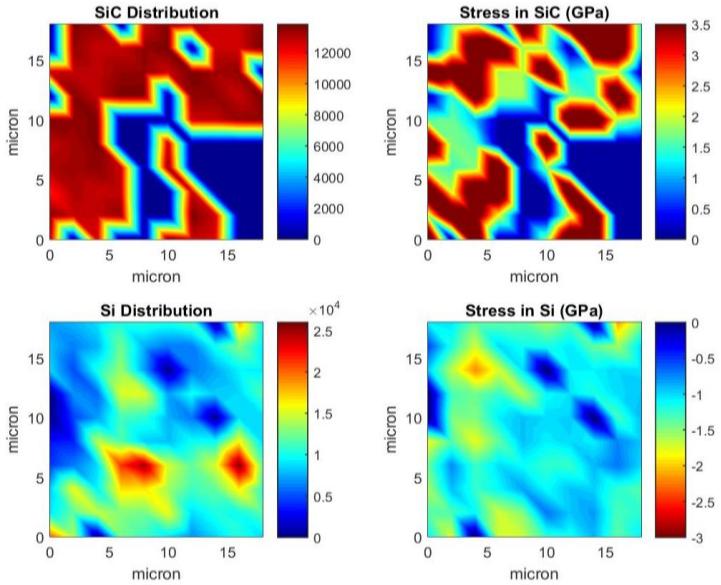

Figure 84: Raman maps of matrix-rich region in Plate 2 after anneal

4.8.3 Silicon Vein Regions

Two silicon veins in each plate were analyzed before and after annealing. The veins ranged from 2 to 5 microns in thickness where measured, and were not connected to the larger pools found within the composite. The veins were between two plies, and the measurement was taken in the middle of the two plies.

Before annealing, the SiC stresses in Plate 1 were near 1 GPa near the silicon vein, as seen in Figure 85. The silicon stresses had a gradient near the vein itself, and then stabilized (zoomed in image seen in Figure 86). The vein itself was measured to be stress-free, while the matrix near it had stresses averaging 2.5 GPa in compression.

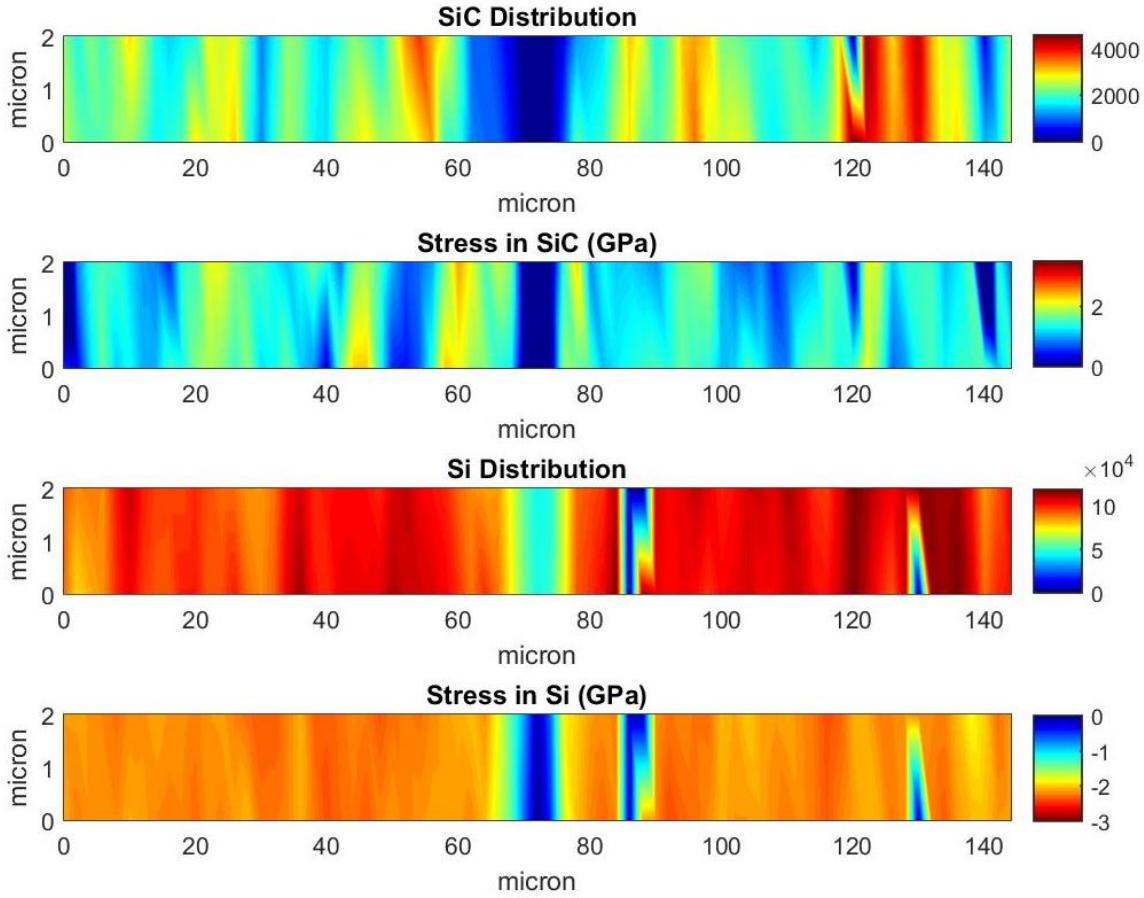

Figure 85: Raman maps of silicon vein in Plate 1 before anneal (vein is in light blue in Si Distribution map)

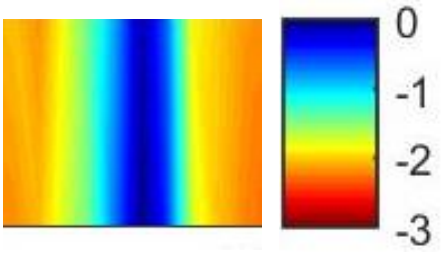

Figure 86: Zoomed image of stress gradient in silicon vein from Figure 85 (units in GPa)

Following the heat treatment, the SiC stresses were fairly stable, with a few spots spiking, similar to the previous 10 hour heat treated data. The SiC matrix near the silicon vein averaged 1 GPa. The silicon within the vein remained at 0 GPa in stress, but the silicon matrix surrounding it lowered, averaging at 1.75 GPa in compression. The Raman maps for annealed Plate 1 are in Figure 87.

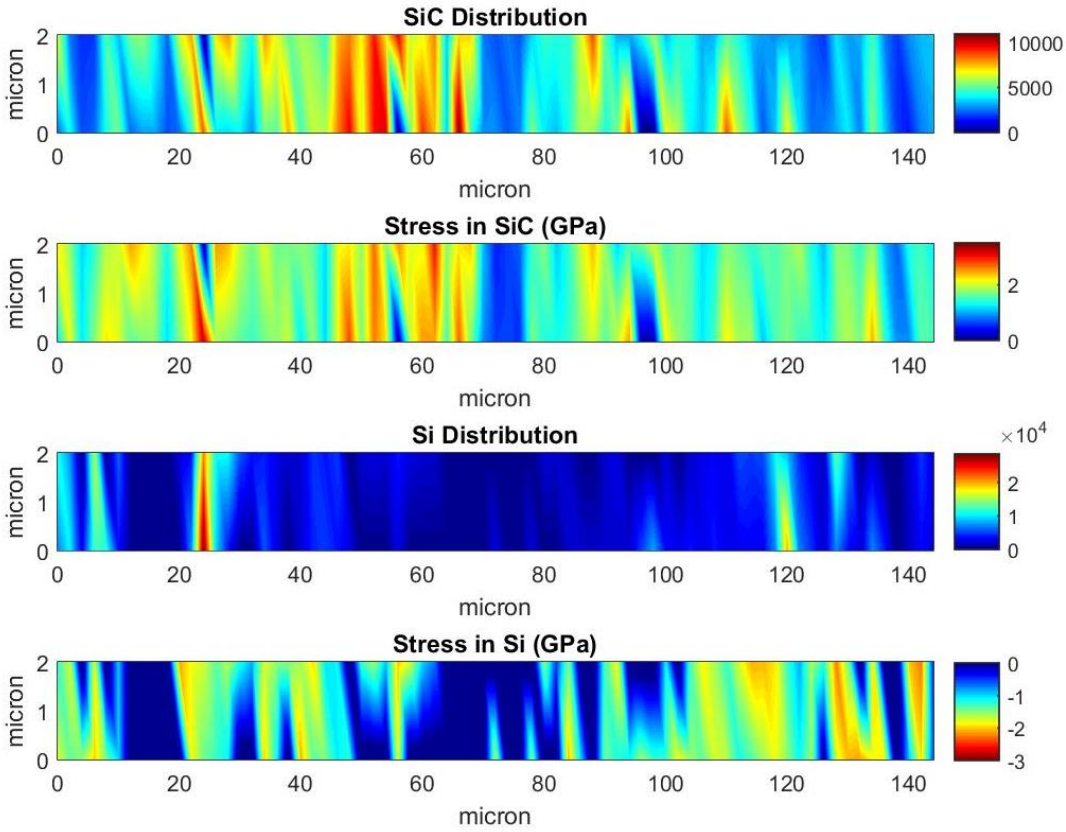

Figure 87: Raman maps of silicon vein in Plate 1 after anneal

Plate 2 exhibited similar behavior to Plate 1 near the silicon veins. As seen in Figure 88, before annealing, the SiC matrix stress ranged from 0 GPa to 3 GPa. The silicon stress within the vein was at 0 GPa, while the silicon matrix surround it was near 3 GPa in compression.

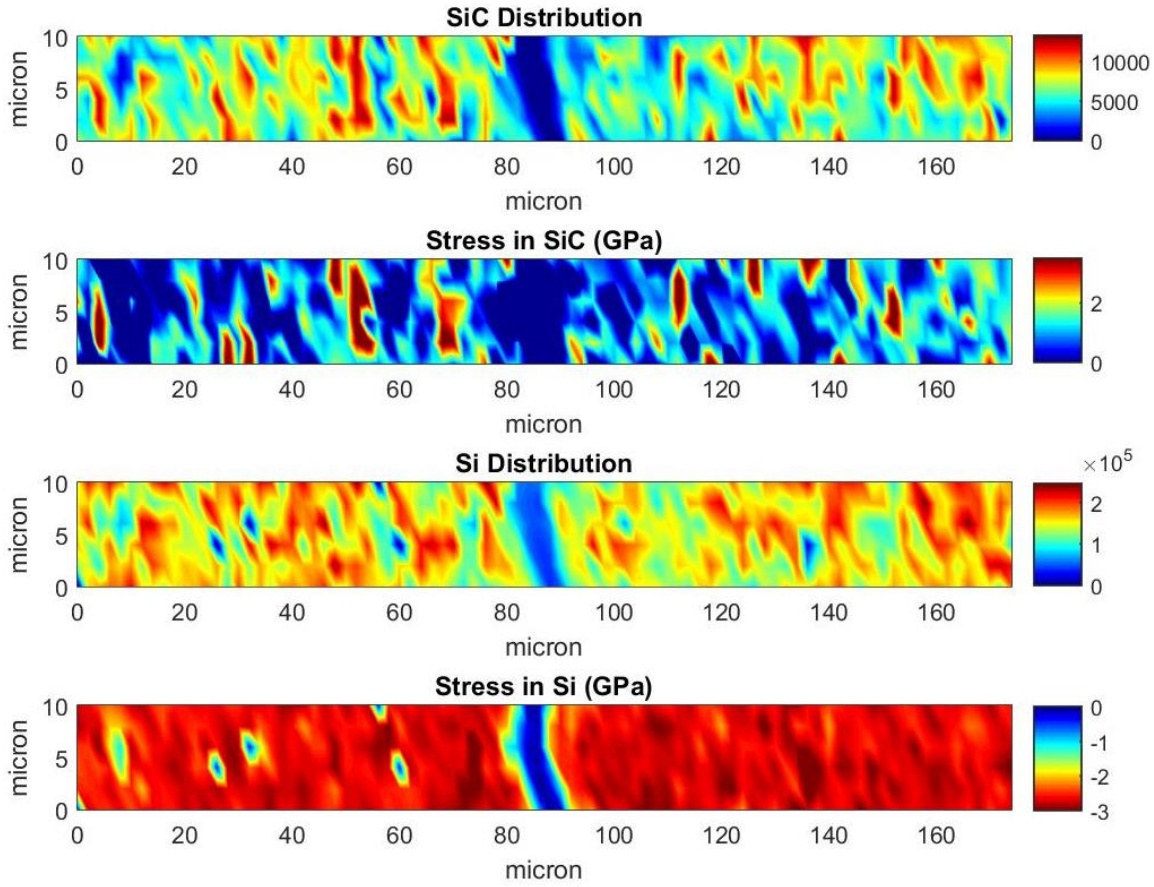

Figure 88: Raman maps of silicon vein in Plate 2 before anneal (vein is in light blue in Si Distribution map)

Following the heat treatment, the SiC stresses varied from 1 GPa to 3 GPa spikes. The areas where the high stress spikes occurred were where alpha SiC formed during the heat treatment. The stresses in the silicon reduced from a uniform 3 GPa in compression

to a range of stresses from 1 GPa to 2 GPa in compression, seen in Figure 89. The stress gradient on the silicon vein was no longer seen after heat treatment.

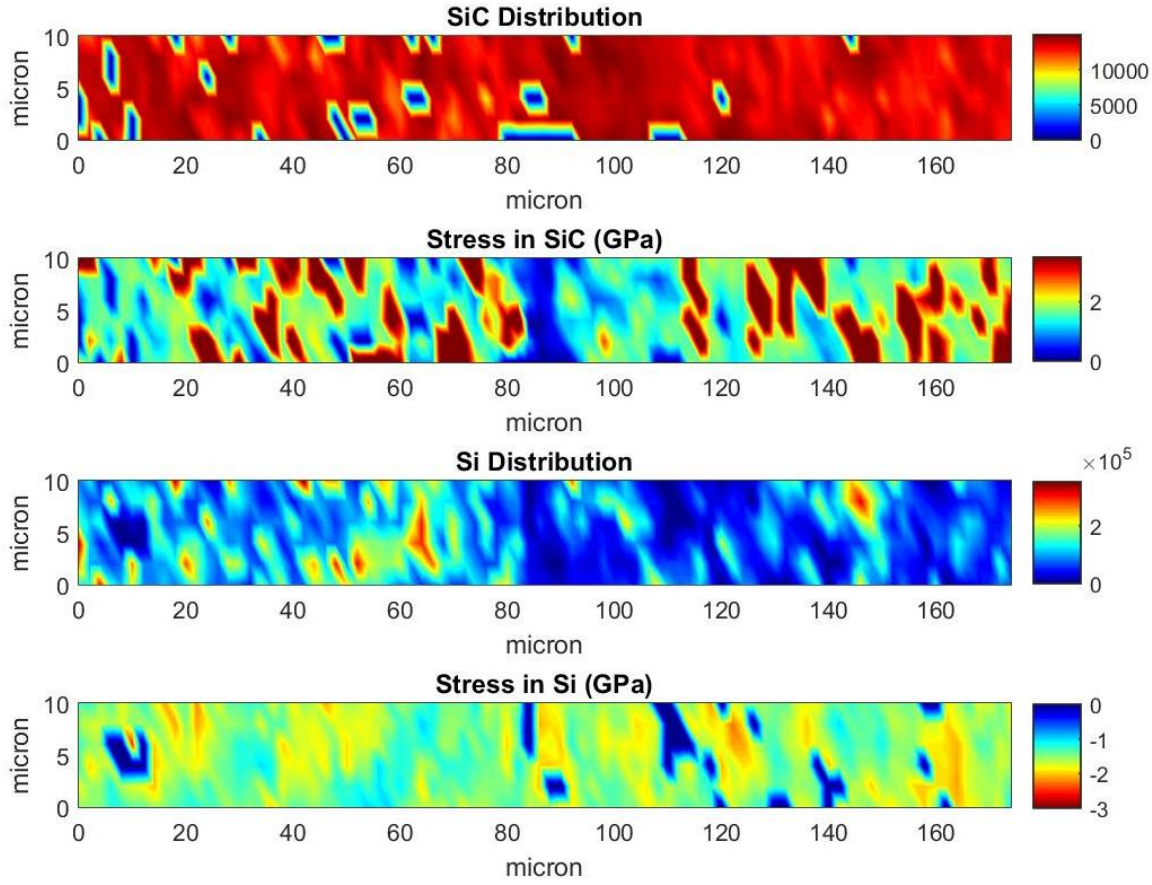

Figure 89: Raman maps of silicon vein in Plate 2 after anneal

V. DISCUSSION

This chapter will provide an analysis on the data collected in this study. First, the macro-residual stress measurements will be discussed, including the indentation cracking and mechanical testing. Second, the micro-residual stresses measured with Raman will be analyzed.

5.1 Macro-Residual Stress Measurements

5.1.1 Indentation Cracking

As mentioned previously, the model used for the crack indentation data processing is the simplest model available. This model was chosen due to uncertainty in the constants for the more advanced models. To improve upon this study, it would be imperative to use the more advanced models. Also, as in other crack indentation studies, the reference crack is typically done on a stress-free reference material, which was not available for this study. The assumption was made that the absence of delaminations propagating in the x-direction is indicative of low stresses in the z-direction. This assumption will bring error into the value for the stress-free reference crack used for the residual stress calculation. For all of the reasons listed above, the data presented should be looked at in a more qualitative manner than as an absolute value. It is clear to see that there is a decrease in the compressive residual stresses after annealing, but the exact value of this change cannot be accurately discerned from crack indentation testing.

There were a few difficulties experienced when conducting the crack indentation experiments. First, due to the weave geometry, some of the prepared samples had less

exposed free matrix area to test. To alleviate this, more samples had to be made for Plate 2. However, the additional samples were prepared in the exact same manner as the originals to help avoid any additional error. Also, some of the produced cracks were immeasurable due to two different scenarios. First, the cracks propagated and joined together, but left the matrix material surrounding it. Second, in some indents, when these cracks joined together, it resulted in the loss of matrix material around the indent. When this occurred, the cracks emanating from these indents were not considered. An attempt was made to fix this occurrence by using lower indent loads, but no visible cracks were seen at the lower available loads. In the future, one may try to avoid these issues by using an indenter with intermediate loads, such as 750 grams.

5.1.2 Mechanical Testing

Four dogbone samples from each plate were tensile tested, with two being as-received and two being annealed for ten hours at 1315° C. The magnitude of change in the elastic moduli, proportional limits, and AE onset stresses are within the bounds of ceramic variability. More tests would need to be run to understand if it is actually a slight change in the properties or if it is only ceramic variability accounting for these small differences in properties. For Plate 1, the changes in the ultimate tensile strength and ultimate strain are also within this variability, while these properties for Plate 2 are not. The large decreases in ultimate tensile strength (84 MPa) and ultimate strain (0.12%) for Plate 2 cannot only be explained by variability. The ultimate tensile strength and ultimate strain are dependent upon fiber strength and fiber content [3]. There is no loss in fiber content from heat treatment, meaning it is likely a loss in fiber strength causing the drop in these properties.

With these results, on the macro-scale, it is unlikely that a 10 hour heat treatment at 1315° C will cause a major change in residual stresses within the material. This is evidenced by the relatively low changes in the proportional limits and the AE onset stresses. If there were a major change in the compressive residual stresses, these values for the annealed specimens would be much lower than the as-received specimens, indicating crack growth occurring at lower stresses as there are lower compressive loads impeding cracking. These results are unlike Neal Gordon's thesis [44], in which there were notable differences in the proportional limits and AE onset stresses. Specifically, for a 0/90 specimen, Gordon noted a drop from 230 MPa to 150 MPa in the proportional limit and a decrease from 200 MPa to 140 MPa for the first AE event. There are many differences between these data sets, including fiber type, geometry, matrix processing, and likely the annealing procedure. The heat treatment was unknown in Gordon's work, and differences in the heat treatment procedure would greatly affect the outcome of the mechanical testing.

5.2 Micro-Residual Stress Measurements

5.2.1 Silicon Conversion Factor

The shift to stress conversion factor used to calculate the residual stresses in the silicon phases is for pure silicon. However, the silicon phase in this composite is doped with boron. This dopant may have an effect on the shift to stress conversion factor. Elemental analysis using an SEM revealed a 1.40 atomic weight percent of boron within the silicon. With the low dopant concentration, the standard value for the shift to stress conversion factor for silicon was used. In the future, to ensure that the use of this

constant is correct, one could complete studies of the powdered samples in a diamond anvil cell, similar to that of Digregorio [23].

5.2.2 Potential Carbon Diffusion

Initially, carbon was only seen near the center of the fibers. However, throughout the annealing cycle, the carbon concentration within the matrix increased. There are two potential sources for this. The first, and more likely, source is carbon depositing upon the sample surface from the graphite furnace. Attempts were made to avoid this carbon deposition. Samples were annealed in argon filled quartz tubes inside of an oxygen rich furnace. However, the quartz tubes cracked at high temperatures, resulting in the samples oxidizing. As oxidation of CMCs is a complicated phenomenon in itself, this method proved to be undesirable for this study. The second potential source could be carbon diffusing through the sample originating from the fibers. In order to properly account for the carbon present in the matrix, future Raman work should be completed on samples that are annealed in a non-carbon furnace.

5.2.3 Stresses near fibers

On the microscale, extremely high stresses in the GPa range are measured with Raman spectroscopy. The stresses measured are much higher than that of Knauf's work, which measured both SiC and silicon constituents to be in the MPa range [47]. The data presented here matches Wing's values much more closely, with measurements being in the GPa range [30].

When not accounting for silicon expansion upon crystallization, and only considering thermal residual stresses, the predicted stresses are much lower than that measured with Raman spectroscopy. However, with the additional consideration of the

silicon expansion, the predicted values are much closer to those measured. With the model presented, while the stresses are underestimated in the silicon, CVI and matrix, it is understood that the correct magnitudes are being measured the correct trends are represented. With the model, it is seen that the SiC matrix stress is higher than that of the SiC CVI stress, which was also seen using Raman. Also, the silicon has the highest measured stresses, which is also true within the model.

However, measured stresses in the fiber are much lower than the calculated values. Such reductions in the measured stresses have been shown to be direct results of interfacial adhesion and fiber fragmentation within the composite [75-81]. However, this phenomenon is more likely attributed to a relief of the stresses near the weak BN interface between the fiber and the CVI SiC. Under these length scales, it would be unlikely that fragmentation within the SiC fiber would occur.

Between the two plates, silicon in the matrix material surrounding the fiber was detected less in Plate 1 than in Plate 2. The local areas with less detected silicon is associated with a slightly higher compressive residual stress measured for the silicon phase. This same observation was also seen in both Wing, et. al and Jannotti, et. al, where lower silicon volume fractions resulted in higher measured stresses in those local areas.

Similar to Jannotti et. al, the small silicon grains present in this study were all under uniform compression, and did not experience tensile stresses. When Jannotti et. al measured stresses near irregularly shaped or large grains, tensile stresses were measured within the center of the grain. While tensile stresses were not measured within the silicon

in this study, the center of the large silicon pools were the lowest measured stresses for silicon, near 0 GPa.

While the cyclical data varies between each plate and temperature, there are some general trends to be noted for the constituents near a fiber. First, throughout the heat treatments, the SiC constituents are always in tension, while the silicon constituents are always in compression. Also, whether it be the silicon within the CVI or the SiC CVI itself, the stresses are almost always lower for the CVI than the matrix material throughout the heat treatments. The SiC MI matrix material typically stays constant at 1.5 GPa in tension throughout the heat treatment cycle. For the SiC CVI, the stresses stay constant when annealed at 1150° C. However, when the heat treatments were conducted at 1315° C, the CVI SiC stresses decreased in both plates. As the material heated up near the melting point of silicon, the silicon softens, losing stiffness and pushing less on the SiC particulates surrounding it. The fiber stresses decreased for all plates and temperatures. As seen in Figure 80, the stresses decreased at a higher exponential rate in the 1315° C anneal than the lower temperature heat treatment.

The trends for silicon are not as clear as the SiC trends. For instance, for Plate 1 at 1150° C, the silicon matrix material behaves unexpectedly. As seen in Figure 63, the stresses have a sharp initial decrease from -2.2 GPa, and then increase again to plateau out at -1.7 GPa. This increase would suggest that the silicon matrix is stiffening with the annealing cycle, which is unlikely. It is possible that another mechanism such as boron, from the doping or boron nitride fiber coatings, or carbon from the furnace, is diffusing through the silicon. However, for the silicon matrix material for Plate 2 at 1150° C, the stresses stay constant around -1.6 GPa. Assuming there are no differences in the melt

infiltrated silicon, the silicon should behave similarly in both plates. Therefore, it is unclear if there is a change in the silicon matrix stresses at 1150° C. The stresses for the silicon contained within the CVI stayed constant for both plates, although Plate 2 had much higher stresses of -1.1 GPa while Plate 1 had stresses of -0.5 GPa.

At 1315° C, there is much more scatter for the silicon data. For Plate 1, the silicon matrix fluctuates around an overall negative trendline, with a net decrease of 0.4 GPa. The silicon matrix material for Plate 2 behaves in a similar manner, with a net decrease of 0.4 GPa. The silicon within the CVI for Plate 1 has a linear decrease from -0.7 to -0.1 GPa. However, for silicon within the CVI for Plate 2, the data fluctuates around an overall negative trendline, but still has an overall decrease of 0.6 GPa. With the uncertainty in behavior for the cyclic annealing of silicon near a fiber, it was decided to instead anneal at 1315° C for 10 hours straight and study more areas. This type of fluctuation was not seen in Wing's work, in which the stresses exponentially decayed in both the silicon and SiC within five hours at 1200° C.

5.2.4 Stresses in free matrix material

Matrix material away from fibers and large silicon pools were studied before and after the 10 hour anneal at 1315° C. In both plates, as expected, the SiC stresses did not change greatly. Small areas spiked in stress, but when studied further, it was determined that it only increased in places where alpha SiC grew on top of the excess silicon. This is actually an artificial change, as the alpha SiC peak has a different wavenumber than the beta SiC peak that has been used. Beta SiC's peak is at 796 cm^{-1}, where alpha SiC's peak is at 787 cm^{-1}. The difference in peaks would account for a 2.5 GPa increase, which is consistent with the maximums measured before and after anneals. Further work could be

completed in creating a more robust curve fitting routine with the ability to distinguish between alpha and beta SiC peaks. However, the silicon stresses stayed constant at -0.75 GPa for Plate 1 with heat treatment, but changed for Plate 2, from -1.5 GPa to -1 GPa. The difference in the initial stresses is not well understood, but it is possible that the stresses plateau at -0.75 GPa. Future work could include annealing Plate 2 for a longer period of time to see where the silicon stresses plateau, and if it would be equivalent to Plate 1's plateau point.

5.2.5 Stresses in silicon veins

The largest changes in stress occur near the silicon veins. Once again, the SiC stresses only appeared to increase where alpha SiC grew on the surface, as seen in the free matrix regions. However, the silicon surrounding the veins greatly changed. In Plate 1, the silicon matrix stresses decreased from -2.5 GPa to -1.75 GPa, while Plate 2 stresses decreased from -3 GPa to -1.5 GPa. With compressive stresses relieving in these zones, it could allow cracks to open much earlier in the matrix surrounding the silicon veins. Future work should be completed in crack mouth opening and density of as-received and annealed specimens.

VI. CONCLUSIONS

6.1 Conclusions

From this work, the following conclusions can be made:

1. With a 10 hour anneal at 1315° C, a decrease in the compressive residual stresses within the matrix was measured with crack indentation. With mechanical testing, a slight decrease in the proportional limit and AE onset was measured, potentially meaning a decrease in the compressive residual stresses within the matrix. However, due to the limited number of samples, it cannot be confirmed if this drop is simply due to ceramic variability or a true decrease in material properties. More testing would need to be completed to confirm this.
2. The ultimate tensile stress and ultimate strain decreased much more for Plate 2 containing Sylramic-iBN fibers than Plate 1 containing Sylramic fibers. However, even with this drop, the mechanical properties for the annealed Plate 2 were still greater than the as-received Plate 1.
3. Excess carbon was detectable in both fiber types with Raman, while previous studies did not detect the carbon bands.
4. High micro-stresses were measured within the composite through Raman spectroscopy. These high stresses were verified through modeling.

5. SiC matrix material is stable through heat treatments up to 1315° C, while the CVI SiC was affected by the heat treatment at 1315° C but not at 1150° C.
6. Tensile stresses within the fiber decreased exponentially at both 1150° C and 1315° C.
7. Compressive stresses measured in the unreacted silicon within the matrix rich regions are highest near silicon veins.

6.2 Future Work

The following are suggestions for future work:

1. Complete annealing in a non-carbon furnace to track potential carbon diffusion within the composite
2. Study matrix crack density and crack mouth opening of as-received and annealed specimens
3. Conduct more mechanical testing to verify effects of annealing
4. Study more areas within the composite, including large silicon pools, fiber tows, and trapped silicon within the fiber tows using Raman spectroscopy

APPENDIX I

3.8 Raman Mapping Code

```
clc
close all


%%
%Define Path
textpath = 'C:\Users\K3\Documents\Raman Results Round 3\1150\T0\02-215\LEFT' ;

addpath('C:\Users\K3\Documents\Raman Results');
addpath(textpath);

%%
%Data collection information
c = 31;
r = 26;
cal = 520.025;
cal = cal - 520;

%%
%Image Read in

I = imread('Image.jpg');

I = imresize(I,[r,c]);

imshow(I)
set(gcf, 'Position',get(0,'Screensize'));
set(gca,'Ydir','Normal')
clickpointsdialog
[x,y,z] = ginput(4);

horizontalradius = (x(4)-x(3))./2;
verticalradius = (y(2) - y(1))./2;
centerx = ((x(3)+x(4))./2)-1;
centery = ((y(1)+y(2))./2)-1;

imshow(I)
```

```
set(gcf, 'Position',get(0,'Screensize'));
set(gca,'Ydir','Normal')
clickpointsdialog2
[x,y,z] = ginput(4);

horizontalradius2 = (x(4)-x(3))./2;
verticalradius2 = (y(2) - y(1))./2;
centerx2 = centerx;
centery2 = centery;

%%
%%Define Fiber and CVI Coating Locations on Maps

Fiber = zeros(r,c);

for i=1:r
   for j=1:c
      if (((i-centerx).^2./horizontalradius.^2)+((j-centery).^2./verticalradius.^2) <= 1)
         Fiber(i,j) = 1;
      end
   end
end

CVI = zeros(r,c);

for i=1:r
   for j=1:c
      if (((i-centerx).^2./horizontalradius2.^2)+((j-centery).^2./verticalradius2.^2) <= 1)
         CVI(i,j) = 1;
      end
   end
end

CVI = CVI - Fiber;
Matrix = ones(r,c);
Matrix = Matrix - Fiber - CVI;
%%
%%SiC Composition Map
%Read in .txt file
A = dlmread('SiC Peak Area.txt');

%Obtain data from .txt file

SiCArea = A(1:length(A),1);

%Reorient matrix
```

```
SiCA = (transpose(reshape(SiCArea, c, r)));

%Find Maximum
MaxSiCA = max(max(SiCA));

%Eliminate low area peaks
SiCA(find(SiCA<0)) = 0;
Eliminator = MaxSiCA * .05;
SiCA(find(SiCA<Eliminator)) = 0;
Eliminator = MaxSiCA * .95;
SiCA(find(SiCA>Eliminator)) = 0;
k = find(~SiCA);

%Setup composition map
[F,G]=meshgrid (0:1:(c-1),0:1:(r-1));

figure
ax1 = subplot(3,2,1)
set(gcf, 'Position',[520 378 560 420]);
set(gca,'Ydir','Normal')
pcolor (F, G, SiCA), colorbar          %creates a pseudocolor plot
colormap(ax1, 'jet')
shading interp         %removes the grid line
xlabel('micron')
ylabel('micron')
title ('SiC Distribution')

%Fiber Ellipse
hold on
plotellipse(centerx, centery, horizontalradius, verticalradius)
% CVI Ellipse
hold on
plotellipse(centerx, centery, horizontalradius2, verticalradius2)

%%
%%SiC Residual Stress Plot
%Read in .txt file
B = dlmread('SiC Peak Position.txt');

%Obtain data from .txt file
SiCWN = B(1:length(A),1);

%Reorient matrix
SiCP = (transpose(reshape(SiCWN, c, r)));

%Eliminate zeroes
```

```
SiCP(k) = 796;

%Solve for Residual Stresses
SiCS=((796-SiCP+cal)/3.53);

SiCSFiber = SiCS .* Fiber;
SiCSFiberAve = mean(SiCSFiber(find(SiCSFiber)));
SiCSFiberMax = max(max((SiCSFiber)));
SiCSFiberR = reshape(SiCSFiber, [1, c*r]);
SiCSFiberR(SiCSFiberR == 0) = NaN;
SiCSFiberStdDev = nanstd(SiCSFiberR);

SiCSCoating = SiCS .* CVI;
SiCSCoatingAve = mean(SiCSCoating(find(SiCSCoating)));
SiCSCoatingMax = max(max((SiCSCoating)));
SiCSCoatingR = reshape(SiCSCoating, [1, c*r]);
SiCSCoatingR(SiCSCoatingR == 0) = NaN;
SiCSCoatingStdDev = nanstd(SiCSCoatingR);

SiCSMatrix = SiCS .* Matrix;
SiCSMatrixAve = mean(SiCSMatrix(find(SiCSMatrix)));
SiCSMatrixMax = max(max((SiCSMatrix)));
SiCSMatrixR = reshape(SiCSMatrix, [1, c*r]);
SiCSMatrixR(SiCSMatrixR == 0) = NaN;
SiCSMatrixStdDev = nanstd(SiCSMatrixR);

%Setup peak position (residual stress) map
ax2 = subplot(3,2,2)
pcolor (F, G, SiCS), colorbar          %creates a pseudocolor plot
colormap(ax2, 'jet')
xlabel('micron')
ylabel('micron')
shading interp         %removes the grid line
caxis ([0,3.5])
title ('Stress in SiC (GPa)')

%Fiber Ellipse
hold on
plotellipse(centerx, centery, horizontalradius, verticalradius)
% CVI Ellipse
hold on
plotellipse(centerx, centery, horizontalradius2, verticalradius2)


%%
%%Si Composition Map
```

```
%Read in .txt file
C = dlmread('Si Peak Area.txt');

%Obtain data from .txt file
SiArea = C(1:length(A),1);

%Reorient matrix
SiA = (transpose(reshape(SiArea, c, r)));

%Find Maximum
MaxSiA = max(max(SiA));

% Eliminate low area peaks
Eliminator = MaxSiA * .05;
SiA(find(SiA<Eliminator)) = 0;
SiA(find(SiA<0)) = 0;
Eliminator = MaxSiA * .95;
SiA(find(SiA>Eliminator)) = 0;
l = find(~SiA);

%Setup composition map
ax3 = subplot(3,2,3)
pcolor (F, G, SiA), colorbar          %creates a pseudocolor plot
colormap(ax3, 'jet')
xlabel('micron')
ylabel('micron')
shading interp        %removes the grid line
title ('Si Distribution')

%Fiber Ellipse
hold on
plotellipse(centerx, centery, horizontalradius, verticalradius)
%CVI Ellipse
hold on
plotellipse(centerx, centery, horizontalradius2, verticalradius2)

%%
%%Si Residual Stress Plot
%Read in .txt file
D = dlmread('Si Peak Position.txt');

%Obtain data from .txt file
SiWN =D(1:length(A),1);

%Reorient matrix
SiP = (transpose(reshape(SiWN, c, r)));
```

```
%Eliminate zeroes
SiP(l) = 515.286;


%Solve for Residual Stresses
SiS=((515.286-SiP+cal)/(1.88));

SiSFiber = SiS .* Fiber;
SiSFiberAve = mean(SiSFiber(SiSFiber~=0));
SiSFiberMax = min(min((SiSFiber)));
SiSFiberR = reshape(SiSFiber, [1, c*r]);
SiSFiberR(SiSFiberR == 0) = NaN;
SiSFiberStdDev = nanstd(SiSFiberR);

SiSCoating = SiS .* CVI;
SiSCoatingAve = mean(SiSCoating(SiSCoating~=0));
SiSCoatingMax = min(min((SiSCoating)));
SiSCoatingR = reshape(SiSCoating, [1, c*r]);
SiSCoatingR(SiSCoatingR == 0) = NaN;
SiSCoatingStdDev = nanstd(SiSCoatingR);

SiSMatrix = SiS .* Matrix;
SiSMatrixAve = mean(SiSMatrix(SiSMatrix~=0));
SiSMatrixMax = min(min((SiSMatrix)));
SiSMatrixR = reshape(SiSMatrix, [1, c*r]);
SiSMatrixR(SiSMatrixR == 0) = NaN;
SiSMatrixStdDev = nanstd(SiSMatrixR);

%Setup peak position (residual stress) map
ax4 = subplot(3,2,4)
pcolor (F, G, SiS), colorbar          %creates a pseudocolor plot
xlabel('micron')
ylabel('micron')
colormap(flipud(jet))
shading interp        %removes the grid line
caxis ([-3.5,0])
title ('Stress in Si (GPa)')

%Fiber Ellipse
hold on
plotellipse(centerx, centery, horizontalradius, verticalradius)
%CVI Ellipse
hold on
plotellipse(centerx, centery, horizontalradius2, verticalradius2)
```

```
%%
%%C Composition Map
%Read in .txt file
E = dlmread('C Peak Area.txt');

%Obtain data from .txt file
CArea = E(1:length(A),3);

%Reorient matrix
CA = (transpose(reshape(CArea, c, r)));

%Find Maximum
MaxCA = max(max(CA));

% Eliminate low area peaks
Eliminator = MaxCA * .05;
CA(find(CA<Eliminator)) = 0;
CA(find(CA<0)) = 0;
Eliminator = MaxCA * .95;
CA(find(CA>Eliminator)) = 0;
l = find(~CA);

%Setup composition map
ax5 = subplot(3,2,5)
pcolor (F, G, CA), colorbar        %creates a pseudocolor plot
colormap(ax5, 'jet')
xlabel('micron')
ylabel('micron')
shading interp         %removes the grid line
title ('C Distribution')

%Fiber Ellipse
hold on
plotellipse(centerx, centery, horizontalradius, verticalradius)
%CVI Ellipse
hold on
plotellipse(centerx, centery, horizontalradius2, verticalradius2)

%%
%Edit: Count Number of Matrix Elements for Confidence Intervals

NSiCSFiber = nnz(SiCA.*SiCSFiber);
NSiCSCoating = nnz(SiCA.*SiCSCoating);
NSiCSMatrix = nnz(SiCA.*SiCSMatrix);
```

```
NSiSFiber = nnz(SiA.*SiSFiber);
NSiSCoating = nnz(SiA.*SiSCoating);
NSiSMatrix = nnz(SiA.*SiSMatrix);

%%
%%Data Message Box
ax = subplot(3,2,6)
text(-0.30, 0.5, {['SiC Fiber Average: ',num2str(SiCSFiberAve)]...
   ['SiC Fiber Max: ',num2str(SiCSFiberMax)]...
   ['SiC Fiber Std. Dev.: ',num2str(SiCSFiberStdDev)]...
   ['SiC CVI Coating Average: ',num2str(SiCSCoatingAve)]...
   ['SiC CVI Coating Maximum: ',num2str(SiCSCoatingMax)]...
   ['SiC CVI Coating Std. Dev.: ',num2str(SiCSCoatingStdDev)]...
   ['SiC Matrix Average: ',num2str(SiCSMatrixAve)]...
   ['SiC Matrix Maximum: ',num2str(SiCSMatrixMax)]...
   ['SiC Matrix Std. Dev.: ', num2str(SiCSMatrixStdDev)]})
text(0.55, 0.5, {['Si CVI Coating Average: ',num2str(SiSCoatingAve)]...
   ['Si CVI Coating Maximum: ',num2str(SiSCoatingMax)]...
   ['Si CVI Coating Std. Dev.: ',num2str(SiSCoatingStdDev)]...
   ['Si Matrix Average: ',num2str(SiSMatrixAve)]...
   ['Si Matrix Maximum: ',num2str(SiSMatrixMax)]...
   ['Si Matrix Std Dev: ', num2str(SiSMatrixStdDev)]})
set(ax, 'visible', 'off')


print('Raman Summary', '-djpeg')


a = [SiCSFiberAve; SiCSFiberMax; SiCSFiberStdDev; NSiCSFiber; SiCSCoatingAve;
SiCSCoatingMax; SiCSCoatingStdDev; NSiCSCoating; SiCSMatrixAve;
SiCSMatrixMax; SiCSMatrixStdDev; NSiCSMatrix; SiSFiberAve; SiSFiberMax;
SiSFiberStdDev; NSiSFiber; SiSCoatingAve; SiSCoatingMax; SiSCoatingStdDev;
NSiSCoating; SiSMatrixAve; SiSMatrixMax; SiSMatrixStdDev; NSiSMatrix];

fileID = fopen('Stress Data.txt','w');
fprintf(fileID, '%8.4f\n', a);
fclose(fileID);

rmpath(textpath)
```

4.2 Theoretical Residual Stress Calculations

Plate 1:

lambda = 0.5

Ef = 400E09
Vf = .41/(.54+.41)
alphaf = 5.4E-06

Em = (.35*(310E09) + .19*(380E09))/(.35+.19)
Vm = .54/(.54+.41)
alpham = (.35*(4.7E-06) + .19*(4.6E-06))/(.35+.19)

To = 24
Tp = 1400

A = Em*(alphaf-alpham)*(To-Tp)
F = lambda*Ef*Vf
M = Em*Vm

RS = (F/(F+M))*A

Plate 2:

lambda = 0.5

Ef = 400E09
Vf = .46/(.51+.46)
alphaf = 5.4E-06

Em = (.29*(310E09) + .22*(380E09))/(.29+.22)
Vm = .51/(.51+.46)
alpham = (.29*(4.7E-06) + .22*(4.6E-06))/(.29+.22)

To = 24
Tp = 1400

A = Em*(alphaf-alpham)*(To-Tp)
F = lambda*Ef*Vf
M = Em*Vm

RS = (F/(F+M))*A

WORKS CITED

1. N. P. Bansal, J.L., *Ceramic matrix composites: materials, modeling and technology*. 2015, Hoboken, New Jersey: John Wiley & Sons, Inc.
2. Li, J.C.M., *Microstructure and properties of materials*. 1996, Singapore: World Scientific.
3. Dicarlo, J.A., Yun, H.M., Morscher, G. N., & Bhatt, R.T., *SiC/SiC composites for 1200 C and above*, in *Handbook of Ceramic Composites*. 2005, Springer US. p. 77-98.
4. Dowling, N.E., *Mechanical behavior of materials: Engineering methods for deformation, fracture, and fatigue*. 2007, Upper Saddle River, N.J.: Pearson/Prentice Hall.
5. Miracle, D.B., & Donaldson, S. L., *Introduction to composites*, in *ASM International*. 2001: Materials Park, OH. p. 3-17.
6. Corman, G.S., & Luthra, K. L., *Silicon melt infiltrated ceramic composites (HiPerComp)*, in *Handbook of Ceramic Composites*. 2005, Springer US. p. 99-115.
7. Harris, B., *Composite Materials Handbook: MIL HDBK 17-5*. 2002.
8. Schajer, G.S., *Practical residual stress measurement methods*. 2013, Chichester, West Sussex, United Kingdom: John Wiley & Sons Inc.
9. Swenson, C.A., *Recommended values for the thermal expansivity of silicon from 0 to 1000 K*. Journal of physical and chemical reference data, 1983. **12**(2): p. 179-182.
10. Slack, G.A., & Bartram, S.F., *Thermal expansion of some diamondlike crystals.* Journal of Applied Physics, 1975. **46**: p. 89.
11. Dicarlo, J.A., & Yun, H.M., *Non-oxide (silicon carbide) fibers*, in *Handbook of ceramic composites*. 2005, Springer US. p. 33-52.
12. Mei, H., *Measurement and calculation of thermal residual stress in fiber reinforced ceramic matrix composites.* Composites science and technology, 2008. **68**(15): p. 3285-3292.
13. Krenkel, W., *Cost effective processing of CMC composites by melt infiltration (LSI-process).* Ceramic Engineering and Science Proceedings, 2009: p. 443-454.
14. Vandenabeele, P., *Practical Raman spectroscopy: an introduction*. 2013, Chichester, West Sussex, United Kingdom: Wiley.
15. Hashmi, S., *Comprehensive Materials Processing*. 2014: Newnes.
16. Amer, M.S., *Raman spectroscopy, fullerenes and nanotechnology*. 2010: Royal Society of Chemistry.
17. Amer, M.S., & Schadler, L. S., *Effect of hydrothermal exposure on interfacial stress in graphite/epoxy composites loaded in compression.* Advanced Composites Letters (UK), 1996. **5**(6): p. 165-168.
18. M.A. Capano, B.C.K., A.R. Smith, et al., *Residual strains in cubic silicon carbide measured by Raman spectroscopy correlated with x-ray diffraction and transmission electron spectroscopy*. Journal of Applied Physics, 2006. **100**(8).

19. Gouadec, G., Karlin, S., Wu, J., Parlier, M., & Colomban, P., *Physical chemistry and mechanical imaging of ceramic-fibre-reinforced ceramic-or metal-matrix composites.* Composites science and technology, 2001. **61**(3): p. 383-388.
20. Wermelinger, T.S., R., *Confocal Raman Microscopy*. Springer Series in Optical Sciences, ed. T. Dieing, Hollricher, O., & Toporski, J. Vol. 158. 2010: Springer.
21. Amer, M., et. al, *Functionally graded joints for carbon/carbon composites: micro-Raman spectroscopy characterization.* 44th International SAMPE Symposium and Exhibition, 1999.
22. Zhu, W.L., Zhu, J. L., Nishino, S., & Pezzotti, G. , *Spatially resolved Raman spectroscopy evaluation of residual stresses in 3C-SiC layer deposited on Si substrates with different crystallographic orientations.* Applied surface science, 2006. **252**(6): p. 2346-2354.
23. DiGregorio, J.F., & Furtak, T.E., *Anaylsis of Residual Stress in 6H-SiC Particles with Al2o3/SiC Composites through Raman Spectroscopy.* Journal of the American Ceramic Society, 1992. **75**(7): p. 1854-1857.
24. Anastassikas, E., Cantarero, A., & Cardona, M., *Piezo-Raman measurements and anharmonic parameters in silicon and diamond.* Physical Review B, 1990. **41**(11): p. 7529.
25. G. Derst, C.W., K.L. Bhatia, W. Kratschmer, and S. Kalbitzer, *Optical Properties of SiC for crystalline/amorphous pattern fabrication.* Applied Physics Letters, 1989. **54**(18): p. 1722-1724.
26. Jr., G.E.J., *Optical functions of silicon determined by two-channel polarization modulation ellipsometry.* Optical Materials, 1992. **1**(1): p. 41-47.
27. Yang, X., Wang, Y. M., & Yuan, X. K. , *An investigation of microstructure of SiC/ceramic composites using Raman spectroscopy.* Journal of materials science letters, 2000. **19**(18): p. 1599-1601.
28. Gouadec, G., & Colomban, P., *Non-destructive mechanical characterization of SiC fibers by Raman spectroscopy.* Journal of the European ceramic society, 2001. **21**(9): p. 1249-1259.
29. Jannotti, P., Subhash, G., Zheng, J., & Halls, V., *Measurement of microscale residual stresses in multi-phase ceramic composites using Raman spectroscopy.* Acta Materialia, 2017. **129**: p. 482-491.
30. Wing, B.L., *Residual stresses and oxidation of silicon carbide fiber reinforced silicon carbide composites*. 2016, University of Michigan.
31. Chawla, K.K., *Ceramic Matrix Composites*. 2003, Boston, MA, USA: Kluwer Academic.
32. Tandon, R., Cook, R. E., *Indentation Crack Initiation and Propagation in Tempered Glass.* Journal of the American Ceramic Society, 1993. **76**: p. 885-889.
33. Zeng, K., Rowcliffe, D., *Experimental measurement of residual stress field around sharp indentation in glass.* Journal of the American Ceramic Society, 1994. **77**: p. 524-530.
34. Zeng, K., Giannakopoulos, A. E., Rowcliffe, D., and Meier, P., *Residual Stress Fields at the Surface of Sharp Pyramid Indentations.* Journal of the American Ceramic Society, 1998. **81**(3): p. 689-694.
35. Dunn, D.G., *The effect of fiber volume fraction in HiPerComp SiC-SiC composites*, in *Ceramics*. 2010, Alfred University: Alfred, NY.

36. Steen, M., & Filiou, C. *Mechanical property scatter in CFCCs*. in *ASME 1998 International Gas Turbine and Aeroengine Congress and Exhibition*. 1998. American Society of Mechanical Engineers.
37. Dassios, K.G., Aggelis, D. G., Kordatos, E. Z., & Matikas, T. E. , *Cyclic loading of a SiC-fiber reinforced ceramic matrix composite reveals damage mechanisms and thermal residual stress state.* Composites Part A: Applied Science and Manufacturing, 2013. **44**: p. 105-113.
38. Morscher, G.N., *Stress-dependent matrix cracking in 2D woven SiC-fiber reinforced melt-infiltrated SiC matrix composites*

Composites Science and Technology, 2004. **64**(9): p. 1311-1319.
39. Wadhwa, A.S., & Dhaliwal, E. H. S., *A Textbook fo Engineering Material and Metallurgy*. 2008: Firewall Media.
40. Rollett, A., Humphreys, F. J., Rohrer, G. S., & Hatherly, M., *Recrystallization and related annealing phenomena*. 2004: Elsevier.
41. Callister, W.D.R., D. G., *Materials science and engineering: an introduction*. Vol. 7. 2007, New York: Wiley.
42. Kotake, H., & Takasu, S. , *The effect of annealing on residual stress and dislocation propagation in silicon slices with damaged layer induced by scribing.* Journal of Materials Science, 1981. **16**(3): p. 767-774.
43. Maier-Schneider, D., Maibach, J., Obermeier, E., & Schneider, D. , *Variations in Young's modulus and intrinsic stress of LPCVD-polysilicon due to high-temperature annealing.* Journal of Micromechanics and Microengineering, 1995. **5**(2): p. 121.
44. Gordon, N., *Material health monitoring of SiC/SiC laminated ceramic matrix composites with acoustic emission and electrical resistance*. 2014, The University of Akron.
45. Kingery, W.D., *Note on Thermal Expansion and Microstresses in Two-Phase Compositions.* Journal of the American Ceramic Society, 1957. **40**(10): p. 351-2.
46. Turner, P.S., *Thermal-Expansion Stress in Reinforced Plastics.* J. Res. Natl. Bur. Stand., 1946. **37**: p. 230-50.
47. Knauf, M., *Effects of Heat Treatment on SiC-SiC Ceramic Matrix Composites*, in *Aeronautics and Astronautics*. 2017, Purdue: West Lafayette, Indiana.
48. Bhatt, R.T.D., J. A., *Method Developed For Improving the Thermomechanical Properties of Silicon Carbide Matrix Composites.* 2004.
49. *Synthetic Fibers and Fabrics Information*. [cited 2017 3/30/2017].
50. Dicarlo, J.A., & Yun, H.M., *New High-Performance SiC Fiber Develped for Ceramic Composites*, N.A.a.S. Administration, Editor. 2002: NASA Glenn Research Center.
51. Composites, H.A., *MI Sylramic Tensile Testing*. 2001, Retrieved from AFRL.
52. International, A., *ASTM E562-11, Standard Test Method for Determining Volume Fraction by Systematic Manual Point Count*. 2011, www.astm.org: West Conschocken, PA.
53. Routbort, J., & Matzke, H., *On the correlation between solid-particle erosion and fraction parameters in SiC.* Journal of Materials Science, 1982. **18**.

54. Whitlow, T., Jones, E., & Przybyla, C., *Failure prediction in ceramc composites using acoustic emission and digital image correlation.* AIP Conference Proceedings, 2016. **1706**(1).
55. Grasselli, J.G.B., B.J., *Analytical Raman Spectroscopy*. 1991, New York: Wiley.
56. Hopcroft, M.A., W.D. Nix, and T.W. Kenny, *What is the Young's Modulus of Silicon?* Journal of Microelectromechanical Systems, 2010. **19**(2): p. 229-238.
57. Koun, S., *Temperature Dependence of Young's Modulus of Silicon.* Japanese Journal of Applied Physics, 2013. **52**(8R): p. 088002.
58. Cho, C.-H., *Characterization of Young's modulus of silicon versus temperature using a "beam deflection" method with a four-point bending fixture.* Current Applied Physics, 2009. **9**(2): p. 538-545.
59. Ouyang, G., et al., *Determination of the Si-Si bond energy from the temperature dependence of elastic modulus and surface tension.* EPL (Europhysics Letters), 2008. **84**(6): p. 66005.
60. Hess, P., *Laser diagnostics of mechanical and elastic properties of silicon and carbon films.* Applied Surface Science, 1996. **106**: p. 429-437.
61. Slack, G.A. and S.F. Bartram, *Thermal expansion of some diamondlike crystals.* Journal of Applied Physics, 1975. **46**(1): p. 89-98.
62. Gulden, T.D., *Mechanical Properties of Polycrystalline β-Sic.* Journal of the American Ceramic Society, 1969. **52**(11): p. 585-590.
63. Mital, S.K., Bednarcyk, B. A., Arnold, S. M., Lang, J., *Modeling of Melt-Infiltrated SiC/SiC Composite Properties*. 2009, NASA: Hanover, MD.
64. DiCarlo, J.A. and H.M. Yun, *SiC/SiC composites for 1200 C and above,* in *Handbook of ceramic composites*. 2005, Springer: USA. p. 33-52.
65. Mei, H., *Measurement and calculation of thermal residual stress in fiber reinforced ceramic matrix composites.* Composites Science and Technology, 2008. **68**(15–16): p. 3285-3292.
66. Murthy, P.L.N., S.K. Mital, and J.A. DiCarlo, *Characterizing the Properties of a Woven SiC/SiC Composite Using W-CEMCAN Computer Code*. 1999, NASA. p. 20.
67. Mital, S.K., et al., *Modeling of Melt-Infi ltrated SiC/SiC Composite Properties*. 2009, NASA. p. 20.
68. Billig, E., *Some Defects in Crystals Grown from the Melt. I. Defects Caused by Thermal Stresses.* Proceedings of the Royal Society of London. Series A. Mathematical and Physical Sciences, 1956. **235**(1200): p. 37-55.
69. *Silicon carbide (SiC) bulk modulus, Youngs modulus, shear modulus,* in *Group IV Elements, IV-IV and III-V Compounds. Part a - Lattice Properties*, O. Madelung, U. Rössler, and M. Schulz, Editors. 2001, Springer Berlin Heidelberg: Berlin, Heidelberg. p. 1-7.
70. Moss, D.R., *Pressure Vessel Design Manual*. 2004: Elsevier Science.
71. Gustafson, P.A., et al., *Measurement of Biaxial Stress States in Silicon Using Micro-Raman Spectroscopy.* Journal of Applied Mechanics, 2006. **73**(5): p. 745-751.
72. Mcnally, P.J., et al., *Monitoring of stress reduction in shallow trench isolation CMOS structures via synchrotron X-ray topography, electrical data and raman*

spectroscopy. Journal of Materials Science: Materials in Electronics, 1999. **10**(5): p. 351-358.

73. Chen, K.-S., *Techniques in Residual Stress Measurement for MEMS and Their Applications*, in *MEMS/NEMS: Handbook Techniques and Applications*, C.T. Leondes, Editor. 2006, Springer US: Boston, MA. p. 1252-1328.
74. Ingrid De, W., *Micro-Raman spectroscopy to study local mechanical stress in silicon integrated circuits.* Semiconductor Science and Technology, 1996. **11**(2): p. 139.
75. Amer, M., et al., *Environmental degradation studies of the interface in single-filament graphite/epoxy composites using laser Raman spectroscopy.* Advanced Composites Letters, 1994. **3**(1): p. 17-20.
76. Amer, M.S. and L.S. Schadler, *Micromechanical behavior of graphite/epoxy composites - Part I: The effect of fiber sizing.* Science and Engineering of Composite Materials, 1998. **7**(1-2): p. 81-113.
77. Amer, M.S. and L.S. Schadler, *Micromechanical behavior of graphite/epoxy composites - Part II: Interfacial durability.* Science and Engineering of Composite Materials, 1998. **7**(1-2): p. 115-149.
78. Wagner, H.D., M.S. Amer, and L.S. Schadler, *Residual Compression Stress Profile in High-Modulus Carbon Fiber Embedded in Isotactic Polypropylene by Micro-Raman Spectroscopy.* Applied Composite Materials, 2000. **7**(4): p. 209-217.
79. Amer, M.S., *Raman spectroscopy investigations of functionally graded materials and inter-granular mechanics.* International Journal of Solids and Structures, 2005. **42**(2): p. 751-757.
80. Schadler, L.S., M. Koczak, and M.S. Amer, *Environmental Effects on Interfacial Behavior in Graphite/Epoxy Single-Fiber and Multi-Fibers Composites*, in *Polymer/Inorganic Interfaces II*, L. Drazal, et al., Editors. 1995, MRS. p. 155-166.
81. Amer, M.S., *Raman spectroscopy and molecular simulation investigations of adsorption on the surface of single-walled carbon nanotubes and nanospheres.* Journal of Raman Spectroscopy, 2007. **38**(6): p. 721-727.